POLITECNICO DI TORINO

Master's Degree in Mechatronic Engineering

Politecnico
di Torino

Master's Degree Thesis

Comparison of radar sensors for indoor human localization

Supervisors

Prof. Mihai T. LAZARESCU

Prof. Luciano LAVAGNO

Candidate

Carmelo PIROSA

Academic year 2021-2022

Summary

In the last decades, the growth of the GPS usage in many fields for outdoor localization has led to a higher demand of systems for indoor human localization for many fields of application, like home security or safety and healthcare.

Indoor human localization and tracking is difficult due to the typically small indoor environments, with highly variable conditions like room dimension, ceiling height, or furniture type and location. Recent improvements in computer vision given by machine learning algorithms can provide a good solution based on optical cameras, but they still have many problems, such as privacy, cost, clear line-of-sight need. For this reason, there exist numerous alternative techniques that use different typologies of sensors to fulfill the human tracking objective, each one with specific limitations and capabilities.

An indoor human localization system suitable for retrofitting existing environments, that does not rely on tags attached to objects or on wearables is a challenging research objective. The aim of this work is to investigate the state of the art in the sensor-based Indoor Human localization techniques, and to implement a localization system using one of the available methodologies.

In this thesis, I explore the localization via microphone and ultrasonic sensors and via radar sensors. First, I have conducted a market analysis to compare existing indoor human localization and tracking techniques, and the capabilities of the utilized sensors. The analysed techniques can be basically divided into two categories: those that rely on tag or wearable sensors, and those that do not require any tags or wearables. The latter is clearly more acceptable from the end-user point of view, in terms of user-comfort and ease of installation, thus I focused the research on them, and in particular on radar sensors for human indoor localization and tracking. The market analysis showed that the best typology of sensor for the indoor human localization seems to be the radar sensor, due to the sensing capabilities, e.g., besides sensing the position of the target(s), depict also the velocity, acceleration, and the angle of arrival, the moderate price and the multiple-choice of commercial solutions. For this reason, the choice made has been to explore and study radar evaluation kits only.

I tested in various conditions commercial radar sensors, comparing the performance of different radar industrial development kits in identical and relevant environments: the Infineon Position2Go, a 24 GHz radar board equipped with an ARM® Cortex™-M4 XMC4700 microcontroller, and the Texas Instruments IWR6843ISK, a 60 GHz radar board, equipped with an ARM® Cortex™-R4F microcontroller.

The experimental part of the thesis starts by gathering several measurements from the two sensors in different environments, evaluating the precision of the measurements, as well as which radar is best for a given environment.

The chosen experimental areas are of three types:

1. A relatively small room, with 'environmental clutter' like chairs, tables, and cabinets, referred as *Laboratory*.

2. An empty indoor space with ample space of movement, referred as *Corridor*.

3. An open space environment referred as *Terrace*.

In every experiment, the target has walked the same trajectory in front of the sensors, made of horizontal and vertical straight lines 1.20 m long. The trajectory is at the minimum distance from the sensors that guarantees that it is centred to and fully within the Field-of-View of both sensors. The two boards have been positioned with the same orientation and as close as possible to each other in order to ensure a fair comparison of the results provided by the devices.

The walked path is composed of straight segments in order to determine the sensors capability to track straight controlled movements. The horizontal segments of the trajectory provide a good measure of the precision Angle-of-Arrival estimation of the sensors, while the vertical segments provide an evaluation of the precision of the range estimation of the two devices.

Before evaluating the sensor performance, all trajectory curves were removed because they are highly irregular in the normal movement of a person (different velocity, acceleration, and posture).

In order to evaluate the quality and errors of the measurement results, the following criteria have been established:

- *Linear regression error*: since the trajectory is made of straight lines, for every measured segment a linear regression is performed to determine the straight segments that fit best the measured segments. The criterion measures the error of such estimation.

- *Root area error*: since the chosen trajectory is repeatedly walked back and forth by the human target, the result of every experiment is a number of measured trajectories. The criterion is computed by calculating the average

of the area in-between every combination of two estimated straight lines associated with the same part of real trajectory. This criterion evaluates the self-consistency of the sensor measurements, i.e., how close to each other are all the trajectories detected by the sensors in constant conditions (environment and configuration).

- *Movement smoothness (acceleration)*: this criterion represents the sensors capability to detect the dynamic characteristics of the human body. This metric computes the change of the measured positions differentiated twice with respect to time. The criterion evaluates if the sensor measurements reflect the realistic movements of a human body, which usually keeps a steady movement on straight paths, with low and smoothly-varying accelerations.
- *Relative location error*: this criterion evaluates how well the measured trajectory can map on the size and shape of the actual trajectory. The measured trajectory is translated to minimize the errors between the ground truth and the sensed trajectory.

The two radars have been tested using four different configurations per radar. Such configurations have been created in order to understand if the specific configurable parameters had an impact on the localization performance of the sensors, and if such impact were the same in every tested environment. The configurations, hence, have been obtained using the tools provided by the producers, that gave us the possibility to modify all the configurable parameters.

For the thesis work, the original producers demo firmwares have been used for both sensors. Differently from the Texas Instruments IWR6843ISK sensor, where the output measurements have been directly used without applying any post-processing algorithm, in the Infineon Position2Go there had been the need to apply such refinements. First, I applied a moving-average filter to the measurements, in order to obtain a smooth trajectory path and not the original one where the walked real straight line were approximated to "zig-zag" movements. After this filter, the outliers positions have been removed, operation not performed for the Texas Instruments IWR6843ISK.

The *Minimized relative location error* of the path-translated measurements is very low in the Texas Instruments IWR6843ISK sensor, compared with the one obtained by the Infineon Position2Go sensor. The self-consistency of the Texas Instruments IWR6843ISK sensor is slightly worse than the Infineon Position2Go sensor in some configurations, but more or less the same as reported in the *Root area error*. The two sensors obtain almost the same *Linear regression error*, while the Infineon Position2Go sensor has a better measured *Movement smoothness*, since the computed acceleration is very low compared to the Texas Instruments IWR6843ISK sensor due to the moving-average filter applied to the measurements of the Infineon sensor.

Table 1: Position2Go sensor best measurements per environment, where Configuration 1, Configuration 2, Configuration 3, Configuration 4

Location	**Linear regression error** (m)	**Root area error** (m)	**Acceleration** (m/s^2)	**Relative location error** (m)
Laboratory	0.053	0.395	0.741	0.731
Corridor	0.083	0.408	0.667	0.816
Garden	0.077	0.358	0.721	0.712

Table 2: IWR6843ISK sensor best measurements per environment, where Configuration 1, Configuration 2, Configuration 3, Configuration 4

Location	**Linear regression error** (m)	**Root area error** (m)	**Acceleration** (m/s^2)	**Relative location error** (m)
Laboratory	0.095	0.305	1.685	0.134
Corridor	0.112	0.314	2.027	0.274
Terrace	0.082	0.310	2.089	0.711

The Infineon Position2Go sensor has two preferred configurations: Configuration 2 for Laboratory and Corridor, and Configuration 1 for Garden. Additionally, Configuration 2 is the second preferred configuration in the Garden environment, while Configuration 1 is the second preferred configuration in both indoor environments. Configuration 3 and Configuration 4 can be considered the worst configurations, since the latter is always ranked third or second, as shown in Table 1.

The Texas Instruments IWR6843ISK sensor has several preferred configurations: Configuration 3 for Laboratory, Configuration 4 for Corridor, Configuration 1 for Terrace. Additionally, Configuration 2 is the second preferred configuration in Corridor and Terrace environments, while is the third preferred configuration in Laboratory environment. This results can be seen in the Table 2.

Table 3, and Table 4 show an overview of the preferred configuration selection criteria for the two sensors.

The preferred indoor configuration for the Infineon Position2Go sensor, would work well even in outdoor environments, obtaining similar results than the preferred outdoor configuration. Note that, it is likely that the *Linear regression error* would get worse utilizing the configuration for outdoor localization.

Table 3: Infineon Position2Go preferred configurations per environment using majority voting (has the lowest error for at least half of the evaluation criteria). In the *Preferred* column, the configurations in decreasing order of votes

Location	**Best Configurations**				**Preferred**
	Linear regression	**Root area**	**Acceleration**	**Relative location**	
Laboratory	4	2	2	1	2,1,4,3
Corridor	4	2	2	1	2,1,4,3
Garden	1	1	3	2	1,2,3,4

Table 4: Texas Instruments IWR6843ISK preferred configurations per environment using majority voting (has the lowest error for at least half of the evaluation criteria). In the *Preferred* column, the configurations in decreasing order of votes

Location	**Best Configurations**				**Preferred**
	Linear regression	**Root area**	**Acceleration**	**Relative location**	
Laboratory	3	3	1	2	3,1,2,4
Corridor	4	4	3	2	4,2,3,1
Terrace	4	2	1	1	1,2,4,3

Unlike the Infineon Position2Go sensor, the Texas Instruments IWR6843ISK sensor has two preferred indoor configurations, one for the *Laboratory* and one for the *Corridor* environments. Looking at Table 4, we can say that the *Corridor* preferred configuration is suitable also for outdoor environments, despite it is likely to achieve higher evaluation criteria values, except for the *Linear regression error*. Following the same assumption, the *Laboratory* preferred configuration would not be suited for outdoor environments, despite it is likely to achieve a lower *Linear regression error*.

Additionally, it is important to notice that the obtained configurations are not optimized for the sensors in each environment, hence, by performing a fine tuning of the configurations, it should be possible to obtain even better results than the one obtained in this thesis.

Each chosen criteria, except for the *Minimized relative location error* and the *Acceleration*, vary in general in the same ranges for both sensors. That said, if we consider also the higher need for post-processing algorithms, like the need to implement a moving-average algorithm on the measured trajectory positions of the Infineon Position2Go, it is possible to determine that the Texas Instruments

IWR6843ISK sensor is the best choice for Indoor human localization.

Table of Contents

List of Tables

List of Figures

Acronyms

Chapter 1

Introduction

The objective of this work is to introduce all the existing techniques of Indoor human localization that utilize sensors as detecting devices, in order to compare their capabilities and limitations.

The objective of the indoor human localization techniques is to create a live map of any indoor environment, regardless of the composition of such space, like the amount of furniture or dimensions of the room, allowing this field to find many different applications, like security, safety and healthcare, live assistance, retail and hospitality, internet of things (IoT) smart homes.

The localization techniques can be broadly split into two categories: tags or wearable localization techniques and tag-less or wearable-less localization techniques, having the latter as the focus of this thesis work. Currently, sensors like optical cameras, radars or sound-waves sensors can be used for the tag-less or wearable-less techniques while sensors that use Bluetooth, Wi-Fi, or radio frequency identification (RFID) tagging can be used for the tags or wearable counterparts.

Creating an indoor human localization system without the need to change the current environment, performing actions like attaching tags to the furniture, or without the need to have the user wear anything is a very interesting possibility that is worth exploring as much as possible, for this reason, this thesis work focuses on the localization via radar sensors.

The chapters of the work are organized as follows: Chapter 2 focuses on the indoor human localization techniques of both aforementioned categories, providing a description of the working principle of most of the sensor-based systems existing in the market and as prototypes. Then, a market analysis of a sub-set of sensors utilized in tag-less and wearable-less techniques is presented, focusing on the comparison of several radar development kits.

The acoustic analysis technique is presented in Chapter 3, technique that allows the human localization utilizing sound wave-based sensors, with the distinction between active systems and passive systems.

In Chapter 4 a summary of the working principle of radar sensors is presented, with a focus on the mathematical parameters estimation of the frequency-modulated continuous wave (FMCW) radars.

In Chapter 5 the two radar development kits utilized in the experimental part of the work are described, the Infineon Position2Go sensor and the Texas Instruments IWR6843ISK sensor, with an overview of the hardware that composes the two, a description of the firmware utilized and of the graphical user interface (GUI) needed to configure, use and obtain the output data of such sensors.

In Chapter 6 a description of the measurements gathering method is presented, with the description of the target environments and all the configurations utilized for the two sensors. Finally, the description of the MATLAB post-processing algorithm utilized in order to compute the evaluation criteria for them measurements.

Finally, the experimental results are reported in Chapter 7, followed by conclusions and future investigations and developments of this thesis work.

Chapter 2

Indoor Human Localization

The indoor human localization is a necessity of growing importance in the past few decades which consists on the capability to detect and track all the humans present in a unique environment with particular characteristics.

While playing a predominant role in outdoor environments, the global positioning system (GPS) is pretty inefficient in indoor environments [1], due to phenomenons like:

1. Inability of GPS signal to penetrate through walls.
2. Multi-path propagation effect generated by the reflections of the signals on different surfaces [2].
3. Noise interference due to devices such as home appliances.
4. Line-of-sight need for GPS signals.

Due to all these inefficiencies, several indoor human localization systems have been proposed, which make use of different sensor types.

These sensors can be categorized by the physical quantity that they measure, like have been done in [3] where the scheme in Figure 2.1 has been proposed.

The principal concern about these sensing techniques is clearly the privacy of the detected humans along with the ease of installation of the required systems; the first is often addressed by utilizing sensors with specific characteristics (e.g., in optical sensing, by using cameras with low resolution), or by discarding a specific type of sensor in favor of another one (e.g., infrared cameras are often the preferred one in optical sensing).

For what regards the ease of installation there are different options, for instance, a localization system could be composed of just a single board connected to a computer with a cable or could comprise more complex systems that would require to set up a particular environment, which could represent a difficulty.

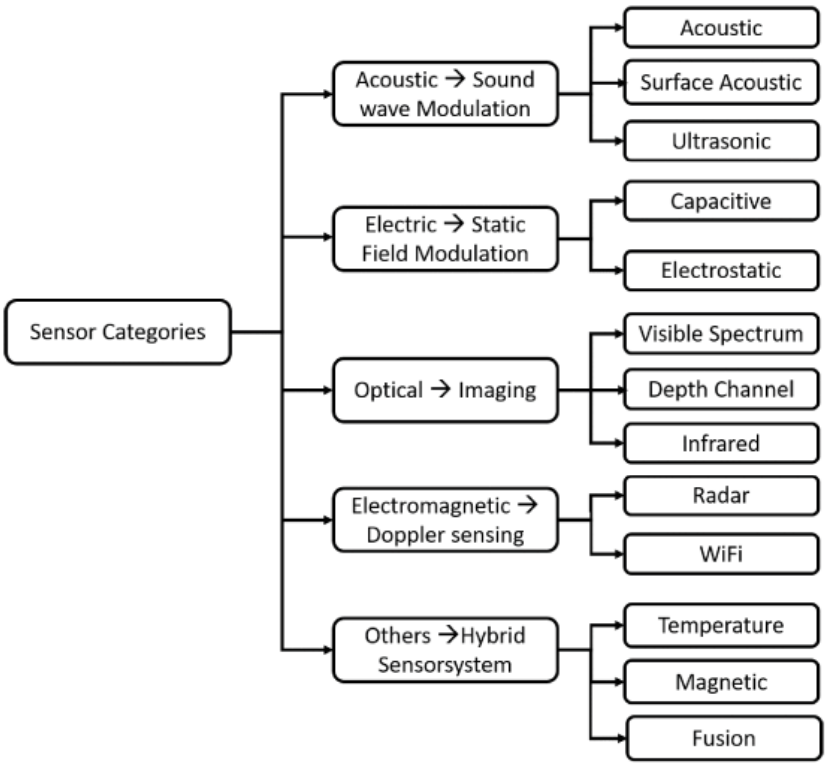

Figure 2.1: Sensor categorization scheme based what these devices sense [3]

2.1 Main Localization Techniques

In the following, an overview of the available techniques for localization, which can be categorized by the interaction that these systems must have with the humans in order to detect them.

2.1.1 Using Tags, Wearables, or Special Interaction

The systems in this category are not able to directly detect a human being, but they detect the presence of a particular object, which can be then associated to a person.

There are multiple systems that can fall under this category, like:

1. **RFID**, a sensor that utilizes electromagnetic fields to identify particular tags.

   An RFID system [4], shown in Figure 2.2 is composed by:

   (a) **Single or multiple RFID tags**, composed of the microchip, responsible for the signal processing and the storage of the information that a

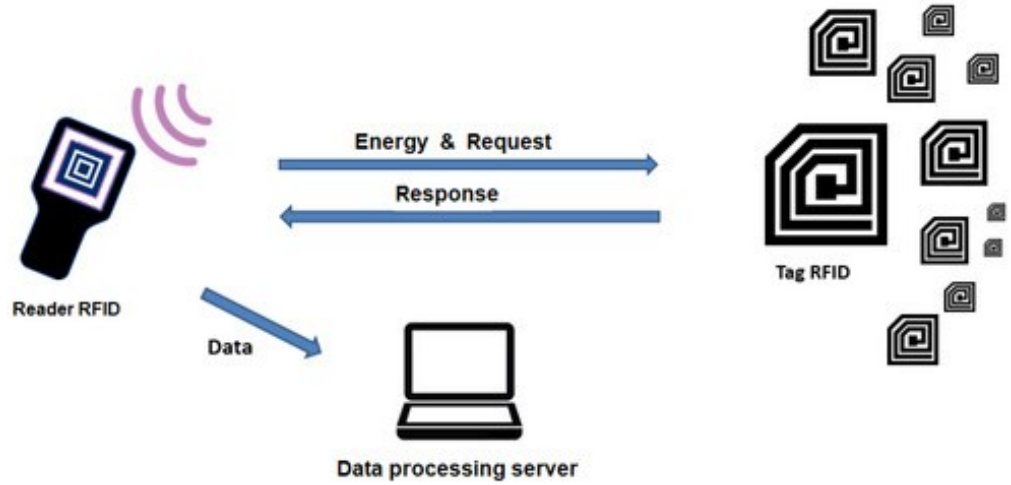

Figure 2.2: Basic radio frequency identification (RFID) system composed of reader, tag(s) and computer database in order to store data [5]

particular tag must transmit to the reader and an antenna for receiving and transmitting the signal to the reader. The tags can be active, e.g., battery-powered, or passive, where the antenna is powered up by the signal received by the reader.

The passive tags are smaller and cheaper because they do not need a battery to operate, but in order to work, they require a very high power from the reader.

(b) **Reader**, responsible for the reception of the reflected signal of the tag. There can be active readers, which actively transmit the interrogation signal to the tags and also receive their replies, or passive readers, which only receives the signals from the active tags.

The RFID system can be also composed of an active tag and an active reader, where the reader transmits interrogation signals to the active tag. In these systems, the distance that separates the reader from the tag can be very high.

(c) **Storage system**, needed in order to manage all the data.

The primary advantage of this type of system is for sure the low cost of the tags (especially the passive ones), in contrast with the cost of the infrastructure (readers and all cables needed) which can be quite high depending on the number of readers employed.

The human localization technique utilized in these systems requires the humans to wear the reader, which will detect the tags attached to fixed locations when

the humans walk near them, as has been proposed in [6].

Moreover, these systems are often employed in the human activity recognition (HAR) field, where tags attached to multiple objects are utilized in order to understand which object is being used by the person monitored like has been proposed in [7] where the system has been used for elder care.

2. **Bluetooth systems**, which utilize the ultra-high frequency (UHF) radio waves to create a personal area network (PAN) between devices, in order to allow data exchange between them [8].

   Bluetooth networks utilize packet-based protocol with a master/slave architecture, characterized by a dynamic time-division multiple access algorithm which divides the time in slots used for the transmissions of the two types of devices (master or slaves) having all the nodes synchronized with the internal clock of the master.

   The big advantage of this localization system is that the Bluetooth radio modules are very cheap and consume very little energy, allowing the devices to work for a very long time before having the need to be recharged or having their batteries changed.

   In the work of Kolakowski and Blachucki [9], a system comprising Bluetooth tags attached to the users, a set of anchors distributed in the localization area and a system controller has been employed to localize and track persons affected by dementia.

   In this system, whose architecture is shown in Figure 2.3, the tags are always transmitting packets at a constant rate of ten times per second, which are then received by the anchors that are in radio visibility of the tag. Finally, the system controller will process all the received packets of the anchors and calculate the position of the users by combining all the received measurements.

2.1.2 Without Tags, Wearables, or Explicit Interaction

The sensor systems present in this category are able to detect a human directly, without using particular infrastructure or the requirement for the human to be equipped with a wearable.

In the following, a list of the principal sensing techniques able to directly sense the human being in an area:

1. **Optical camera**: a very simple human localization technique, which consists of standard optical cameras mounted in the area to monitor, which use computer vision techniques in order to detect a human being or distinguish between moving humans and moving objects.

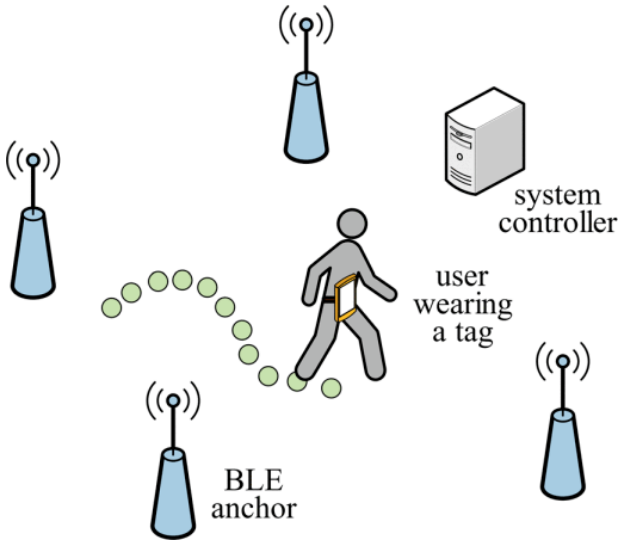

Figure 2.3: Kolakowski and Blachucki Bluetooth localization system, composed of wearable tag (worn by the targets) and bluetooth low energy (BLE) anchors to detect the tag [9]

The difficulty of this type of system, besides the need for a clear line of sight, is the development and the optimization of the algorithm utilized for the computer vision itself, which usually consists of a convolutional neural network (CNN) [10] or recurrent neural network (RNN) [11].

A **CNN**, shown in Figure 2.4 is a particular type of neural network, most commonly used in classification, which implements the so-called convolution layers, which are layers (hidden layers) that perform a convolution of the input data that then is passed to the next layers. The result of this operation is an output abstracted to an activation map, which is then fed to the next layers.

Together with the convolutional layers, in a CNN may also be present the pooling layers, which have the objective to reduce the dimensions of the activation maps with a particular pooling operation, which can be considered equal to the application of a filter, Figure 2.5.

Like the convolutional ones, the pooling layers are hidden layers in a CNN.

It is important to notice that in a CNN every single neuron does not receive its input from the entire previous layer, like it happens in fully connected neural networks, but it receives input from only a restricted area of the previous layer, called the receptive field of the neuron. The final output of a CNN is an abstract output that allows the network to better understand the class to which the input belongs.

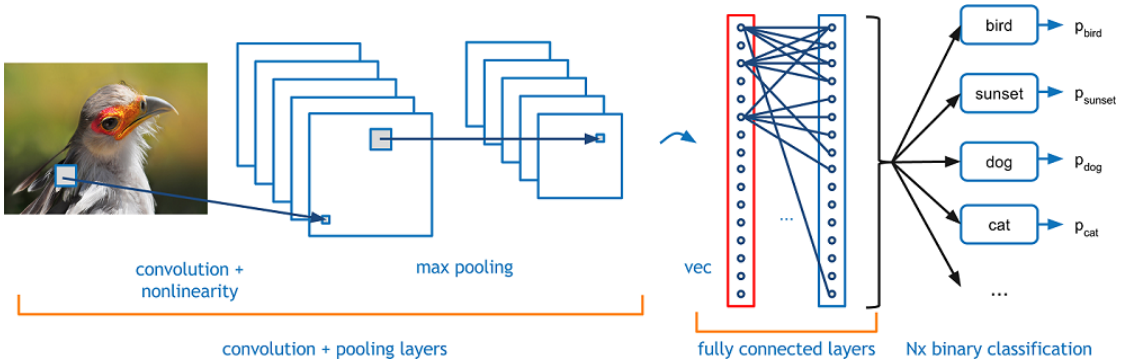

Figure 2.4: Convolutional neural network (CNN) network utilized for image classification, formed by convolutional and pooling layers, connected to fully connected layers to produce a non-binary classification [12]

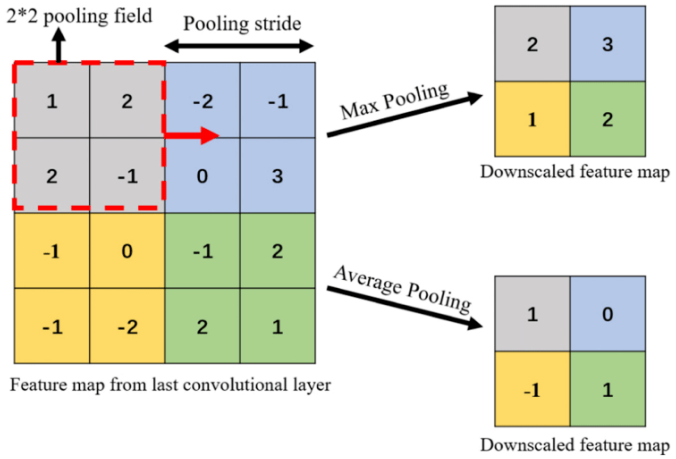

Figure 2.5: Max-pooling operation performed by pooling layers in CNN [13]

An **RNN** is another class of neural networks characterized by a temporal dynamic behavior.

Differently from the feedforward neural networks [14] shown in Figure 2.6, in which the connections between different nodes can not form a cycle, hence the information can only move forward, in the RNNs, Figure 2.7, cycles between nodes can be present, allowing the neurons to re-process their own output many times over time.

The main concern about the human localization technique that uses optical camera along with computer vision algorithms is the privacy: the face of the detected human beings will be clearly visible from the camera or the cameras installed in the environment.

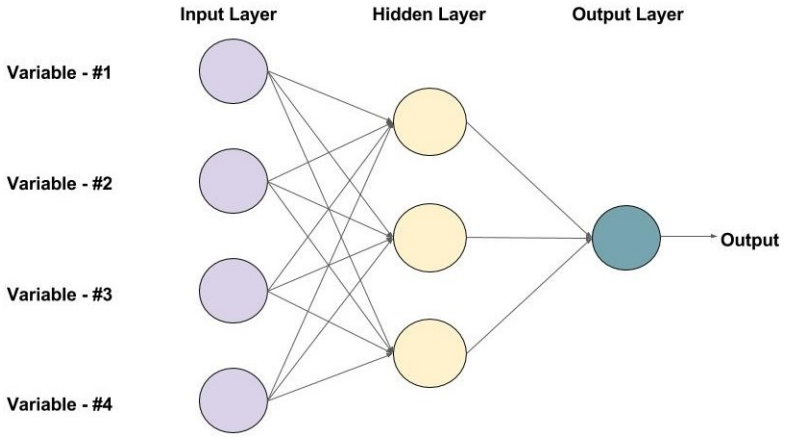

Figure 2.6: Example of a feedforward neural network with one hidden layer [15]

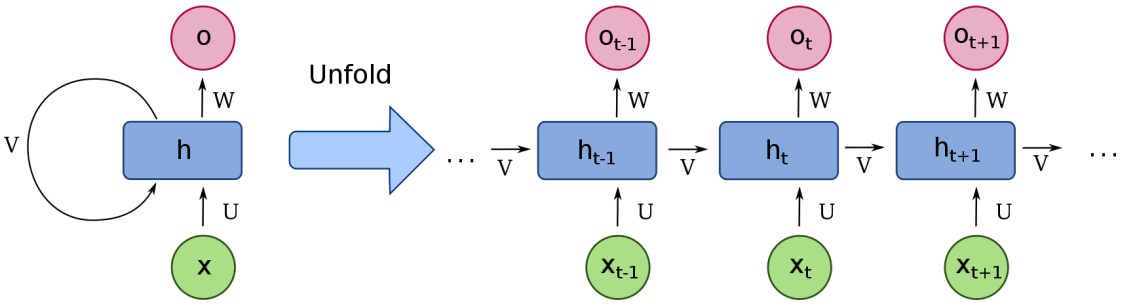

Figure 2.7: Example of a recurrent neural network (RNN) with one unit, x are the inputs, h are the hidden states, o are the outputs. On the left, the complex diagram of the network (folded), on the right the extended version (unfolded) [16]

The cost of such a system can be very variable, it all depends on the number of cameras utilized and of course, their overall technical quality represented in terms of number of megapixels, lens quality, overall resolution, etc.

2. **Infrared (IR) camera**: also known as thermal imager [17], this camera sensor, often micro-electromechanical system (MEMS) devices, shown in Figure 2.8, is able to create an image by detecting the IR radiation of the environment, similar to the classic optical cameras that create images by detecting the visible light.

   IR cameras, in fact, are sensible to wavelengths in the range of 1,000 nm to 14,000 nm, in contrast to the range detected by a normal camera which is from 400 nm to 700 nm.

   Once the IR camera has captured the thermal image or video, such element can be analyzed using computer vision methods like the previous sensing

(a) Micro-electromechanical system (MEMS) thermal camera [18]

(b) Industrial thermal camera [19]

Figure 2.8: Some infrared (IR) cameras

Figure 2.9: Capture of a low resolution thermal imager [20]

technique, with the difference that now the users privacy is respected, since by using a low-resolution thermal camera, the human faces will not be clearly visible, like it can be seen in Figure 2.9.

3. **Microphone systems**: exposed in Chapter 3.

4. **Ultrasonic sensors**: exposed in Chapter 3.

5. **Capacitive proximity sensing**: this type of technique is based on the concept that an electric field is perturbed by the existence of a conductive object, which in this case is a part of the human body. More specifically, we apply voltage to only one electrode of the sensor, allowing the latter to

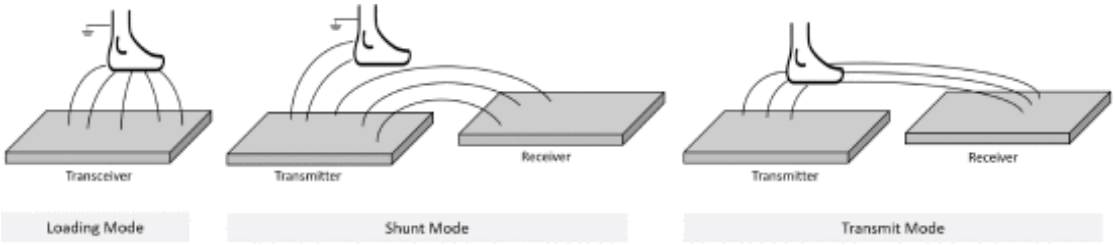

Figure 2.10: The three operating modes of a capacitive sensor, the *Loading mode* utilized to compute the distance between object and electric field, the *Shunt mode* where the electric field is weakened by the presence of a body, and the *Transmit mode* where the object body acts as a transmitter [21]

generate the electric field.

The capacitive sensing principle can be divided into three operating modes [21]: *loading mode, shunt mode, and transmit mode*, as shown in Figure 2.10.

(a) *Loading mode*: Mostly utilized in order to compute the relative distance between the object and electric field,

(b) *Shunt mode*: in this mode, the strength of the electric field is weakened by the presence of the object.

(c) *Transmit mode*: The path of the electric field lines is shortened by the object that acts as a transmitter. This result in an amplification of the electric field.

In the transmit mode the object is a point source, the electric field will be dependent by the latter through the formula $1/r^2$ where r is the distance between receiver and object while the object is near the field, while the formula will become 1/r when the distance will increase.

The localization technique which applies capacitive proximity sensing is based on "smart floors" which embed the capacitive sensors directly in the tiles, that can be made of any non-conductive material. The tiles will be capable of detecting and tracking a person, as well as recognizing a person or a moving object, using the electric field principle aforementioned. These works have been carried out by Steinhage [22] and Valtonen [23].

6. **Resistive pressure sensing**: technique that employs mechanical sensors in order to work [24]. Mechanical sensors are transducers that convert the pressure applied to them P = F/A, with *P = pressure, F = force normal to contact surface, A = area of contact*, in an electric signal. In particular, the force applied to the sensing surface will deform the latter, the sensor will

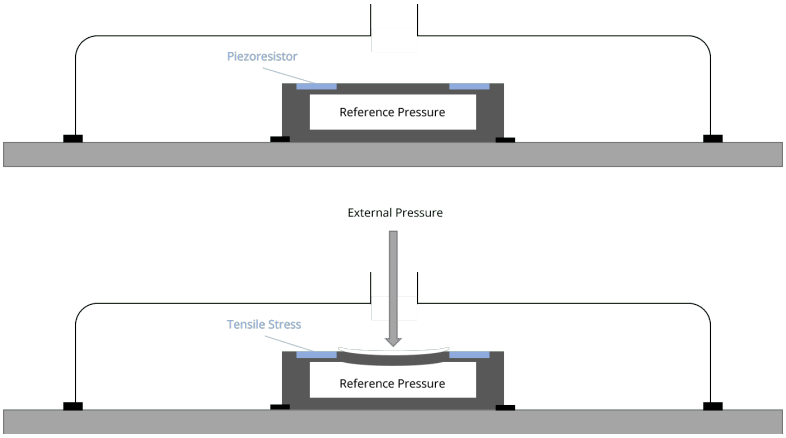

Figure 2.11: A piezoresistive pressure sensor on top, the same piezoresistive pressure sensor with an external force applied that causes the deformation of the device due to tensile stress on bottom [25]

produce an electrical signal proportional to the amount of force, which will be then sampled by an analog to digital converter (ADC).

The localization technique is very similar to the one that employs capacitive proximity sensors, hence it utilizes "smart floors" where the pressure sensors are embedded, enabling the environment for a room-scale localization and detection as well as depicting the poses of the humans in the room with proper signal processing, like has been done in the *GravitySpace* project [26].

7. **Wi-Fi sensing**: based on the radiations, in the form of high-frequency electromagnetic waves [27] [28] [29]. According to the 802.11 standard domestic Wi-Fi operates in the frequency bands of 2.4 GHz when high-range transmission is needed and 5 GHz for close-range transmissions [30]. Working with the 2.4 GHz band allows a good solid object penetration, allowing for better coverage.

   The sensing technique, shown in Figure 2.12 utilized in Wi-Fi systems is actually very similar to the one employed by radars; it consists, in comparing the radiation waves generated by the sensor with the ones reflected back by objects inside the electromagnetic field of the device. This comparison is made by analyzing the channel state information (CSI) which describes the Wi-Fi channel properties. The movement of a human in the Wi-Fi signal covered area, will cause different phenomena in the signal, like attenuation, frequency shift and change in propagation path. Exploiting this phenomena, it is possible to understand the presence of a human in the area [28].

8. **Radar sensors**: discussed in Chapter 5.

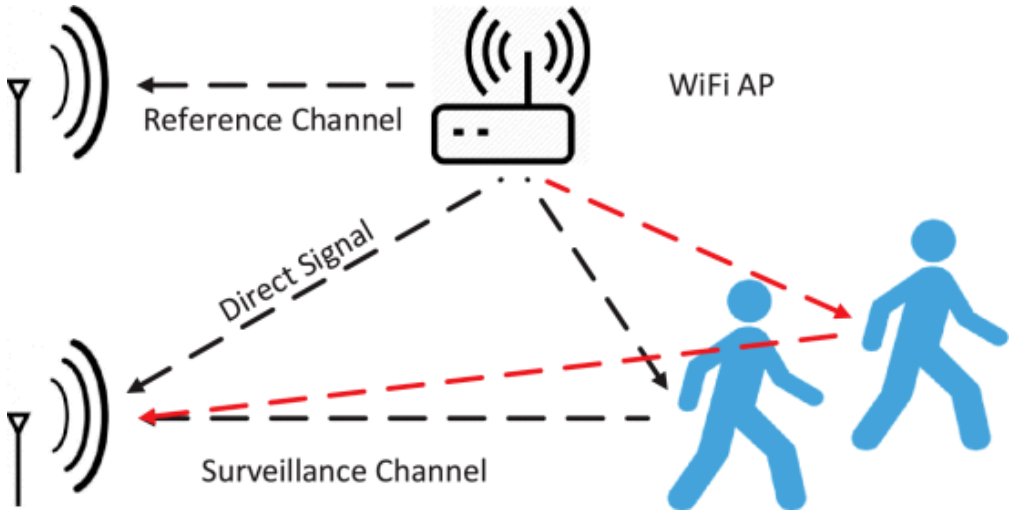

Figure 2.12: Wi-Fi sensing technique employed in [28], where the Wi-Fi access point (AP) is able to detect a human body by analyzing the channel state information (CSI), which describes the Wi-Fi channel properties. When the signal is scattered by a human body, the channel state information (CSI) changes accordingly

2.2 Market Analysis

In order to understand which sensor typology could be the best for the human localization, a market analysis has been conducted, in order to compare the principal available sensors. More specifically the sensors that have been compared are:

1. Microphone sensors
2. Ultrasonic sensors
3. Capacitive proximity sensors
4. Radar sensors

In the first part of the analysis, only the sensor modules to be connected to micro-controller boards have been analyzed.

In Table 2.1, several microphone sensors are compared, considering their working frequency range, sensing sensitivity, energy consumption, and the dimensions of the devices. Regarding the directionality, only omnidirectional microphones have been chosen since, for the localization task, the human can be positioned in any part of the room taken in consideration. Most of the sensors considered are MEMS devices, which have the advantage of having small dimensions. Differently from the sensors considered in the other tables, in Microphone sensors there is no information about the distance at which the sensor is capable to detect. Such types of sensors must hence work in a room with little or no noise, in order to have the best measurements possible.

Shown in Table 2.2, the comparison between different ultrasonic sensor elements. The reported features of such devices are the electromagnetic wave frequency, the sensitivity, the maximum range at which the sensor is able to detect the targets, the area of sight of the sensor, expressed in °, the power consumption, and finally dimensions and sensor typology. All the compared sensors are *Sensor module*s meaning that the devices are sensor kits that usually utilize inter integrated circuit (I2C) communication protocol in order to send data to the microcontroller unit (MCU). Considering the task, the most suited ultrasonic sensor should be the A02YYUW, which present the highest area of sight, and a reasonable maximum detection distance of about 4.5 m.

In Table 2.3, the comparison between capacitive proximity sensors. The reported characteristics are the detection range, in mm, the *Set distance*, which is the minimum distance at which the sensor is able to detect, the *Standard detection object*, the supply needed, the dimensions and finally the typology and some notes if present. Even if in most of the sensors the detection object indicated is Iron, such sensors are also able to detect the presence of a non-metal object or body.

Shown in Table 2.4 the list of all the compared radar sensors. The characteristics reported are their working frequency, the typical detection range for human targets, the set distance, e.g., the minimum distance at which the sensors are able to detect a target, the power consumption and finally the dimensions and the typology. Most of the sensor present in this table are monolithic microwave IC (MMIC) where IC stands for IC, which is the chip that operates directly with the frequency, hence representing the heart of a radar sensor. Most of the sensors shown in the table, with the exception of RR30.DAO0-IGPI.9VF and the IWR6843ISK, have similar characteristics, this is because they work with almost the same frequency band, which starts at 24 GHz.

After comparing all the sensor types and their applications, the sensors chosen to be tested for the thesis are the radar sensors, due to their better accuracy, more developed examples and experiments, ability to detect the target(s) without the need of tags, special wearables or special interactions needed, and finally ease of installation in different environments (they just need to be placed in a wall or in the ceiling using simple screws). In order to directly test the abilities of these sensor types, complete development boards have been chosen for the thesis purpose, which do not need external micro-controller, or need cheap micro-controllers like Raspberry, and perform all the signal processing parts directly on the board.

The comparison between the development kits present in the market can be seen in the Table 2.5, where the sensors have been compared considering their working frequency, the capability to detect motion, direction, position, distance, and velocity, the capability to detect single or multiple targets, the typical minimum and maximum range for human targets, and finally the MMIC utilized by the kits.

After comparing all the development kits, two of them have been selected, which are the Infineon Position2Go and the Texas Instruments IWR6843ISK, for their advanced human tracking algorithms and their high accuracy.

The two sensors have been selected in order to test the capabilities of the radars which operate at different frequency bands, having the Position2Go most suitable for, but not limited to, outdoor environments, and the IWR6843ISK most suitable for, but not limited to, indoor environments.

Table 2.1: Microphone sensors comparison

Name	Frequency range (Hz)	Sensitivity	Directionality	Energy consumption	Dimensions (mm)	Type
Grove sound sensor [31]	16,000–20,000	−60 dB V/Pa to 56 dB V/Pa	omni	4 V–5 V 4 mA–5 mA	2.4 x 20 x 9.8	Module
WPSE309 [32]	50–20,000	46 dB to 66 dB	omni	3.3 V–5 V	44 x 15 x 10	Module
Adafruit MEMS Microphone [33]	50–15,000	−29 dBFS to −23 dBFS	omni	1.62 V–3.6 V 600 µA	3.50 x 2.65 x 0.98	MEMS
IM69D130 [34]	20–20,000	−37 dBFS to −35 dBFS	omni	1.62 V–3.6 V 25 µA–980 µA	4 x 3 x 1.2	MEMS
MP23ABS1 [35]	35–15,000	−39 dB V to −37 dB V	omni	1.52 V–3.6 V 120 µA–150 µA	3.5 x 2.65 x 0.98	MEMS
LM393 [36]	100–10,000	52 dB to 48 dB	omni	3.3 V–5 V 4 mA–5 mA	34 x 16	Module
SPV1840LR5H-B [37]	100–10,000	−35 dB V/Pa to −41 dB V/Pa	omni	1.5 V–3.6 V 45 µA–60 µA	2.75 x 1.85 x 0.98	MEMS
SPM1423HM4H-B [38]	100–10,000	−19 dBFS to −25 dBFS	omni	1.6 V–3.6 V 600 µA	4.72 x 3.76 x 1.25	MEMS
SPH0611LR5H-1 [39]	100–10,000	−37 dB V/Pa to −39 dB V/Pa	omni	1.5 V–3.6 V 185 µA	3.50 x 2.65 x 1.10	MEMS
SPM0437HD4H-B [40]	100–10,000	−23 dBFS to −29 dBFS	omni	1.6 V–3.6 V 500 µA	4.72 x 3.76 x 1.35	MEMS
SPU1410LR5H-QB [41]	100–10,000	−35 dB V/Pa to −41 dB V/Pa	omni	1.5 V–3.6 V 160 µA	3.76 x 3.00 x 1.20	MEMS

Table 2.2: Ultrasonic sensors comparison

Name	**Acoustic emission frequency** (Hz)	**Sensitivity**	**Range** (m)	**Effective angle** (°)	**Consumption**	**Dimensions** (mm)	Typology
HC-SR04 [42]	40,000	−65 dB min	0.02–4	15	5 V 15 mA	40 x 20 x 15	Sensor module
HY-SRF05 [43]	40,000	Not specified	0.02–4.5	15	4.5 V–5.5 V 10 mA–40 mA	45 x 21	Sensor module
URM09 [44]	40,000 ± 2,000	Not specified	0.02–5	60	3.3 V–5.5 V 20 mA	47 x 22	Sensor module
A02YYUW [45]	40,000 ± 1,000	Not specified	0.03–4.5	100	3.3 V–5 V 8 mA	63.6 x 29.6 x 12.5	Sensor module
MB1013 [46]	42,000	Not specified	0.3–5	44	2.5 V–5.5 V 2.5 mA–3.1 mA	22 x 19 x 15	Sensor module
MB1360 [47]	42,000	Not specified	0.25–10	62	3.3 V–5.5 V 3.4 mA	22.1 x 19 x 25.11	Sensor module

Table 2.3: Capacitive proximity sensors comparison

Name	Detection range (mm)	Set distance (mm)	Standard detection object	Supply	Dimensions	Typology	Notes
LJC12A3-5-Z/AY [48]	5 ± 10%	0–4	Iron: 50 mm x 50 mm x 1 mm	DC: 6 V to 36 V AC: 90 V to 250 V 50/60 Hz	M12	Industrial	Non-shielded
LJC18A3-B-Z/BX [49]	10 ± 10%	0–8	Iron: 50 mm x 50 mm x 1 mm	DC: 6 V to 36 V AC: 90 V to 250 V 50/60 Hz	M18x1x60	Industrial	Non-shielded
CAT2-12GM series [50]	2 ± 10%	0–1.7	Iron: 50 mm x 50 mm x 1 mm	DC type: 200 mA max AC type: 400 mA	M12x1x50	Industrial	Shielded
CAM8-20GM series [51]	8 ± 10%	0–7	Iron: 50 mm x 50 mm x 1 mm	DC: 6 V to 36 V AC: 36 V to 250 V 50/60 Hz	ø20x78	Industrial	Non-shielded
CPM40-80B series [52]	40 ± 10%	0–36	Iron: 50 mm x 50 mm x 1 mm	DC: 6 V to 36 V AC: 36 V to 250 V 50/60 Hz	80 mm x 80 mm x 40 mm	Industrial	Non-shielded
EC 3025 TBA P L-6 [53]	16 mm flush mounted 25 mm non-flush mounted	0 mm–2 mm flush[1] mounted 0 mm–4 mm non-flush[2] mounted	Not specified	AC: 20 V–250 V	M12	Industrial	None
CA18EAxxBP-xIO - IO-Link [54]	8 mm flush mounted 12 mm non-flush mounted	0 mm flush mounted 0 mm non-flush mounted	Not specified	DC: 10 V–40 V	M18x1	Industrial	None
KIA3150NFPKG2T/US [55]	15 ± 10%	Not specified	Not specified	DC: 10 V–36 V	M30x1.5	Industrial	None

[1]Flush: The sensor do not require free space around the sensing face
[2]Non-flush: The sensor does require some free space around the sensing face

Table 2.4: Radar sensors comparison

Name	Frequency (GHz)	Detection range (m)	Set distance (m)	Consumption	Dimensions (mm)	Typology
BGT24MTR11 [56]	24–26	20	0.5	−0.3 V to 3.6 V 150 mA	5.5 x 4.3 x 0.9	MMIC chip
BGT24MTR12 [57]	24–24.25	20	0.5	−0.3 V to 3.6 V 210 mA	5.5 x 4.3 x 0.9	MMIC chip
BGT24LTR11N16 [58]	24–24.25	20	0.1	−0.3 V to 3.6 V 45 mA	2.4 x 2.4 x 0.73	MMIC chip
BGT24MR2 [59]	24–24.25	20	0.2	3.3 V 90 mA	5.5 x 4.3 x 0.9	MMIC chip
RR30.DAO0-IGPI.9VF [60]	122–123	6	0.2	12 V to 30 V 200 mA	ø28 x 97	Sensor module
FM24-NP100 [61]	24	20	0.5	4 V to 8 V 100 mA	34 x 44 x 5	Sensor module
MW2401TR11 [62]	24–24.25	20	0.5	5 V to 12 V 50 mA to 56 mA	20 x 20 x 2.54	Sensor module
IWR6843ISK [63]	60–64	10	0.2	3.3 V	10.4 × 10.4 x 0.65	MMIC chip

Table 2.5: Radar development kit comparison

Name	**Frequency** (GHz)	**Motion detection**	**Direction detection**	**Position** detection	**Distance** detection
DEMO Distance2GOL [64]	24–24.25	Yes	Yes	No	Yes
DEMO Sense2GOL pulse [65]	24–24.25	Yes	Yes	No	No
DEMO Position2GO [66]	24–24.25	Yes	Yes	Position tracking	Yes
Grove doppler radar [67]	24–24.25	Yes	Yes	No	No
DEMO BGT60LTR11AIP Kit [68][69]	60–61.5	Yes	Yes	No	No
Acconeer XC112-XR112 Kit[1] [70][71][72]	60–64 PCR[2]	Yes	Yes	Position tracking	Yes
OPS243-C-FC-RP [73]	24–24.25	Yes	Yes	No	Yes
MM5D91E00 [74]	61–61.5	Detects presence	No	No	No
IWR6843ISK [63]	60–64	Yes	Yes	Yes	Yes
IWR1843BOOST [75][76]	76–81	Yes	Yes	Yes	Yes

Name	**Velocity** detection	**Target**	**Min range** (m)	**Max range** (m)	**MMIC chip**
DEMO Distance2GOL [64]	Yes	Single	0.5	15–20	BGT24LTR11
DEMO Sense2GOL pulse [65]	Yes	Single	0.5	18 m	BGT24LTR11
DEMO Position2GO [66]	Yes	Multiple	0.6	20	BGT24MTR12
Grove doppler radar [67]	Yes	Single	0.5	10	BGT24LTR11
DEMO BGT60LTR11AIP Kit [68][69]	No	Single human	0.5	7	BGT60LTR11AIP
Acconeer XC112-XR112 Kit[1] [70][71][72]	Yes	Single human	0.2	2	AC111
OPS243-C-FC-RP [73]	Yes	Multiple	1	15	Not specified
MM5D91E00 [74]	No	Single	0	10	Not specified
IWR6843ISK [63][77]	Yes	Multiple	0.2	10	IWR6843
IWR1843BOOST [75][76]	Yes	Multiple	0.5	37	IWR1843

Chapter 3

Acoustic Analysis

Acoustic analysis is a technique that allows to detect the position of objects utilizing sound waves. The technique can be expanded in order to detect humans in an environment, as well as, by using particular machine learning (ML) algorithms, to detect the activity performed by humans.

Acoustic localization systems can be divided in active systems, which are able to localize the objects by first producing a sound wave and then by analyzing the received echo, a working principle similar to the one employed in radar systems, and passive systems which analyze the sound or the vibrations produced by the object to detect it, mimicking the localization ability of the human ears.

Both the active and passive systems, when used in water, are referred to as **sound navigation and ranging (SONAR)**, mostly used in submarine navigation [78].

Before the development of the radar systems, the SONAR technology was also used in order to implement acoustic location in air for atmospheric investigation purposes. These systems, known as **sonic detection and ranging (SODAR)**, are used as wind profilers, in order to measure the wind speed at various height operating using the Doppler effect.

3.1 State of the Art

The acoustic analysis techniques are mostly utilized when dealing with industrial and production machinery that are prone to produce a high density of acoustic noise and vibrations, which are perceived as disturbs. These sound emissions represent a great danger for the workers that operate such machines, since could lead to long-term hearing damages, if not hearing loss in the worst case scenarios. Hence, the need to reduce, or when possible suppress, such noises is of primary importance. The main challenge of noise suppression is the need to know the exact position

of the acoustic emissions, making the sound localization techniques of upmost importance.

In the last years, sound source localization, which mainly utilizes sensors like acoustic camera microphone arrays, achieved significant improvements, which, however, still suffer some challenges, like when dealing with moving sound source localization [79].

The sound source localization finds also application in the field of robotics. This functionality in fact, can be useful in many tasks, like the localization of a human speaker, rescue scenario with no visual contact, or the mapping task of an unknown acoustic environments [80].

3.2 Active Systems

The active sound source localization systems are composed of a device responsible for the sound signal generation and a device responsible for the reception of the reflected echo of this transmitted sound, in order to detect the objects in which the signal has reflected.

As previously stated, this working principle is the same employed in radar systems, with the difference that the signal analysis is different in this type of systems.

The principal active locators are:

1. **Active SONAR**: composed of a sound transmitter and a receiver, this sensor is operated in the so called monostatic operation if transmitter and receiver are present in the same place, and in bistatic operation if otherwise. Moreover, if more spatially distanced transmitters are present, the operation mode is called multistatic operation [81].

   The transmitted sound wave is usually electronically generated, but other methods can be used, like using chemical explosives, or plasma sound sources.

   The generated pulse of sound, the "ping" will be reflected back to the receiver if an object is present in its trajectory, and in order to measure the distance between the object and the SONAR, the time measured between transmission and reception will be utilized, with the knowledge, of course, of the speed of sound, Figure 3.1

2. **Time-of-arrival (TOA) localization**: localization method that utilizes systems composed of speakers for signal transmission and microphones for signal reception or ultrasonic sensors [83], shown in Figure 3.2 for the localization of objects [84].

   The difference between the two sensors is basically the frequency of the transmitted signal, having a frequency range between 20 Hz to 20 kHz for the

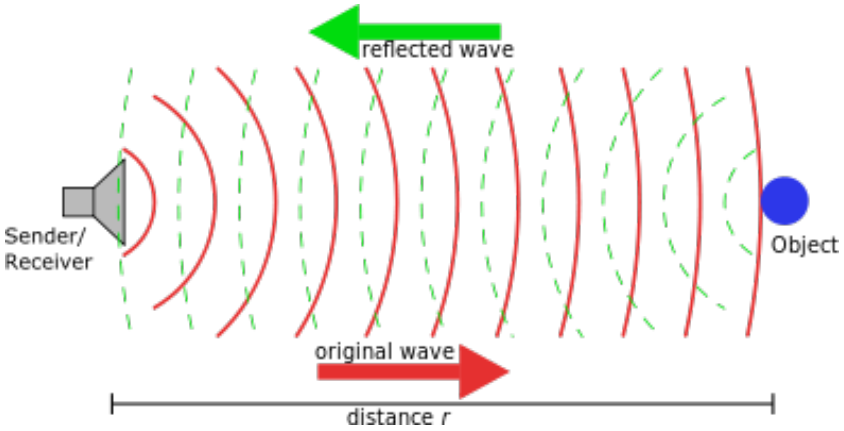

Figure 3.1: Active sound navigation and ranging (SONAR) system working principle. By comparing the *Original wave* with the *Reflected wave* the sensor is able to detect an object [82]

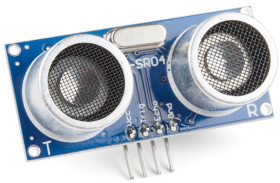

Figure 3.2: The HC-SR04, an ultrasonic sensor module that can be used for the human localization [42]

speaker-microphone system and a range between 25 kHz to 200 kHz for the ultrasonic sensors, meaning that the transmitted audio signal can not be heard by human ears.

The advantages of these systems are various: these systems are independent from most of the environment characteristics, such as light, smoke, dust, etc. while having the principal disadvantage of being incapable of detecting objects that are not in their line-of-sight, e.g., the target must be inside the area in which the sound waves propagates.

3.3 Passive Systems

The principal passive sound source localization systems involve the usage of microphone sensors, more precisely of **microphone arrays**, shown in Figure 3.3, which are any number of microphone sensors working in tandem. The sensors utilized are usually omnidirectional, but it is also possible to find array of directional

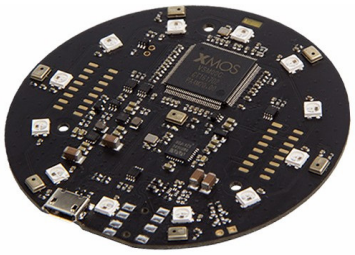

(a) ReSpeaker microphone array, a microphone sensor that can be used for the human localization [85]

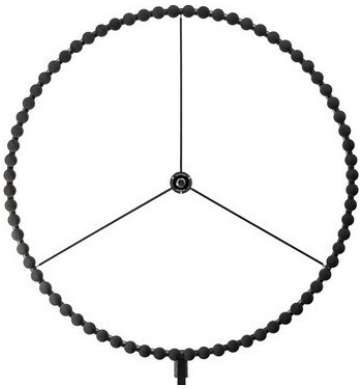

(b) Acoustic camera microphone array, sensor usually utilized for the sound localization in industrial machinery, in order to prevent the high emission of noise [86]

Figure 3.3: Microphone sensor arrays

microphones or formed by a mix of omnidirectional and directional ones.

A microphone is a transducer able to convert the sound in an electrical signal, by first converting the sound into mechanical motion using a diaphragm, and then converting this motion into electricity.

The objective of these systems is to localize the source of the sound, which in the field of human localization, is a person that produces sound, for instance walking in a particular type of terrain.

The sound source localization techniques are based on the 3D sound localization capability of the humans hearing system, that is able to locate a sound depending by its physical parameters: time, level (intensity) and spectral shape like it has been shown in the work of Risoud and colleagues [87].

The azimuth of the sound is determined by binaural factors, hence utilizing both hears to compute the interaural time and level differentials [87].

The height and depth distance are determined by monaural factors, hence utilizing just one hear. In the monaural hearing the brain computes changes in incident spectral shape [87].

Having information about the azimuth, elevation and distance of the sound, we are capable to estimate the sound source location, Figure 3.4.

Below, a list of all existing methods for sound source localization, proposed in [88]:

1. **Energy-Based localization**: utilized mostly in the wireless acoustic sensor network (WASN), the basic concept of this technique is to utilize the energy

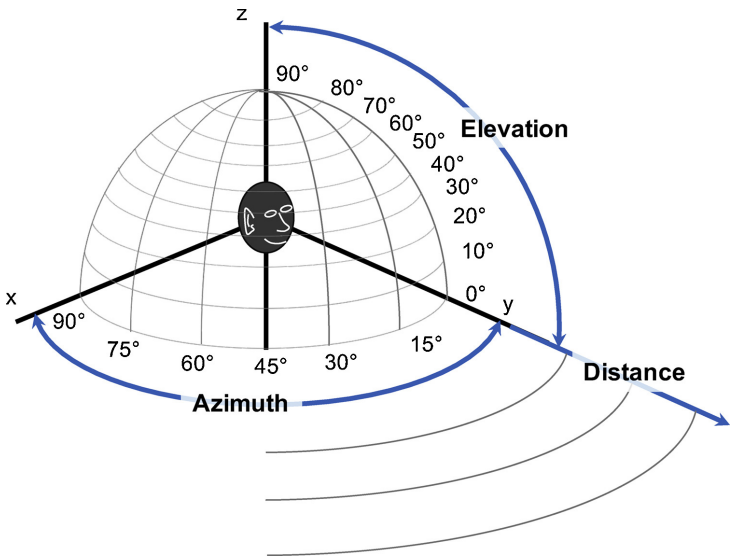

Figure 3.4: 3D system in polar coordinates centered on the hearer used to locate sound sources [87]

ratios of the sensors, restricting the sound source to a hypersphere. By increasing the number of sensors, the target will be at the intersection point of the hyperspheres [88].

2. **TOA**: defined as the time instant at which the microphones detect the source signal. This method is based on the time-of-flight (TOF) of the signal, which allows to understand the distance between the sensor and the target. The latter is calculated by depicting the time needed by the source signal to reach the microphone. By using different microphones it is possible to form equations, using the method of trilateration, which solution gives the intersection point that will be the position of the target [88].

3. **Time difference of arrival (TDOA)**: technique focused on the time difference between signals, also based on the TOF. In order to utilize this technique we need the measurements of time difference between TOA found by different microphones. This technique is strongly dependent by the synchronization between the different sensors, which can be achieved by choosing an optimal reference noise which also nullifies the noise factors. Moreover, like in the TOA method, the position of all the microphones must be known [88].

   An important assumption to be made in TOA and TDOA is that the sound signal travels from the target to the microphones along the shortest path. If this does not happen, e.g., the shortest path is blocked by an obstacle, the signal will take a longer path, resulting in an error of the estimated position.

4. **Direction of arrival (DOA)**: localization method aimed at estimating the direction of arrival of the sound signal, hence the angle of the sound wave with respect to the sensors array [88].

   The most widely method to determine the DOA is by using the **Delay-and-sum beamforming** techniques, both in time and in frequency domain.

   (a) Time domain delay-and-sum beamforming [89], which is based on the principle that the same sound will employ different amount of time to reach every different microphone of the array, which will result in a difference of delay and phases in the output measurement signals of each microphone. The delays can be computed considering the speed of sound and the distance between each microphone. By shifting the signal of each microphone by its proper delay, and then summing together all the signals which will now be in phase, it is possible to obtain a signal from which it is possible to estimate the DOA [90], Figure 3.5.

   (b) Frequency domain delay-and-sum beamforming [89], based on the same principles as in the time domain case, with the difference that now the signals will be mathematically manipulated considering their Fourier transform, which will let us work in the frequency domain instead of the time domain, Figure 3.6.

5. **Steered response power (SRP)**: this algorithm can be interpreted as a an approach based on beamforming that tries to search the candidate position for the sound source by choosing the one position that maximises the output of a steered delay-and-sum beamformer.

   More specifically, the sound source position will be chosen evaluating the objective function on a grid of possible positions that maps the environment observed by the sensors [88].

6. **Inter-microphone intensity difference (IID)**: usually implemented using a 2-microphones array, this method evaluates the difference of energy between the measurement signals in order to understand if the sound source is at right, left or in front of the sensor, Figure 3.7.

   The resolution of the measurement can be incremented utilizing an array which has more than two microphones of course.

   The signal evaluated by the IID is a time domain signal. Like for the Delay-and-sum beamforming technique, the signal can also be evaluated in the frequency domain, considering the spectrum of the signal, hence evaluating a inter-microphone level difference (ILD) [88].

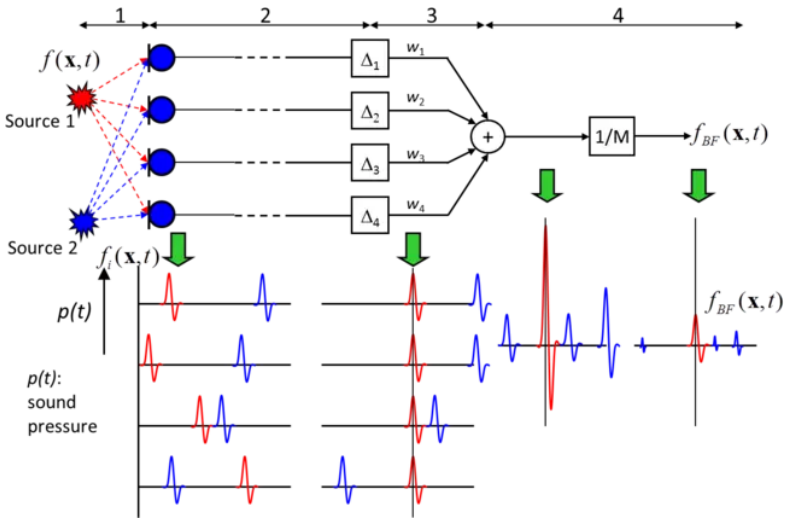

Figure 3.5: Delay-and-sum beamforming operation in time domain. In this technique, several microphones capture the sound which needs to be delayed since it will employ different time periods to reach each sensor. After delaying it, all the sound contributes that are now in phase will be summed in order to estimate the direction of arrival (DOA) of the source. All the operations are performed directly in the time domain of the signal [91]

In the work of Li [94], a visual tracking of human targets performed by means of a optical camera has been enhanced with acoustic tracking by performing the estimation of the DOA of the sound source.

This objective has been achieved by utilizing a system of seven MEMS microphones built in a system composed of field programmable gate arrays (FPGA) and advanced RISC machine (ARM) processor (where RISC stands for reduced instruction set computer (RISC)) for all the computations needed, Figure 3.8. The estimation of the DOA of the sound source will make the optical camera move towards the target in order to track it in real time, Figure 3.9.

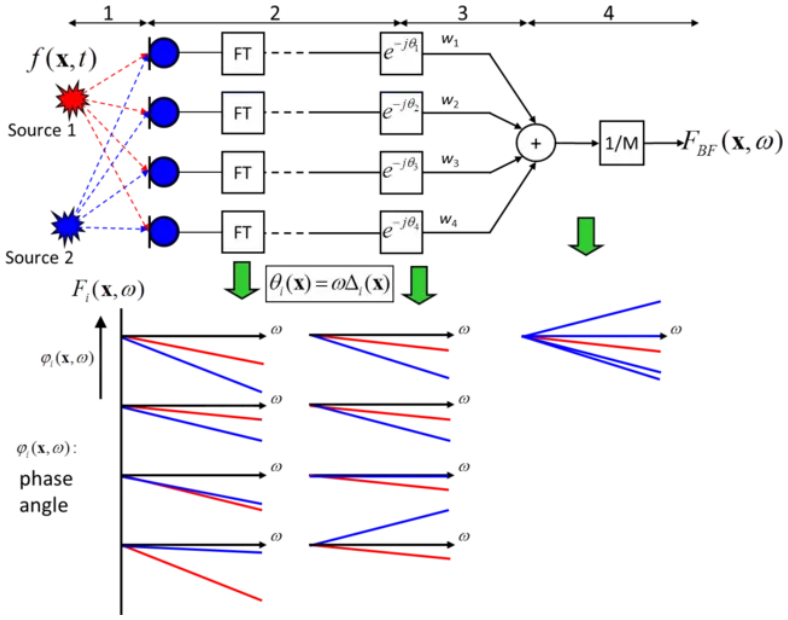

Figure 3.6: Delay-and-sum beamforming in frequency domain. In this technique, several microphones capture the sound which needs to be delayed since it will employ different time periods to reach each sensor. After delaying it, all the sound contributes that are now in phase will be summed in order to estimate the direction of arrival (DOA) of the source. All the operations are performed in the frequency domain by performing a fast-Fourier transform (FFT) operation [92]

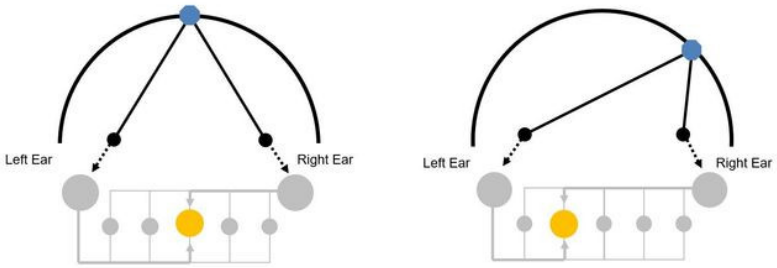

Figure 3.7: Inter-microphone intensity difference (IID) technique, in which the sound intensity of the two hears of the hearer is compared in order to localize the sound [93]

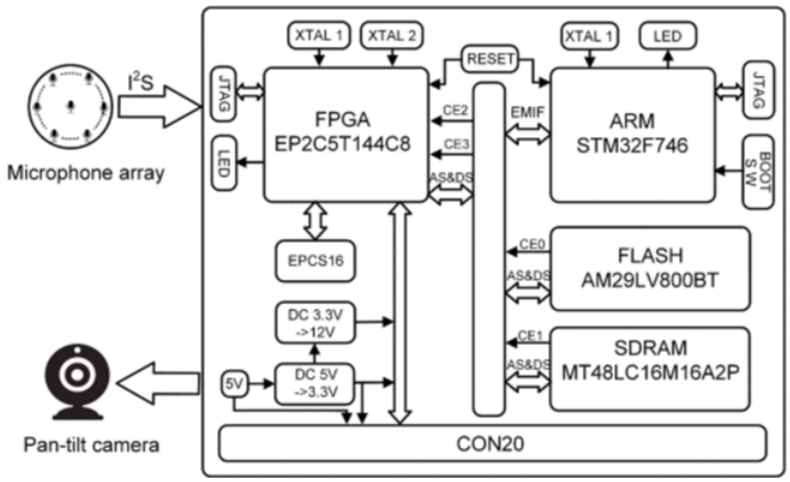

Figure 3.8: System set-up of acoustic enhanced camera tracking employed in [94] composed of a microphone array that is able to estimate the direction of arrival (DOA), estimate that is then used to move a pan-tilt camera in order to follow the "heard" target. To achieve this, the output of the array is fed to a field programmable gate arrays (FPGA) system that controls the camera.

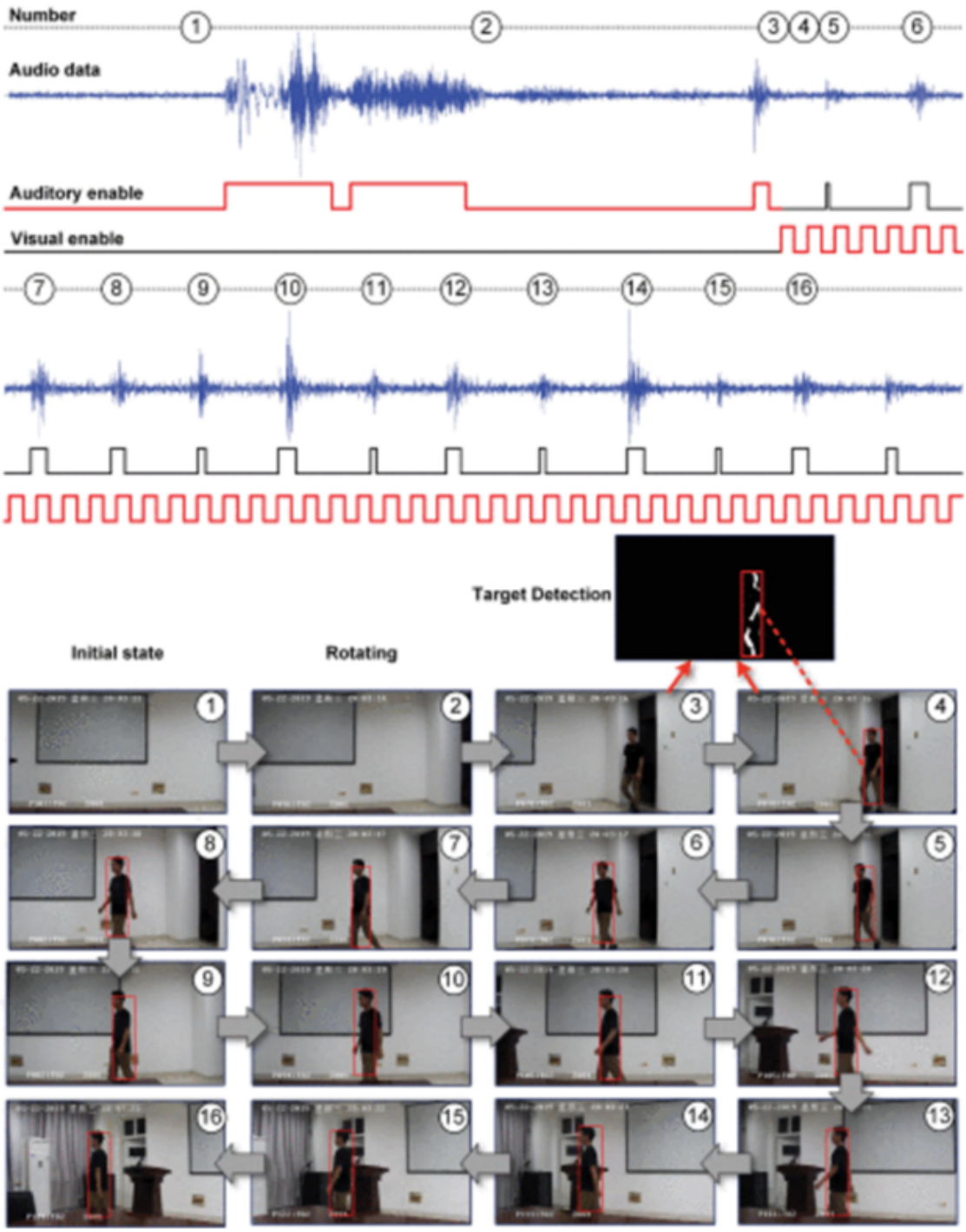

Figure 3.9: Results obtained in Li's experiments [94]. On the top part all the audio data of the located target extracted from the microphone array. In the bottom part, the human tracking performed by turning of the camera

Chapter 4

RADAR

4.1 RADAR Fundamentals

RADAR [95], acronym for "Radio Detection And Ranging", is a radio waves-based detection system, which is able to determine the distance, angle, and velocity of objects in its detection range.

A radar system, shown in Figure 4.1 is composed of a transmitter that produces radio waves and a receiver, which receives the echoes of the initial waves. Finally, a processor will be responsible for the elaboration of the received signal in order to depict the information needed.

The transmitted (TX) radio waves, upon hitting an object, will be absorbed by it, or will be reflected or scattered in many directions; those waves which will be reflected back to the receiver are the ones that will be analyzed by the sensor. Materials with high electrical conductivity, such as metals, will reflect better the radio waves.

Radar sensors can be classified into two types, based on the radio wave that is transmitted by it [95]:

1. **Pulse radar**, usually characterized by the presence of a single antenna, that will work in transmitting or receiving mode, regulated by a duplexer, which will alternate the two operating modes on a periodic basis. The antenna will transmit a pulse every clock pulse, after that, the duplexer will switch to receiving mode, in order to receive the echo signal at the next clock pulse.

2. **Continuous wave (CW) radar**, characterized by the presence of two antennas, one for the transmission and the other for the reception. These radars work with a continuous transmission of the radio signal, hence the differentiation of transmitter and receiver. The transmitted wave can be **unmodulated** or **modulated**.

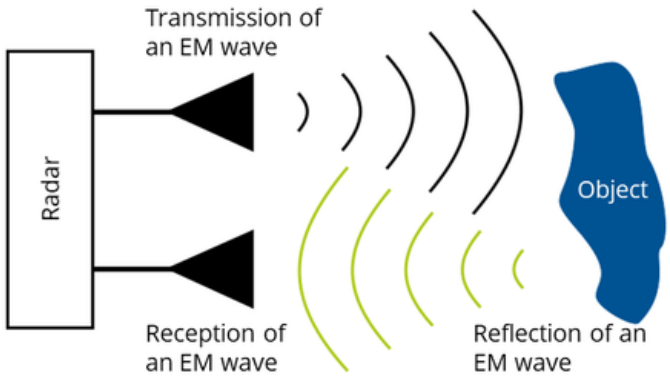

Figure 4.1: Radar basic working principle: The object is detected by comparing the transmitted (TX) and the received (RX) electromagnetic wave [96]

(a) **Unmodulated CW**: These radars transmit a radio wave which is not modulated and will exploit the *Doppler effect*, which is the change in frequency of the received echo wave when a moving object have been encountered by the latter, Figure 4.2.

The Doppler frequency change depends on the speed of light in the air c′ and the speed of the target v and is equal to (4.1):

$$fr = ft\frac{(1 + v/c')}{(1 - v/c')} \tag{4.1}$$

where *fr* is the observed frequency and *ft* is the original emitted frequency.

These type of radars hence, also called Doppler radars, can not detect stationary targets because they will not trigger the Doppler effect and, moreover, are not able to depict the distance of the non-stationary objects detected. The Doppler radars are only able to detect the velocity of the detected non-stationary objects, in fact, they are typically employed in competition sports like golf, car racing, baseball, etc.

(b) **Modulated CW**: explained in the next section.

4.2 Frequency-Modulated Continuous Wave Radar

FMCW radars are a type of modulated CW sensors that, differently from the unmodulated ones are able to depict the distance of the detected object with a fairly high accuracy [98] [99].

Often used as altimeters in air-crafts to measure the height during the landing process, these radars transmit a modulated signal, which consists of a continuous

Figure 4.2: Radio wave signal which changes frequency due to *Doppler effect* caused by the movements of the detect objects [97]

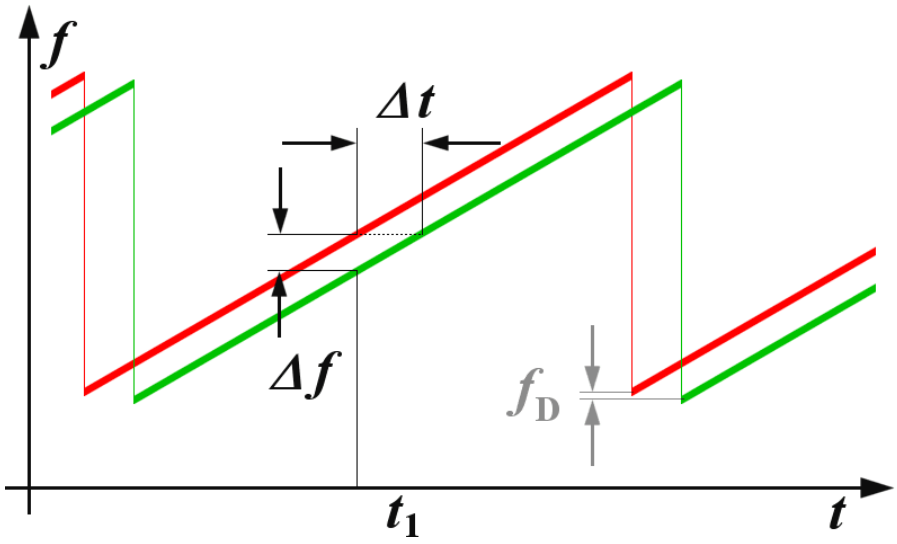

Figure 4.3: Working principle of frequency-modulated continuous wave (FMCW) radars. Δt is the time difference, Δf is the frequency difference between transmitted (TX) and received (RX) signal, and f_D is the frequency shift due to *Doppler effect* [100]

wave of a known stable frequency which increases and decreases over a fixed period of time. By computing the difference between the received (RX) and the TX signal it is possible to compute the range between the sensor and the detected objects.

If the detected object is moving with respect to the radar, like in CW radars, the Doppler effect will take place, causing a frequency shift in the received signal proportional to the radial speed of the target, which will show a higher frequency if the target is approaching the radar and lower frequency in the opposite case.

The working principle of FMCW radars is shown in Figure 4.3, where Δt is the time difference between received and TX signals, Δf is the frequency difference and f_D is the frequency shift caused by the Doppler effect.

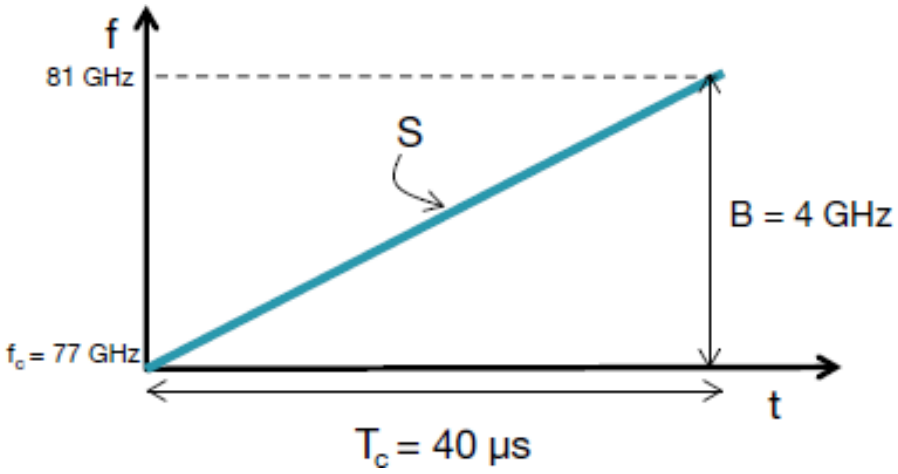

Figure 4.4: Basic chirp signal with frequency as function of time, with starting frequency of 77 GHz and ending frequency of 81 GHz. S is the slope of the signal [98]

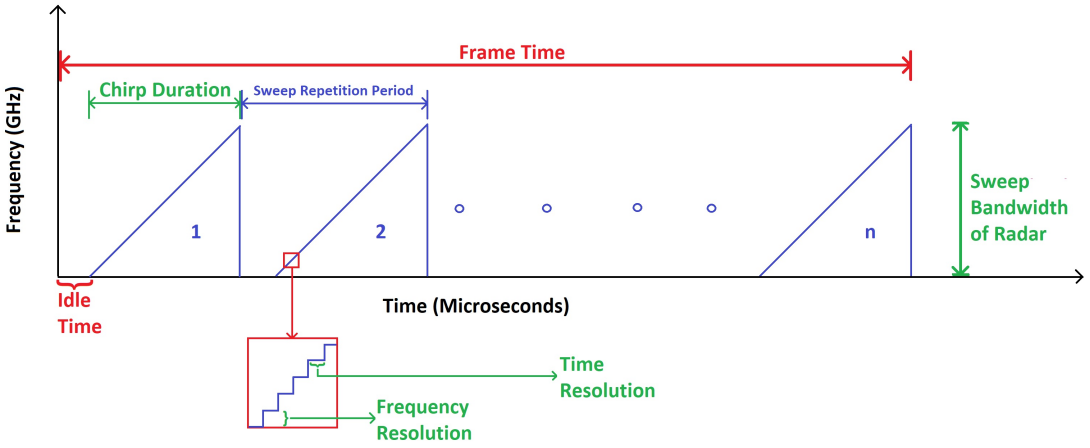

Figure 4.5: Chirp signal of a generic radar with frequency as function of time [101]

The basic radar signal is called “chirp”, shown in Figure 4.4, having S as the slope that indicates the rate of change of frequency, that represents the sinusoidal wave with a frequency that is increased within a time window T_c.

The signal of the radar will be formed by a repetition of chirps with always the same starting and ending frequencies Figure 4.5.

The basic system of an FMCW is presented in Figure 4.6 where:

1. Represents the synthesizer, which is responsible for the chirp generation

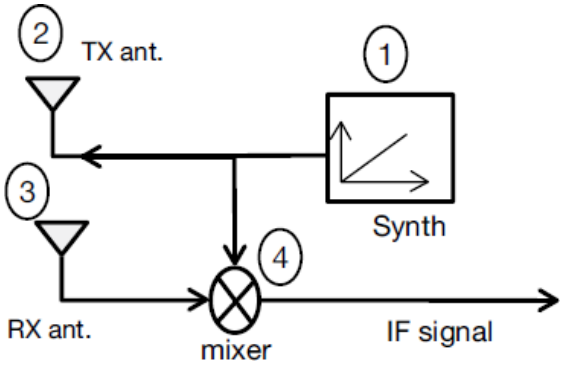

Figure 4.6: Block diagram of a frequency-modulated continuous wave (FMCW) radar. The synthetizer is responsible for the chirp generation, the mixer mixes received (RX) and transmitted (TX) obtaining in output the intermediate frequency (IF) signal, which is analyzed to find target(s) [98]

2. Is the transmitter antenna, which transmits the chirp signal
3. Is the receiving antenna, which captures the reflected chirp
4. Is the mixer, which combines the TX and RX signal in order to obtain the sensor output

The result of the mixer will be an intermediate frequency (IF) signal, whose Fourier transform results in a beat signal. The frequency of this signal, which is constant and equal to $S * \tau$, with τ being the time delay between TX and RX signal, as can be seen in Figure 4.7, is the one utilized in order to depict the range of the detected target. If more than one target is detected, the IF signal will comprise multiple sinusoids with different frequencies, each one corresponding to a particular target, Figure 4.8 [99].

The range of the targets [99] detected by the sensor is depicted using (4.2):

$$R = \frac{(C \cdot T_c \cdot f_b)}{(2 \cdot B)} \tag{4.2}$$

where R = target distance, C = speed of light of vacuum, T_c = up-chirp time, f_b = beat frequency corresponding to the target, B = bandwidth of the signal.

The Doppler effect will produce a change in the phase of the IF output signal from one chirp to another, which is proportional to the radial velocity v_r of the target and can be computed using (4.3) [98].

$$\Delta w = \frac{(4 \cdot \pi \cdot v_r \cdot T_c)}{\lambda} \tag{4.3}$$

where λ = wavelength (m)

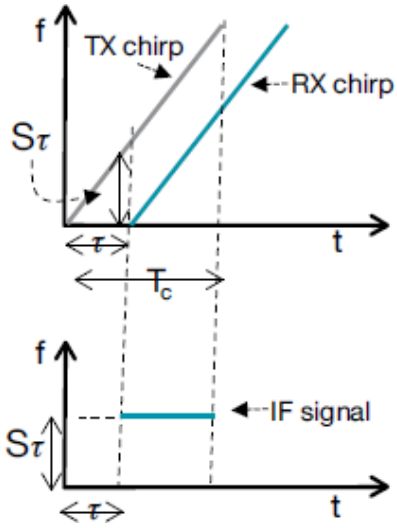

Figure 4.7: Intermediate frequency (IF) resulting from the mixer output, a signal with constant frequency [98]

From (4.3) it is possible to compute the radial velocity [98] of the target which can be computed using (4.4).

$$v_r = \frac{\Delta w \cdot \lambda}{(4 \cdot \pi \cdot T_c)} \tag{4.4}$$

When measuring the velocity of the detected target, it could happen that the phase difference between difference chirps do not respect the constraint $|\Delta \mathrm{w}| < \pi$, causing the radar not being able to understand the velocity. This happens because the phase difference is periodic of 2π. This means that every radar has an upper bound for the detectable velocity, meaning that if the $\Delta \mathrm{w} = \pi$ the maximum velocity manageable [98] is (4.5):

$$v_{max} = \frac{\lambda}{(4 \cdot T_c)} \tag{4.5}$$

The maximum velocity limit can be increased by having closer chirps, hence decreasing $\mathrm{T_c}$.

As previously stated, the signal transmitted by radar is composed of multiple chirps, N called frame window.

When dealing with multiple targets the radar will be able to distinguish between them, hence the Fourier transform of the IF signal will present two separated peaks at different frequencies, if the resolution [98] (4.6) is respected.

$$\Delta v = \frac{\lambda}{(2 \cdot N \cdot T_c)} \tag{4.6}$$

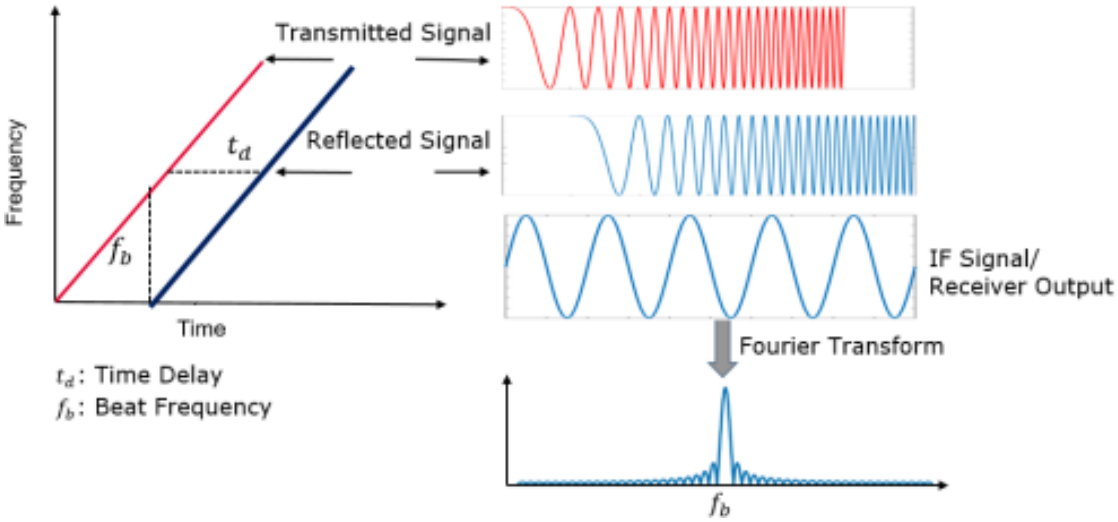

Figure 4.8: Receiver output of a radar sensor, showing the beat frequency from which it is possible to extract the target range [99]

The resolution in (4.6) represents the minimum velocity difference between two objects that the radar is able to sense.

The last information that these radars are able to depict is the angle of arrival (AoA) of the received signal, with the note that this information can only be obtained if multiple antennas are present, hence the sensor must be a multiple input multiple output (MIMO) radar, Figure 4.9. From the latter statement, we observe that the sensor must have at least two receiving antenna in order to determine the angle.

Supposing that only one target is present in front of the radar, it is possible to use the phase difference of the RX signal of the different antennas to compute the angle of the detected object.

More specifically, the different receiving antennas will receive the same copy of the reflected signal, but due to the distance d between the antennas, the copies will have a phase difference [98]. By mixing the TX signal and the different copies of the RX signal and by operating the Fourier Transform of the IF signal, the output signals will be composed of the peaks in the same position, but with a difference in phase, which is (4.7).

$$w = \frac{2 \cdot \pi \cdot d \cdot \sin(\theta)}{\lambda} \tag{4.7}$$

by inverting (4.7) we are able to estimate the angle of the detected object [98], which is (4.8).

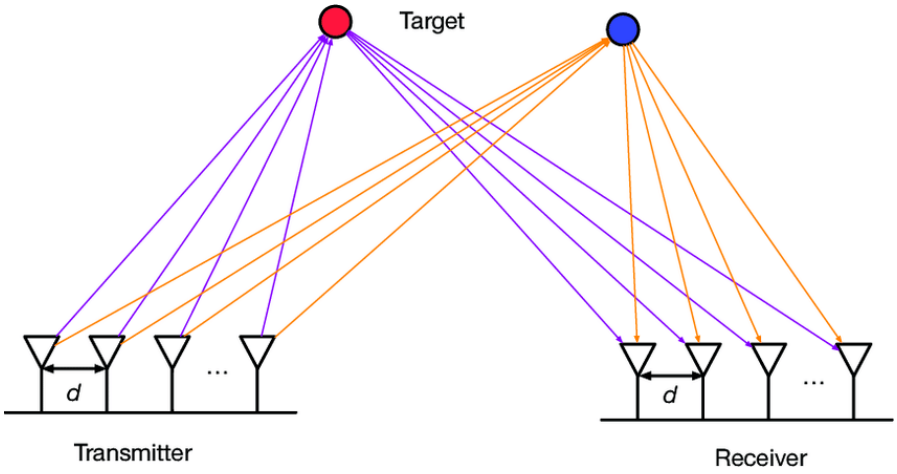

Figure 4.9: Multiple input multiple output (MIMO) radar sensor [102], able to detect the angle of arrival (AoA) of the target(s) due to the presence of more than one transmitted (TX) and received (RX) antennas

$$\theta = \sin^{-1}\left(\frac{\lambda \cdot w}{2 \cdot \pi \cdot d}\right) \tag{4.8}$$

Like in the velocity case, there is an upper limit in the detectable angle of arrival of the target [98], which is when w = π, which is (4.9).

$$\theta_{max} = \sin^{-1}\left(\frac{\lambda}{2 \cdot d}\right) \tag{4.9}$$

Chapter 5

Human Localization via Radar Sensors

5.1 Infineon Radar Demo Position2Go

The Demo Position2Go, Figure 5.1, is a complete sensor evaluation board made by Infineon, which is essentially based on the 24 GHz transceiver chipset BGT24MTR12 and by the 32-bit ARM® Cortex™-M4 XMC4700 microcontroller [66][99][104].

The demo kit is complete with a demonstration firmware to be flashed in the sensor, which can be modified using the DAVE™ toolchain, and a GUI, which can be used in order to display the detected targets in real time, as well as modify the radar transmitted signal (bandwidth, up-chirp time, transmission and reception power levels, etc).

The core of the sensor is the transceiver chip, a radar that operates in the 24 GHz bandwidth. All the technical information of such chip has been exposed in the Table 2.4.

The evaluation kit, equipped with one TX antenna and two RX antennas, is capable to detect the position, angle, distance, and velocity of moving and not-moving targets, up to five targets at the same time. It also includes target-tracking capability implemented via algorithms running directly on the on-board MCU.

The measured and processed data can be sent via universal serial bus (USB) cable directly to a computer, also responsible for the power supply, which will be then in charge of only visualizing those results using the GUI.

Below, the full list of the embedded components in the Position2Go sensor [99]:

1. BGT24MTR12, 24 GHz transceiver
2. XMC4700 MCU

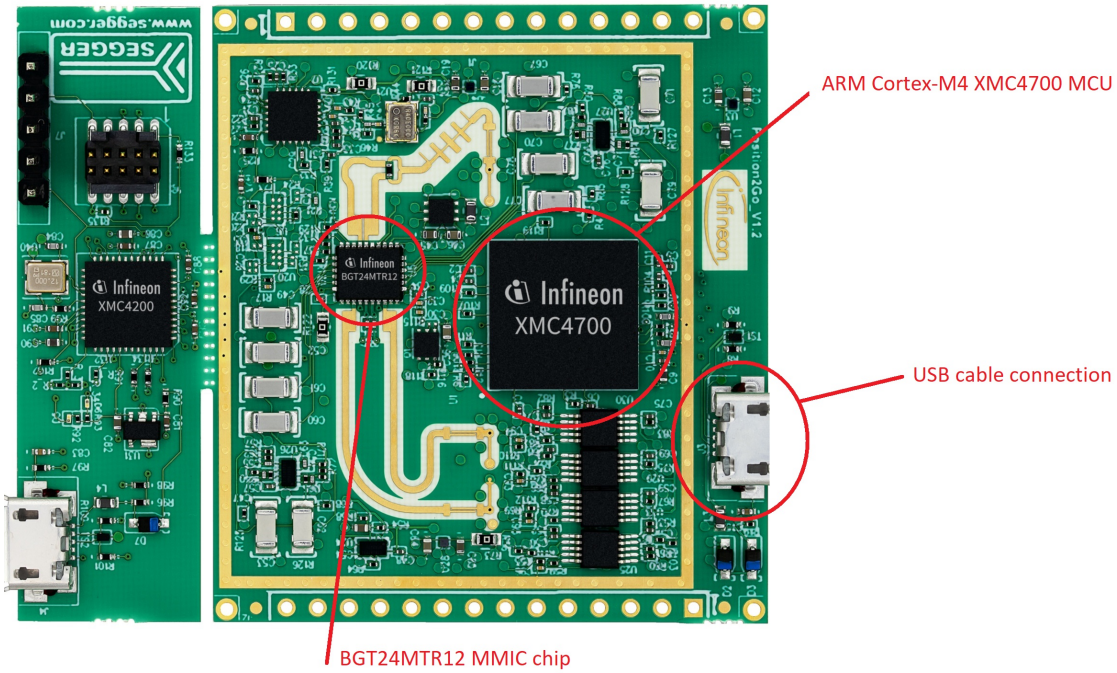

Figure 5.1: Top view of Demo Position2Go, with highlighted monolithic microwave IC (MMIC), microcontroller unit (MCU) and the universal serial bus (USB) cable connector, needed to let the sensor communicate with the host computer. On the left part of the sensor, the breakable debugger, that must be connected when the sensor needs to be flashed [103]

3. LMX2491, Phased locked loop (PLL)
4. PGA112, Programmable gain amplifier (PGA)

In order to enable communication with these components, the firmware configures the following peripherals [99]:

1. ADC
2. Direct memory access (DMA)
3. General-purpose input output (GPIO)
4. Capture and compare unit (CCU)
5. Hardware/Software interrupts
6. USB interface

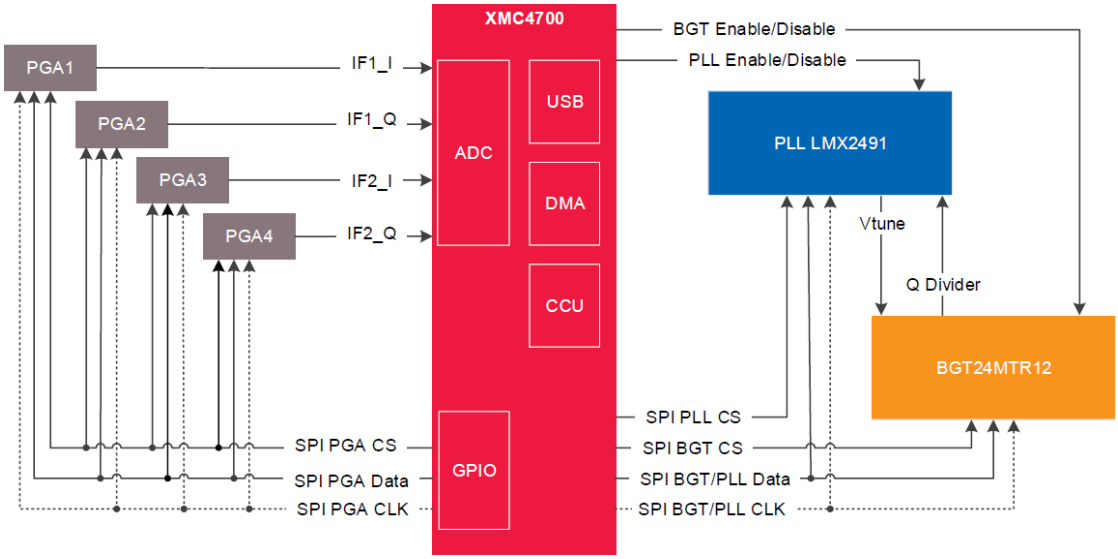

Figure 5.2: Position2Go components block diagram, where, besides the basic components of the microcontroller unit (MCU) are visible, the programmable gain amplifiers (PGAs) that amplify the intermediate frequency (IF) signals that are then sampled by the analog to digital converter (ADC) are shown. Also, the phased locked loop (PLL) which starts the chirp generation and the monolithic microwave IC (MMIC) can be seen. [99]

Figure 5.2 shows all the embedded components of the sensor considering also the communication protocols.

Position2Go firmware is characterized by repetitive and non-repetitive actions, shown in Figure 5.3. The core of the flow diagram is the main loop, that the program leaves only when a frame timer interrupt or a GUI request is received, which will cause some specific actions depending on what has been received, only to have the execution returns to the loop after those actions have been completed.

More specifically, the steps shown in Figure 5.3 are [99]:

- **Device initialization**: First task executed by the device only at the start of the latter. In this step, all the MCU peripherals are initialized.
- **Frame timer interrupts**: Internal trigger of the chirp generation phase over PLL
- **Raw data acquisition**: Start of the collection of raw data from the radar
- **Radar algorithm**: Computation of the parameters of the detected target(s)

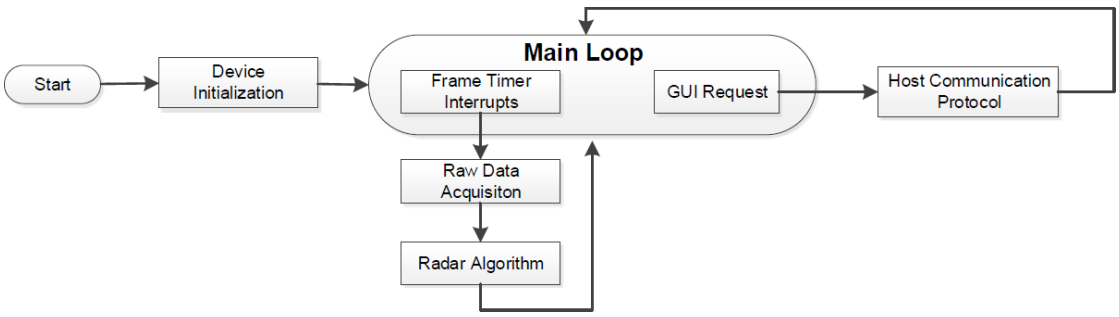

Figure 5.3: Position2Go firmware flow diagram, where the principal tasks performed by the microcontroller unit (MCU) are shown [99]

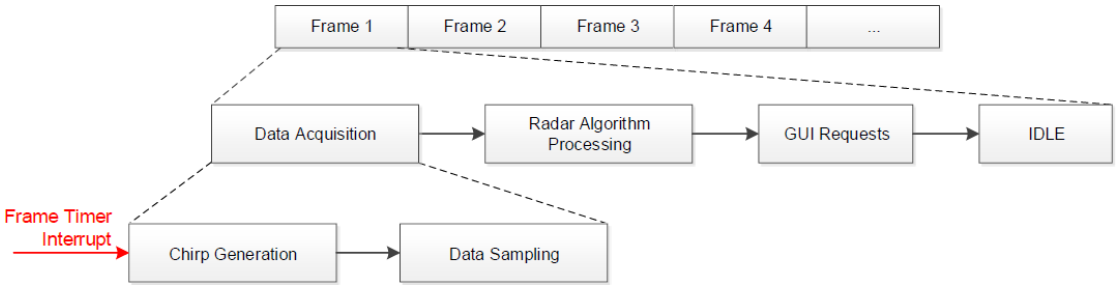

Figure 5.4: Position2Go data acquisition flow diagram [99]

5.1.1 Raw Data Acquisition

As shown in Figure 5.4 the raw data acquisition task can be further divided into two tasks

- **Chirp generation**: this process is triggered by an internal frame timer, enabling the generation of the chirps over PLL.

  The whole process can be depicted in Figure 5.5.

  Below a description of the blocks present in Figure 5.5 [99]:

  - **Configure and enable DMA**: set-up of the DMA source/destination addresses, more specifically, four DMA channels are configured for the two RX complex data samples Q1, I1, Q2, I2.
  - **Trigger PLL high**: rising edge of the signal which controls the PLL, which will start the PLL ramping.
  - **Start ADC timer**: started by the rising edge of PLL controlling signal, this timer is used in order to have equidistant ADC samples.
  - **Trigger PLL low**: falling edge of the PLL controlling signal.

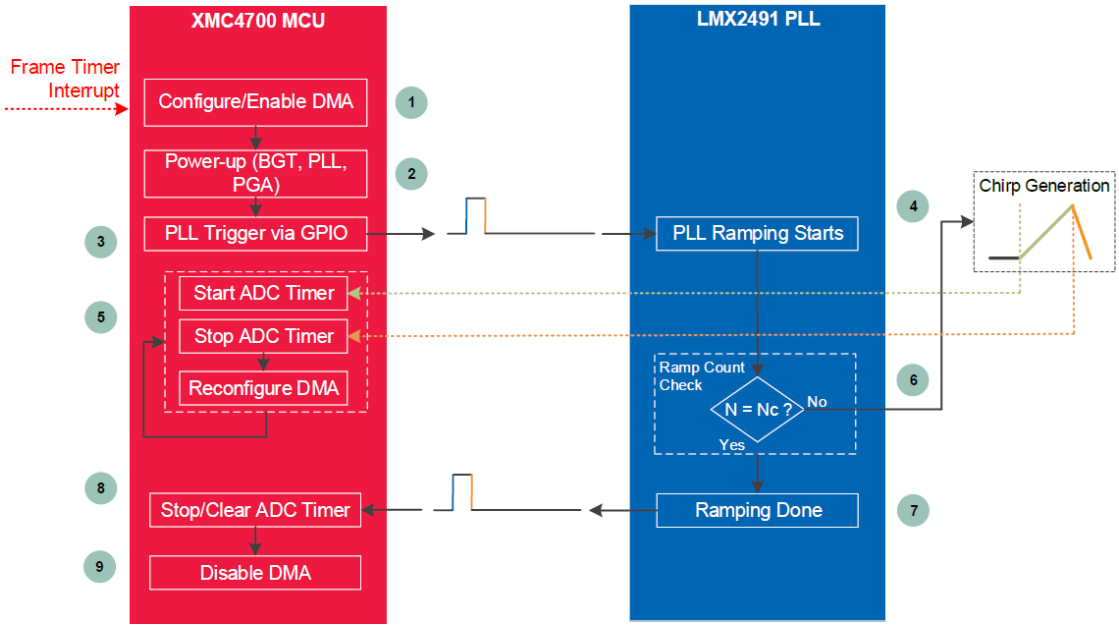

Figure 5.5: Position2Go chirp generation flow diagram, having on the left the microcontroller unit (MCU) and on the right the phased locked loop (PLL) [99]

The result of the generation task will be the chirp signal shown in Figure 5.6.

- **Data sampling**: at the same moment of the PLL start of the generation of chirps, the ADC is triggered to start sampling the data from the RX antennas. As previously stated, the sampled complex data will be moved by the DMA using four different channels until the number N_s of required samples is reached, causing the stop of the DMA transfer. The whole data sampling process can be seen in Figure 5.7.

  Each IF signal received by the antennas is digitized by the ADC to a complex I/Q signal, with I being the In-phase signal and Q being the Quadrature signal.

5.1.2 Radar Algorithm

The radar algorithm can be divided into different blocks, Figure 5.8. The algorithm takes the raw data measured by the radar and produce as output the target(s) parameters. More specifically, the basic steps of the software are [99]:

1. **Raw data acquisition**: raw data are collected in a 2D matrix containing slow and fast time samples.

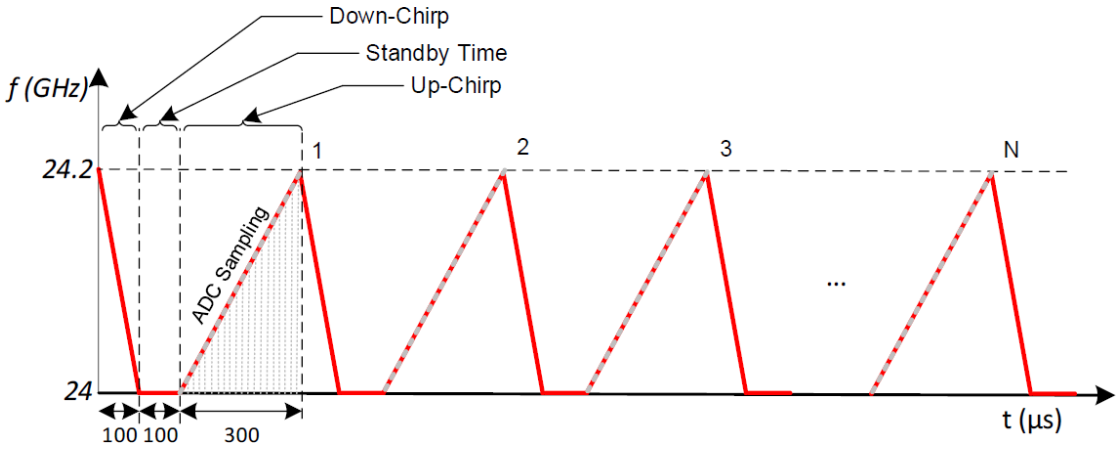

Figure 5.6: Position2Go chirp generation resulting signal, showing the chirp times, namely *Down-chirp time*, *Standby time*, *Up-chirp time* [99]

2. **Window Across Range**: first step of the algorithm consists of the application of a Blackman window across the range dimension (fast time samples). This results in an enhancement of the signal-to-noise ratio (SNR) and in the removal of the side lobes of the signals.

3. **Zero padding**: technique in which a sequence of zeros is added to the end of the input sequence in order to have the output sequence size equal to a power of two. This technique improves the input signal characteristic.

4. **Range fast-Fourier transform (FFT)**: generation of an FFT range image by performing the FFT of the signal.

5. **Target detection**: in this step the algorithm searches for peaks in the range FFT image in order to depict the target(s) range.

6. **Doppler FFT**: this step involves the same steps performed for the fast time samples in order to depict the target(s) range. More specifically, the doppler dimension is represented by the slow time samples.

   First, a Chebyshev window is applied to these time samples in order to improve SNR. Then the zero-padding operation is performed and finally, the FFT is computed in order to obtain the complete range Doppler map.

7. **Angle estimation**: since the Position2Go comprises more than one RX antenna, the AoA of the target(s) can be computed.

   In order to do so, the phase difference of the range Doppler maps obtained from the two receivers is computed, which is then used to compute the target angle using (4.8). The whole angle estimation process is shown in Figure 5.9.

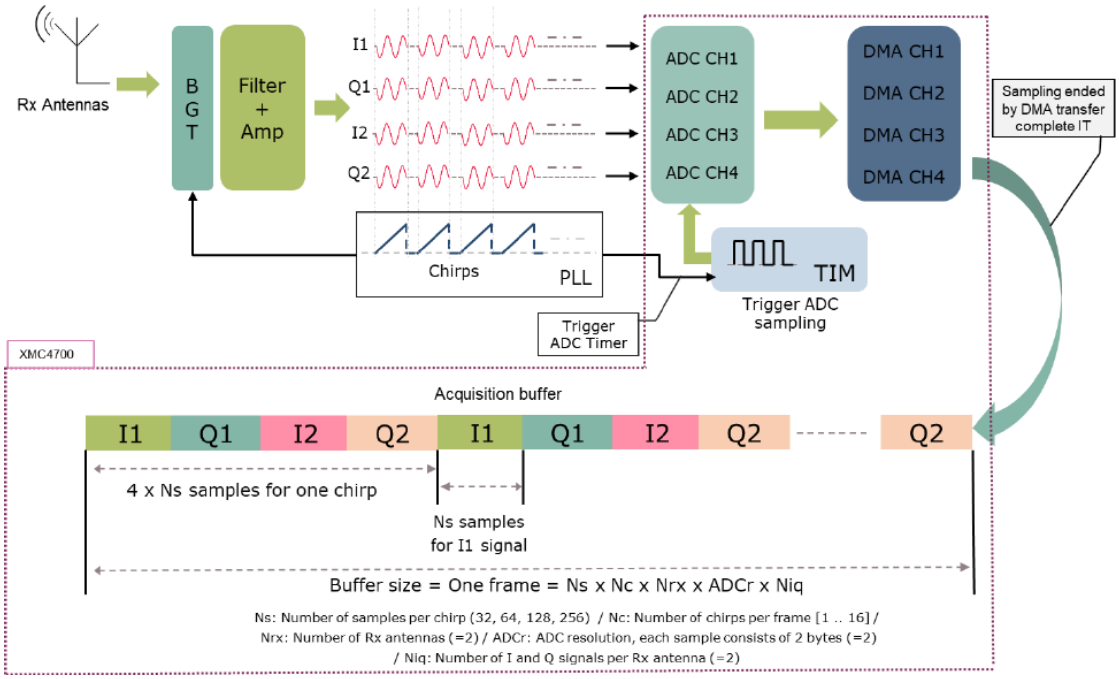

Figure 5.7: Position2Go full data acquisition and sampling process where the four intermediate frequency (IF) signals can be seen [99]

8. **Target tracking**: at the end of the above-mentioned processing steps, the algorithm obtains the range Doppler and angle parameters of the target(s) that have been detected for each frame. Then, a strongest nearest neighbor (SNN) approach is applied to associate the obtained measurements with the different tracks following the principle that the most similar measurements must be associated with the same track.

   Finally, in order to track in real-time the moving targets, an Alpha-Beta tracker is implemented, which is a filter really close to Kalman Filters that estimates the future location of the target(s).

5.1.3 Power Saving

In order to decrease the overall power consumption and the thermal dissipation of the sensor, there is the possibility to operate the BGT24MTR12 in a duty-cycle mode.

When the duty-cycle mode is enabled, the BGT module and the PLL module will be the ones to be activated/de-activated, following pre-determined delays specified in the firmware.

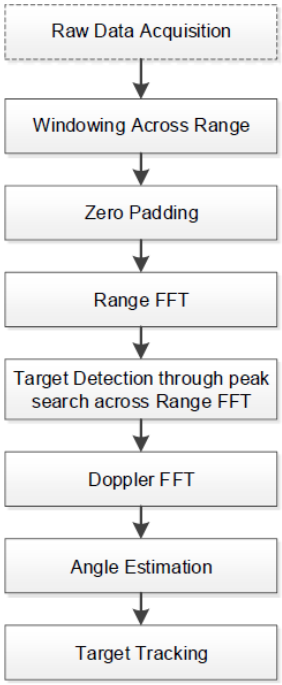

Figure 5.8: Position2Go radar algorithm block diagram [99]

5.2 Infineon Position2Go Graphical User Interface

The Position2Go sensor, as previously stated, is operated utilizing the software provided by Infineon, the Radar GUI, Figure 5.10.

The GUI shows in real-time a "Radar-like" plot, which gives us real-time information of all the targets being detected at that moment, providing all the measured parameters, hence the distance, angle, velocity, and FFT magnitude of the peak that represents the specific target. It also gives an insight of the TX and RX signals in frequency and time domain.

The software also offers the possibility to modify the working parameters of the radar sensor while the latter is operating. The modifiable parameters affect the radar sensing capabilities, for instance, it is possible to modify the up-chirp time and the bandwidth in order to change the maximum detectable target distance, the TX antenna power level, etc. Besides the sensor parameters, it is also possible to modify the maximum and minimum range and velocity admissible in the detected targets, minimum velocity, and range threshold.

There is also the possibility to enable/disable the duty cycle mode, the moving target indication (MTI) filter, which will filter out static objects from the detected

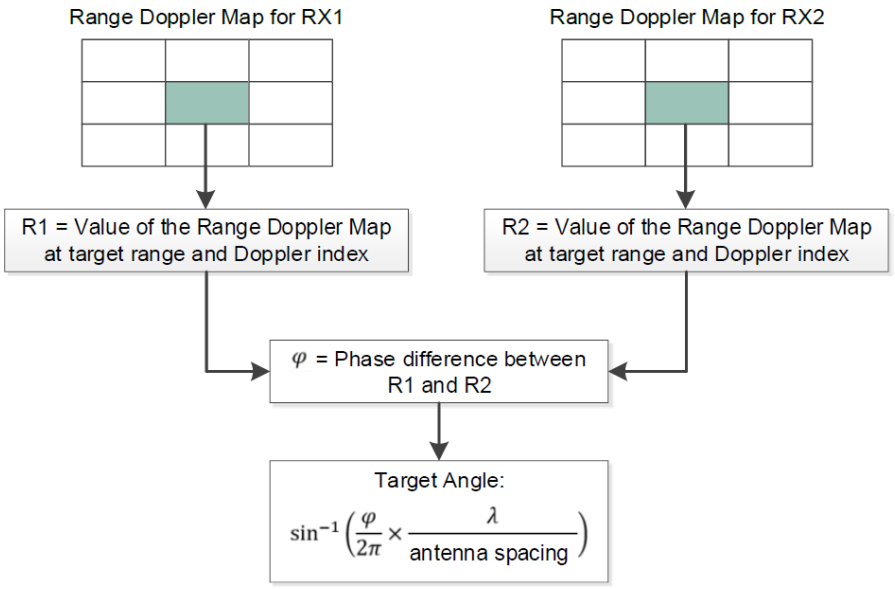

Figure 5.9: Position2Go angle estimation process, focused on the computation of the phase difference φ between the signals of the two receivers [99]

targets, and the tracking algorithms for moving targets.

The GUI offers also the possibility to re-calibrate the sensor, a very important task to perform every time the TX power level or the RX PGA level is modified or when the environment temperature changes, since the measurement are dependent by the latter. There are two types of sensor calibration data, which are stored in the appropriate target memories, e.g., FLASH memory or static random access memory (SRAM) memory of the sensor, which are ADC calibration data and algorithm calibration data. In the first one, the ADC raw data for RX1 and RX2 antennas are used in order to calibrate the first chirp of the sensor, while in the second one, the calibration is done by means of a range or angle offset added to the measurements.

The last feature of the tool is the capability to record and export all the data of the measurements by pressing the Recording/Stop button, in order to process these data with an external software such as MATLAB. The exported data can also be processed and visualized again by the Infineon software in order, for instance, to verify the accuracy of the same raw data elaborated by external software.

5.3 Texas Instruments Radar IWR6843ISK

The IWR6843ISK in Figure 5.11, is a complete sensor evaluation board based on the IWR6843 60 GHz to 64 GHz band FMCW radar [63][106][107][108][109][77]. The kit comes with several firmwares in order to test the various capabilities of the

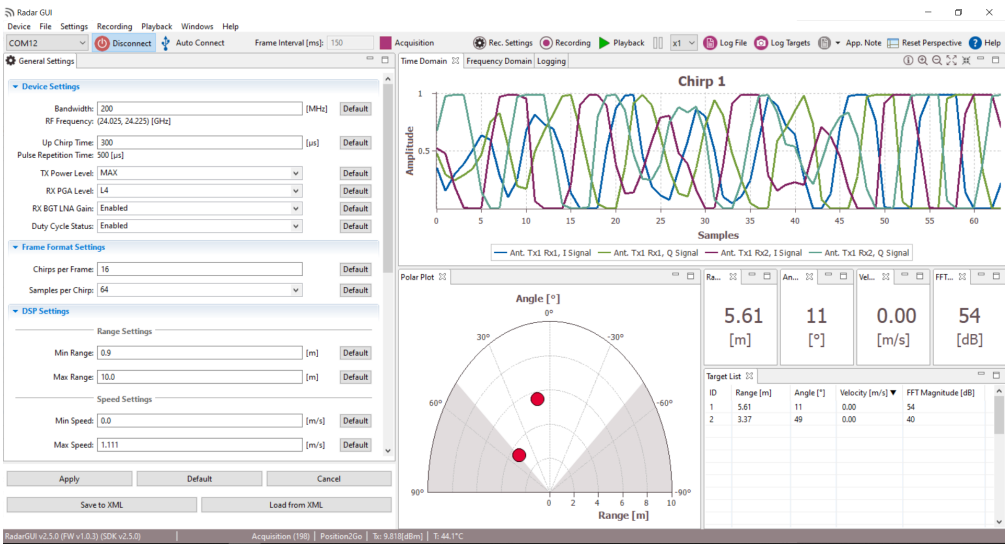

Figure 5.10: Position2Go Infineon Radar graphical user interface (GUI) software, having at the left part all the configurable parameters, on top the received (RX) chirp 1, and in the bottom the radar view of the targets

sensor, as well as visualization programs complete with GUI and software utilities needed to test and select the best configurations in terms of radar TX signal. All the technical information of the transceiver chip which operates in the band of 60 GHz is exposed in Table 2.4.

The evaluation kit, whose functional block diagram is shown in Figure 5.12, presents three TX and four RX antennas, resulting in an FoV of 120° in azimuth and 30° in elevation.

The hardware of the development kit can be divided into sub-systems, which are [63]:

1. **Radio frequency (RF) and analog sub-system** including the RF and the analog circuitry which is formed by the ADC, the synthesizer, the mixer IF, the power amplifier (PA), the low noise amplifier (LNA) [63].

2. **Clock sub-system**, which is responsible for the generation of the input reference for the 60 GHz to 64 GHz signal to transmit. The input is in fact generated by an oscillator circuit that produces a 40 MHz signal, which then passes by a X3 multiplier in order to obtain the required frequency. Moreover, in this sub-system is also present a PLL that provides to the host processor a reference clock after the system wake-up [63].

3. **Transmit sub-system**, made by three independent amplitude and phase control parallel transmit chains. The sensor can support 6-bit linear phase

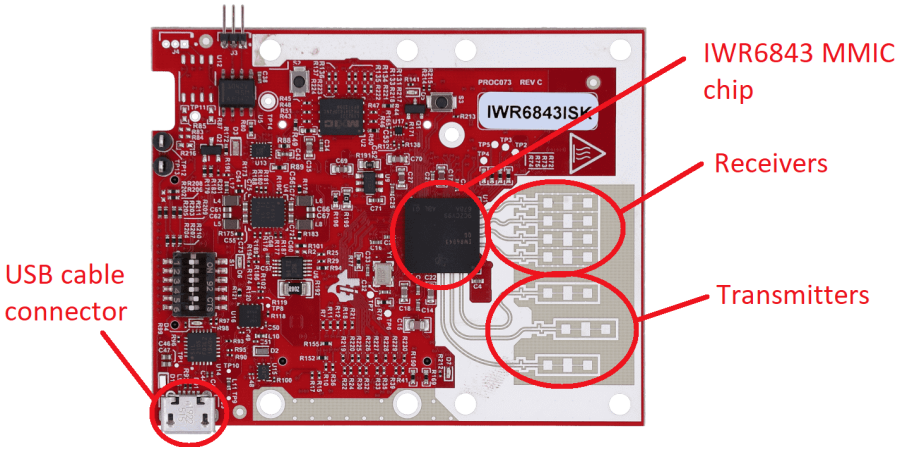

Figure 5.11: Top view of IWR6843ISK, with highlighted monolithic microwave IC (MMIC), onboard antennas, and the universal serial bus (USB) cable connector, needed to let the sensor communicate with the host computer [105]

modulation for MIMO radar, interference mitigation and TX beamforming applications [63].

4. **Receive sub-system**, consisting of four parallel channels that can be operated at the same time, each one formed by LNA, mixer, IF filtering, ADC, decimation. The receiving system of the sensor is operated in a complex baseband architecture, meaning that each receiver provides I and Q signals as output [63].

5. **Processor sub-system**, that at high level can be divided in two customer programmable sub-systems, where the first one is the digital signal processing (DSP) sub-system containing the high-performance C674X DSP, high-bandwidth interconnect, hardware accelerator and associated peripherals, and the second one is the main sub-system, which controls all the sensor peripherals and all the activities carried out by the sensor. The latter is composed by the ARM® Cortex™-R4F processor and the associated peripherals like the DMA, universal asynchronous receiver-transmitter (UART), pulse-width modulation (PWM), etc [63].

6. **Host interface**, which can be provided through serial peripheral interface (SPI), UART or controller area network flexible data-rate (CAN-FD) interface [63].

7. **Hardware accelerator**, an instruction pointer (IP) that softens the computational load of the main processor by executing certain frequently used computations in FMCW radar signal processing, which consists of FFT and

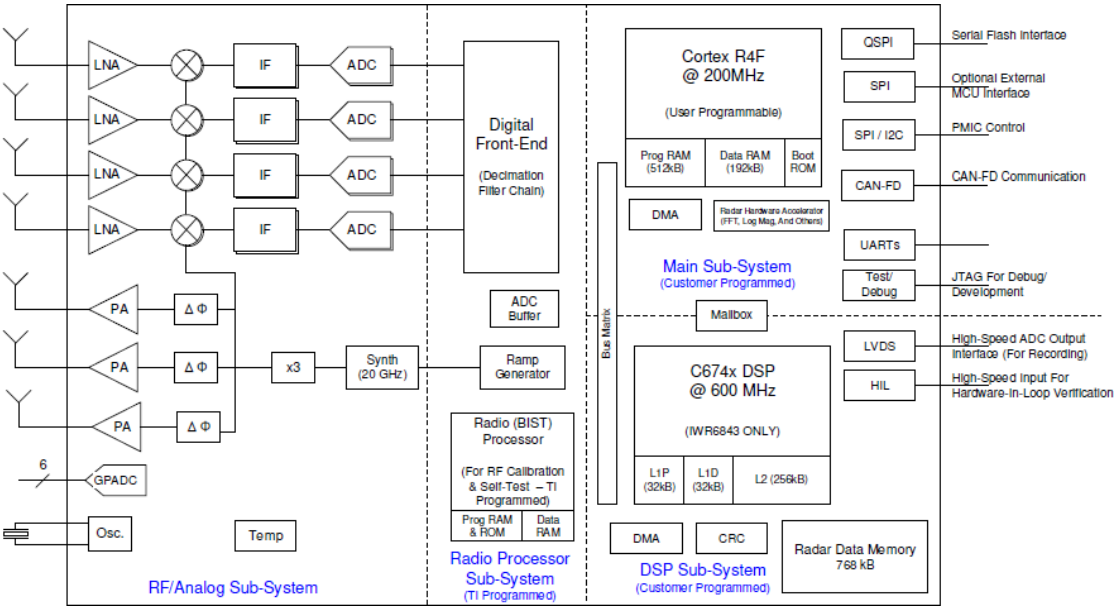

Figure 5.12: Functional block diagram of IWR6843ISK sensor, where the *Radio frequency and analogue sub-system*, *Radio processor sub-system*, *Main sub-system*, *digital signal processing (DSP) sub system* can be seen [63]

log-magnitude computations to obtain all the radar information from the measurements [63].

IWR6843ISK utilized firmware, called 3D People counting demo [106], which can be schematized like in Figure 5.13.

From the sensor point of view, the firmware can be divided into two layers, Detection layer [107], and Tracking layer [109], with the first one being implemented in the hardware accelerator and the second one being handled by the processor. The focus of the detection layer is to generate the point cloud, which is the collection of points, with each one having spherical coordinates, radial velocity, and SNR, where every single point represents a detected reflection. This point cloud is then fed to the Tracking layer which will be responsible for the association of a point cluster to a target (a person) when the characteristics of such cluster meets the requirements. Every target will then be tracked in time, obtaining the output of the Tracking layer which consists of a target list, where each one has Cartesian coordinates and linear speed. The outputs of the two layer will then be send to the host computer via UART.

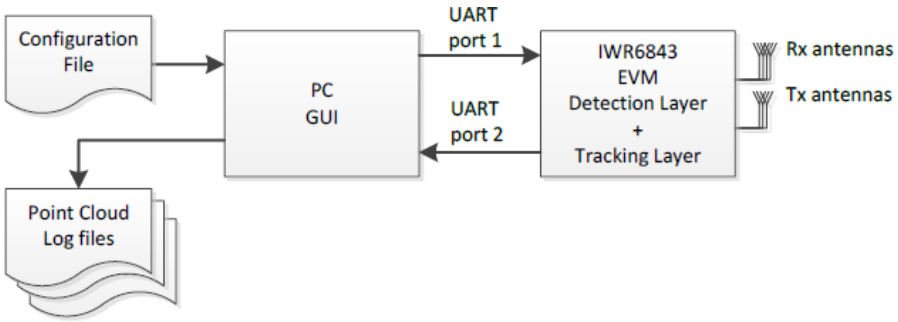

Figure 5.13: 3D people counting demo firmware setup, showing all the communications between host computer (using the graphical user interface (GUI)) and the sensor. Also, the two principal layers of the firmware, namely the *Detection layer* and the *Tracking layer* can be seen [106]

5.3.1 Detection Layer

Consisting of low level signal processing, this layer comprises two separate signal processing chains, one optimized for the wall mount of the sensor and the other for the ceiling mount. The processing chain is the following [107]:

- **Range processing** done for each antenna, detects the range of the objects following the basic radar working principle. Then, a window filter to the IF signal and the FFT transform is applied are applied in order to obtain the range spectrum.
- **Static clutter removal**, step which consists in the removal of all the static objects in the scene, like chairs or tables, letting the software focus only on the moving objects that are considered humans.
- **Capon Beamforming**, which output of this step will be a 2D range-azimuth spectrum matrix (heatmap) for the wall mount and a 3D range-azimuth-elevation heatmap for the ceil mount.

  More specifically, the heatmap is created by estimating the AoA of the detected objects, in terms of only azimuth or azimuth and elevation. Figure 5.14 illustrates the system geometry, having the azimuth (φ) defined as the angle between the y-axis and the orthogonal projection of the position vector on the xy-plane, while the elevation (θ)) is the angle between the projection onto the xy-plane and the vector position.
- **Constant false alarm rate (CFAR) detection algorithm**, applied to the 2D heatmap (3D for the ceiling mount). This step has the objective to define the power threshold needed to classify the returning radar wave as reflected

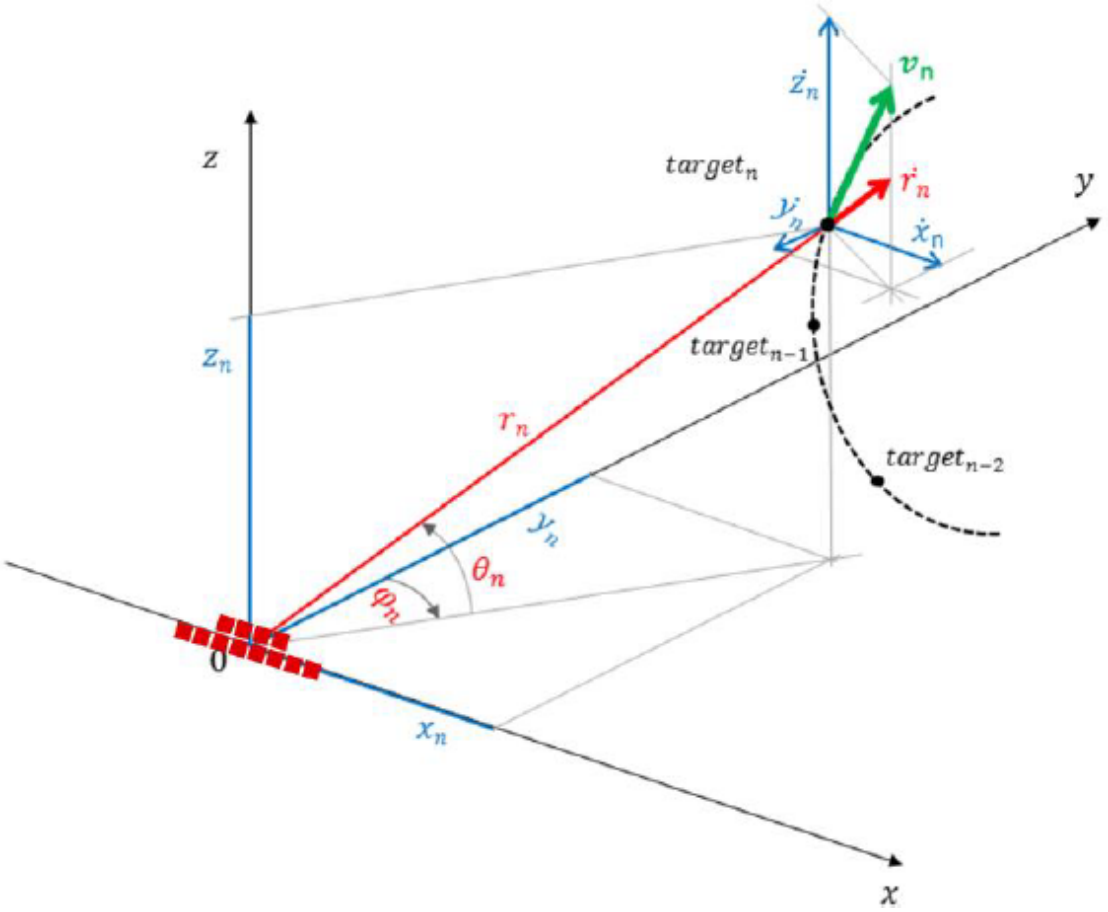

Figure 5.14: IWR6843ISK point cloud 3D coordinate system, with the sensor being at the origin of the axes and a target standing in front of the sensor [108]

by an object or not. The received waves, in fact, will present different levels of power depending by many factors, like for instance the environment, or the path that they travelled. The threshold value is very important in the operation, it can not be too high, because that would cause many tracks to not being classified as targets even if there would be a lot less of false alarms, which are interference or noise classified as objects; conversely, it can not be too low, because more tracks would be classified as targets, but there would be too many false alarms. In order to solve the threshold problem, the sensor uses a CFAR-Cell averaging small of (CASO), which sets as a threshold the smallest average of the left and right reference windows.

For the CFAR step, a 2-pass CFAR-CASO is used, the first pass works on the range domain, while the second pass confirms the detected objects in the azimuth domain for the wall mount. In the ceiling mount, the operation is

similar, with the only difference that the azimuth-elevation angles are put together in one dimension, using (5.1):

$$(azimuth\ \varphi, elevation\ \theta) \rightarrow (\varphi + \theta \cdot \varphi) \tag{5.1}$$

- **Elevation estimation (for the wall mount)**, a step in which the Capon Beamformer is applied again to the result of the CFAR algorithm in order to depict the elevation angle from the heatmap. This step is only performed in the wall mount configuration.
- **Fine Azimuth/Elevation estimation (for ceiling mount)**, after the CFAR step the Capon Beamformer algorithms are applied to generate a zoomed-in 2D azimuth-elevation angle spectrums for fine angle estimation. This step is only performed in the ceiling mount configuration.
- **Radial velocity estimation**, the last step of the detection layer, in which the Doppler spectrum is estimated over the consecutive chirps by applying to the virtual antenna array a capon beamformer which points to the azimuth-elevation angle.

  The virtual antenna array is a way to generalize a MIMO radar. For every transmitter, in fact, all four receiver antennas will receive the reflected signal shifted in phase. Since in the IWR6843ISK three transmit antennas are present, this concept can be generalized considering a virtual antenna array of one transmitter and 12 receivers (the number of receivers of the virtual antenna is given by the relation $N_{TX} \cdot N_{RX}$.

5.3.2 Tracking Layer

This layer is responsible for the localization and tracking of the targets, which are nothing more than clusters of points of the point cloud coming from the Detection layer. The Tracking layer [108] [109], which can be also referred to as Group tracker module, can be summarized in a series of basic building blocks, represented in 5.15.

- **Point cloud tagging**: step which consists of the selection of points to process. In the configuration file sent to the sensor and also via GUI, it is possible to determine the boundaries to consider while detecting targets. All the points of the point cloud outside these user-chosen boundaries are not considered in the next steps [109].
- **Predict**: implementation of the standard prediction equations of the Kalman filter. This step, which requires in input the state vector formed by position, velocity, and acceleration of the tagged tracked targets and their respective

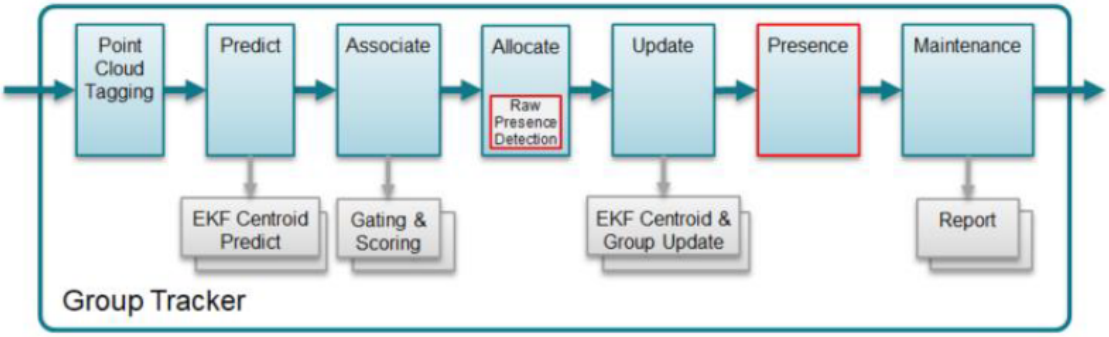

Figure 5.15: Block diagram of Tracker layer (Group Tracker) showing the principal operations performed sequentially by the layer. The operations work with the point cloud in input in order to produce the target list in output [108]

state covariance matrix, where the latter is the result of the Capon beamforming step of the detection layer needed to estimate the range-azimuth heatmap (or range-azimuth-elevation heatmap). Once solved the prediction equations, the output of this step will be the new state vector of the tracked targets as well as the new covariance matrix [109].

- **Associate**, step where each track will have a gate created around itself, then, for each point, the Mahalanobis distance between point and track is computed. If the latter falls within the gate of a track, a bidding score is assigned to the point. Finally, the point will be associated to the track (each point can be associated with only one track) which has the highest bidding score [109].

- **Allocate**, step conceptually very similar to the clustering technique. All the points of the point cloud that are not associated with one of the existing tracks can be chosen for initializing a new cluster/candidate set, which can become a new track. Firstly, the measurements points need to pass the configurable velocity and range thresholds in order to be added to a cluster, then, the centroid of such cluster will be re-calculated. Once all points have been evaluated, the new clusters are evaluated in terms of minimum number of points threshold, mean velocity of the points threshold and required combined SNR of all points in the cluster. If all the thresholds/requirements are satisfied, the cluster will become a new track, otherwise, such cluster with all the relative measurement points will be ignored [109].

- **Update**: step which foresees the update of the track centroid and the covariance matrix for such track when new points are assigned to the latter in the previous steps. Also, in this step the group track dispersion matrix and the

group covariance matrix, where the latter is used to create the gate around each track, are computed [109].

- **Presence**: check of the presence boundary box, which like the boundary box of the Point cloud tagging step can be modified in the configuration file or in the GUI. The focus of the check is to see if the targets exist in the presence boundary box. In addition, the clusters obtained in the allocate step are checked again and, if the number of points forming the cluster and the mean velocity exceed the set thresholds, the cluster will be considered valid [109].
- **Maintenance**: last step, which focuses on the track states [109]. A target/track in fact, can be in the DETECT, ACTIVE or FREE state. In this step the states can be changed or de-allocated. A track may change state if the thresholds set in the state transition parameters are met. A track that is currently allocated will start with the DETECT state. Every time instant, the track can get a HIT or a MISS event, with the first being the presence of any non-zero point in the track instance and the latter the absence of points in the tracking instance. After a configurable number of HIT events, the track can transition from DETECT to ACTIVE state and after a configurable number of MISS events, the track can pass from the DETECT to the FREE state. Actually, in the ACTIVE state, the track can be in *Normal, Static, Exit, or Sleep* conditions:
  - *Normal condition*: No special condition occurring in the target/track
  - *Static condition*: The target is in the "static zone". A target is static if its velocity is close to static (depending on the threshold for a velocity to be static).
  - *Exit condition*: If the target is not in the "static zone" but its number of MISS events exceeds the set threshold this means that the target is exiting the boundaries.
  - *Sleep condition*: A target is declared in this condition if it stays static for long enough. By putting a target in this state in fact, we can extend the maximum lifespan of such target in the static zone, allowing the sensor to continuously track even the steadiest target.

  In Figure 5.16 the states transitions diagram with the aforementioned thresholds.

5.4 mmWAVE Visualizer

The software utilized in order to visualize in real-time all the tracks detected by the IWR6843ISK is the mmWave People Counting software, Figure 5.17. This open-source GUI, written in Python, allows the users to select the desired configuration

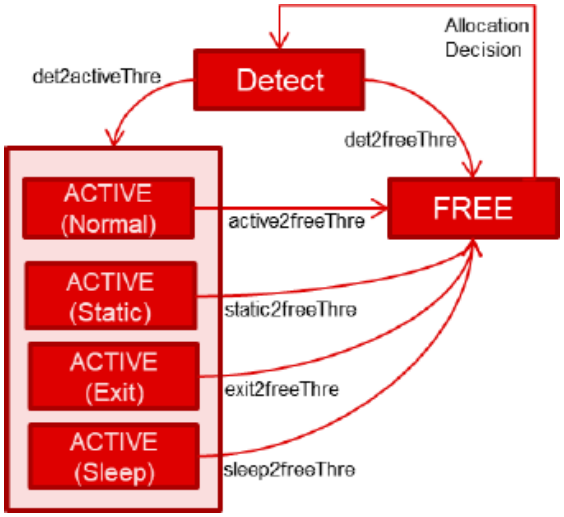

Figure 5.16: Tracker layer states transitions diagram, showing all the states that a track can have, as well as the state transitions [108]

file, which includes all the parameters needed for the detection and the tracking layers. Once the sensor is connected, by means of the selection of the two communication port (COM)s ports, and the configuration file has been selected, all the sensor parameters, e.g., maximum range, range resolution, maximum velocity, and velocity resolution, will be displayed in the GUI, as well as the detection boundaries in which the sensor searches for targets. While the detection layer parameters can not be modified in the GUI, the detection boundaries, the orientation, and the position of the sensor, can be configured in real-time.

Finally, directly by modifying the code of the .py files that creates the GUI, it is possible to produce an output .bin or .csv file containing all the data coming from the detection and tracking layers, e.g., the point cloud spherical coordinates and the tracks Cartesian coordinates, together with their respective velocities.

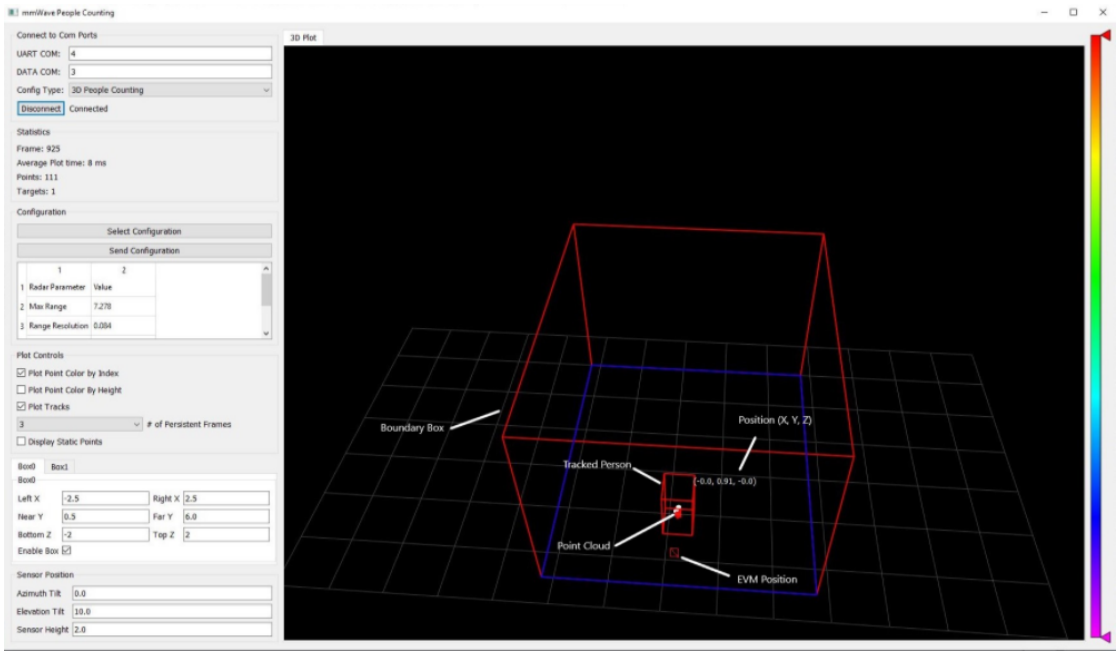

Figure 5.17: IWR6843ISK people counting graphical user interface (GUI) software, where on the left side there are all the configuration parameters, the configurable detection boundaries and the sensor physical set-up (azimuth, elevation and height) are shown, while on the right side the 3D live map of the detected area is shown [110]

Chapter 6

Sensor measurements

This chapter focuses on the measurements that have been performed using the two development kits chosen, the Position2Go and the IWR6843ISK. The principal objectives of the measurements are:

1. Analyze the sensors capability to detect a person inside their line of sight, studying their tracking capabilities.

2. Analyze the consistency of the results, focusing on the differences between the repeated measurements that consider the same target with the same conditions, e.g., same position, same configuration, but in different time instants.

3. Analyze the dynamic data the detected target in the measurements, such as velocity or acceleration.

4. Analyze the precision of the measurements in terms of differences between measured trajectory and real trajectory

5. Optimize the measurements in post-processing in order to reduce the distance between measured trajectory and real trajectory

6. Compare the obtained measurements from the two sensors

Perform all the analyses considering different sensors configurations, in order to understand which one is the best in that particular environment.

6.1 Environments

All the experiments have been performed in three different environments, consisting of two indoor environments, Figure 6.1, where the difference between the two is

the number of "clutter" present, represented by furniture of particular materials (wood, metal, plastic), and one outdoor environment shown in Figure 6.2.

The first environment is a common electronics laboratory, referred to as *Lab*, where the measurement area is empty but surrounded by furniture like tables, chairs or tool cabinets. The goal of the measurements in this environment is to understand if the sensors are able to localize and track a human target in a small indoor environment full of "clutter".

The second environment, referred to as *Corridor* consists of an empty large area located in the corridor of the university building. The goal of the measurements in this environment is to understand if the sensors are able to localize and track a human target in a large indoor environment, where the sensors are placed at a higher distance with respect to the walked path, in contrast to the *Lab* environment.

Finally, the third environment, referred to as *Terrace*, is an empty terrace located at the top of the university building, where the only walls are railings and a metal structure is present near the left-most part of the trajectory. The goal of the measurements in this environment is to understand if the sensors behave differently in an outdoor environment.

6.2 Sensors Configurations

In both sensors, for every single environment, several configurations have been tested, in order to compare them to find which one is the best suited for that particular area, more specifically, for the Position2Go sensor the tested configurations are shown in Table 6.1.

For every configuration, the minimum and maximum range were configurable in an independent way, this means that all the detected targets that are below the minimum distance or beyond the maximum distance are excluded by the radar algorithm.

In addition, the PGA power level depends on the environment: setting the level to 4 in the indoor measurements would result in very disturbed measurements, while setting it to three in outdoor environments would result in a very difficult acquisition of the target, obtaining empty measurements.

The *Samples per chirp*, which can assume values [32, 64, 128, 256], and the *Chirp per frame*, which can assume values in the range 1–64 are the same for every configuration, this is because the parameters are set to their default values that are, indeed, the best ones. Setting the parameters to different values would have resulted in worst performances. The *Chirp duration*, which can assume values in the range 50 µs to 3,000 µs is the parameter that changes in every configuration, varying from a minimum value of 120 µs to a maximum value of 250 µs. Since the *Samples per chirp* is set to 64, the *Chirp duration* value can not be lower than

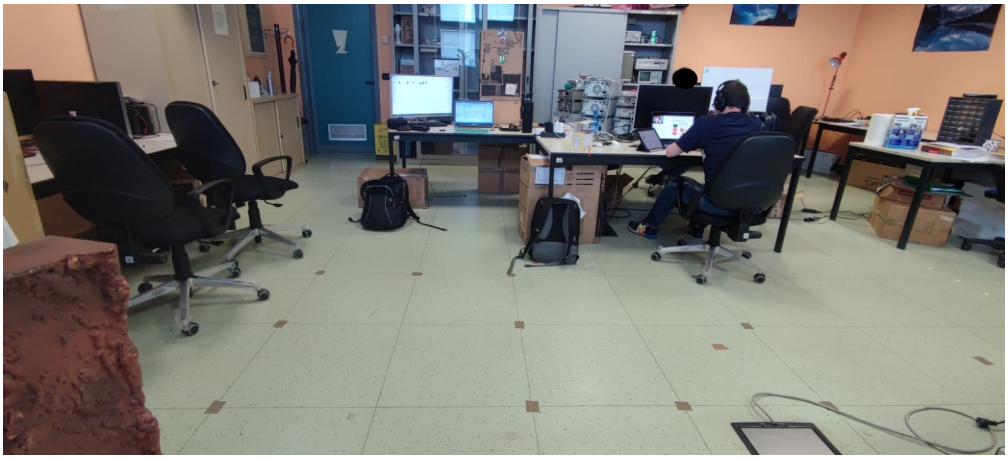

(a) Lab environment (indoor) where the sensors can be seen in the top part, while in the bottom part the area where the target walked can be seen. This environment is full of "clutter" represented by furniture all around the experiment area

(b) Corridor environment (indoor) where the sensors can be seen in the top part, while in the bottom part the area where the target walked can be seen. This environment is empty and no "clutter" is present. The walls are made of the same material of the laboratory walls

Figure 6.1: Indoor measurement environments

100 µs, because, otherwise, a supported sampling rate would not be ensured [99]. In addition, values higher than 250 µs would always result in worse performances in terms of target localization. Finally, the *Pulse repetition* time is a non-configurable value, which will always be equal to the *Chirp time* plus 200 µs.

The tested configuration for the Texas Instruments sensor is shown in Table 6.2.

In all the configurations, there are two different maximum range parameters: the *Maximum range*, that is the maximum distance at which the sensor can possibly

Figure 6.2: Terrace environment (outdoor) where the sensors can be seen in the top part, while in the bottom part the area where the target walked can be seen. Differently from the indoor environments, no walls are present except for the metal structure on the left and the railings on the right. Like in the Corridor environment, no "clutter", represented by furniture, is present

detect targets, while the *Maximum boundary range* is similar to the maximum range of the Position2Go sensor: setting this parameter will make the firmware algorithms ignore the detected targets at a range beyond this boundary. For every configuration, this parameter is set to 4 m.

The objective of the different Configurations was to obtain different *Range resolution*s besides the one obtained with the standard configuration, e.g., Configuration 2. Besides increasing the bandwidth, modifying the starting frequency from 60.75 GHz to 60 GHz in all the configurations and delaying the *Ramp end* time, modifying this value from the standard 59.10 µs to 72.73 µs, the resolution change has been obtained by modifying the number of *ADC samples* and *Chirp per frame*, in particular, the decrement of the first together with the increment of the second parameter will cause an increment in the range resolution of the sensor.

Table 6.1: Position2Go configurations

Conf.	Samples per chirp	Chirps per frame	Chirp duration (µs)	Pulse repetition (µs)	Min range (cm)	Max range (cm)	Acq. period (ms)	PGA level
1	64	16	150	350	90	600	150	3 in, 4 out
2	64	16	120	320	90	600	150	3 in, 4 out
3	64	16	200	400	90	600	150	3 in, 4 out
4	64	16	250	450	90	600	150	3 in, 4 out

All the aforementioned parameters have been obtained using the tool mmWave sensing estimator [111], which provided a starting point for the tuning step that has been then performed following the indications in [107].

As aforementioned, the configurations for both sensors have been created using the tools given by the producers of the latters. The objective of the configurations is to understand if the change of the configurable parameters have an impact on the performance of the two sensors, and if this impact changes with the change of the environment. As a matter of fact, the obtained configurations are not the best possible ones for the sensors, since no fine tuning have been performed on the configurations in order to obtain the best performance.

6.3 Method

The followed method is always the same: the same specific trajectory has been set, consisting of movements performed in straight segments of always the same distance, 1.2 m. The sensors have been positioned in the exact center with respect to the trajectory (at different heights), at a specific distance which guarantees that all the walked trajectory is inside the field-of-view (FoV) of the two sensors. The minimum distance between the two sensors and a straight line of trajectory, given that the sensors are always in the middle line of trajectory, must be of 1.8 m.

To get a reference for the position, a 2D reference system has been set as shown in Figure 6.3.

All the measurements start at the Start point and consist of several movements going from the Start point to the End point and vice versa. As stated before, the sensors are always positioned at $x = 1.8\,\text{m}$ and $y > 3.6\,\text{m}$.

In order to analyze the results of the measurements two MATLAB scripts have been created, which take as input the target data of the two sensors and produce in output the metrics needed to evaluate the sensors performances. An overview of the structure of such scripts can be seen in Figure 6.4.

More specifically the steps followed by the scripts are:

Table 6.2: IWR6843ISK configurations

Conf.	Start freq. (GHz)	Idle time (µs)	ADC start (µs)	Ramp end (µs)	Freq. slope (MHz/µs)	ADC samples	Chirps per frame	Frame period (ms)	Max range (m)	Range resolution (m)
1	60.00	30	25	72.73	54.71	120	16	55	7.279	0.067
2	60.75	30	25	59.10	54.71	96	48	55	7.279	0.084
3	60.00	30	25	72.73	54.71	50	64	55	7.279	0.161
4	60.00	30	25	72.73	54.71	35	76	55	7.279	0.231

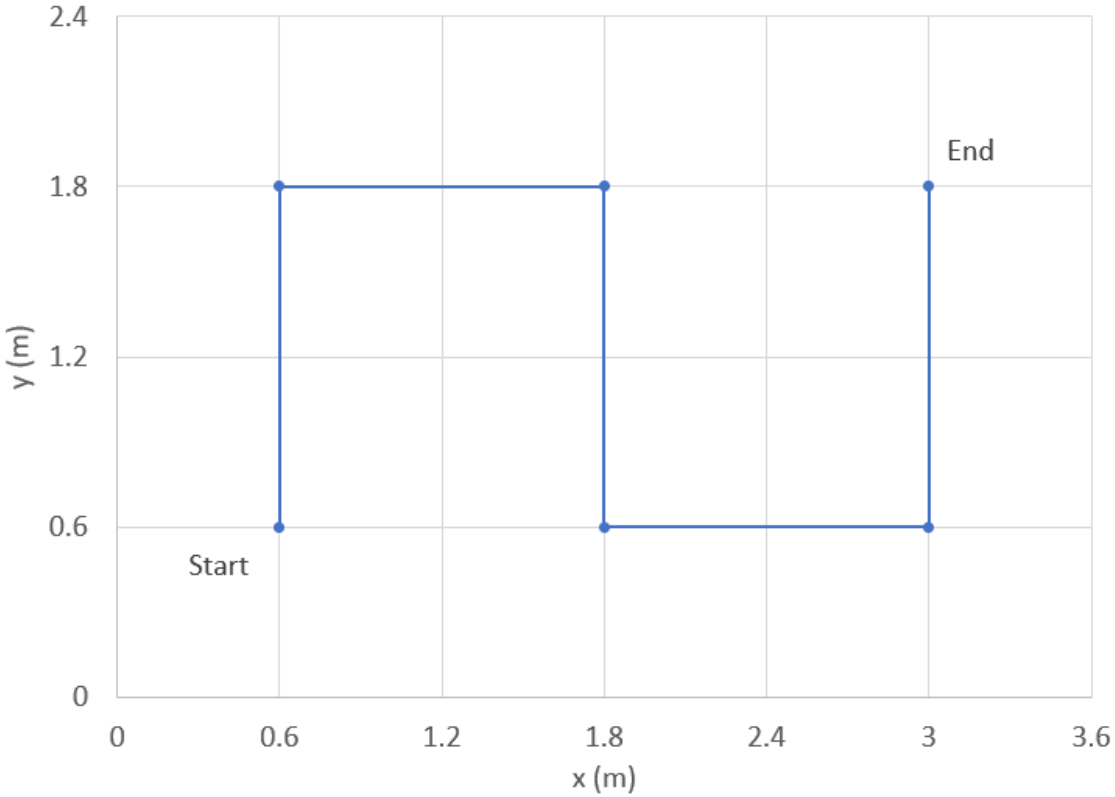

Figure 6.3: Real trajectory walked by the target in every environment for every configuration. The experiments always start at the *Start* point and, once arrived at the *End* point, the whole path is repeated again the other way round, e.g., from *End* to *Start* point. The process is repeated many times for every measurement

- **Load sensor data**: the first step of the script, the sensor output file consists in a comma-separated value (CSV) for the IWR6843ISK, consisting of all the point cloud and target measurements data (only the target data have been considered) for every time instant, and a .trg file for the Position2Go, consisting of all the target measurement data.
- **Convert coordinates**: conversion of the coordinates of the target data for either sensor. The IWR6843ISK reports the coordinates in cartesian form, so the only operation to do is to change the reference system, the Position2Go, on the other hand, reports the coordinates in spherical form, so first a spherical to cartesian coordinates conversion must be performed, then, those coordinates can be changed of reference system.
- **Plot full trajectory**: plot of the trajectory data obtained after the conversion. This step is needed in order to determine the cutting coordinate points.

- **Cut the trajectory in segments**: after the cutting points (which depend on the measurements) have been determined, the measured trajectory is divided in several segments, which start from the minimum boundary and end in the maximum boundary.

  The result of this operation is the creation of five cell arrays, given the fact that the real trajectory contains five straight segments, three vertical and two horizontal.

- **Linear regression of segments**: for every single segment, the coefficients of a linear first-degree equation are estimated using the x and y coordinates. Such equation will be used to estimate the y coordinate using the x one in order to determine the straight line that fits best every single trajectory segment. Moreover, in this step, the estimation error is given by the MATLAB estimation function, which is used as an evaluation metric. Once all the straight segments are estimated, an average of all the estimation errors of the straight segments associated with a real trajectory segment will be computed, obtaining five mean regression errors, each one for a real trajectory segment.

  Since the obtained straight segments may show different lengths, they are finally cut or stretched using the same equation needed to estimate them. The minimum and maximum coordinate (y for vertical segments and x for horizontal segments) will be equal to the cutting points of every trajectory part.

- **Area computation**: in this step the area between all the possible combinations of straight segments of the same trajectory part is computed. If two straight segments intersect themselves, the area will be the sum of the areas of the two triangles described by such segments, otherwise, the area will be the difference between the area of two trapezoids formed by each segment and a straight imaginary segment at a distance of 50 m or more. Once the areas of all the combinations of the straight segments associated with the same real trajectory segment are computed, the average of such areas is computed. The result will be five area values, each one associated with a real trajectory segment, normalized by dividing by each straight segment distance. Lastly, the square root of the area error values are computed, in order to obtain a better comparison between this error and the other errors (except for the Acceleration error) which all are expressed in meters.

- **Acceleration computation**: in this step the average acceleration of every measured trajectory segment is computed, performing the double derivative of the positions comprised in the considered segment over the *Frame periodicity* time interval squared for the IWR6843ISK case, or the *Acquisition frame* period squared for the Position2Go case, since in both cases the position estimation

is performed at the end of every transmitted frame. It is important to notice a moving average has been applied to the positions before the double derivative operation, in order to improve the results reducing the noise. This moving average has a window size comparable with the time instants considered, of about seven samples.

- **Relative location error computation**: step in which the relative location error is computed. First, the minimum distance between the real trajectory segment and respective measured segments is computed, with the following rules:
  - *Vertical segments*: when the vertical segments of the trajectory are considered, the minimum distances in the x-axis only are computed, by creating for every measured trajectory segment an imaginary real trajectory segment with the x-coordinates of the real path (e.g., for the first vertical segment, $x = 0.6\,\text{m}$, and the y-coordinate of the considered measured segment. In such a way, the y-coordinates will always be aligned, and the distance will only be in the x axes.
  - *Horizontal segments*: when the horizontal segments of the trajectory are considered, the minimum distances in the y-axis only are computed, by creating for every measured trajectory segment an imaginary real trajectory segment with the y-coordinates of the real path (e.g., for the first horizontal segment, $y = 1.8\,\text{m}$, and the x-coordinate of the considered measured segment. In such a way, the x-coordinates will always be aligned, and the distance will only be in the y axes.

  Then, the root of the sum of the squares of such minimum distance is computed, for instance, if the first real trajectory segment of the path has three measured trajectory segments associated, the root of the sum of squares is (6.1).

$$distError = \sqrt{(minDistance_1)^2 + (minDistance_2)^2 + (minDistance_3)^2} \quad (6.1)$$

  The result of the operation of (6.1) will be five *distError*s, each one associated with a real trajectory segment. Finally, the relative location error is given by the root of the sum of squares of those five *distError*s (6.2).

$$\begin{aligned} locError = [(distError_1)^2 + (distError_2)^2 + (distError_3)^2 \\ +(distError_4)^2 + (distError_5)^2]^{\frac{1}{2}} \end{aligned} \quad (6.2)$$

- **Path optimization**: in this step, the translation values for the measured path are computed. The path will be translated in the x axis of a value of

(6.3) and in the y axis of a value of (6.4), in order to try to minimize the relative location error. The direction of such translations is decided by visual inspection of the measured trajectory and the real trajectory for every single measurement.

$$translation_x = mean(distError_1, distError_3, distError_5) \tag{6.3}$$

$$translation_y = mean(distError_2, distError_4) \tag{6.4}$$

This translation is not guaranteed to obtain a smaller relative location error than the original one. If this happens, the path will be translated of values chosen by visual inspection, following a trial-and-error method.

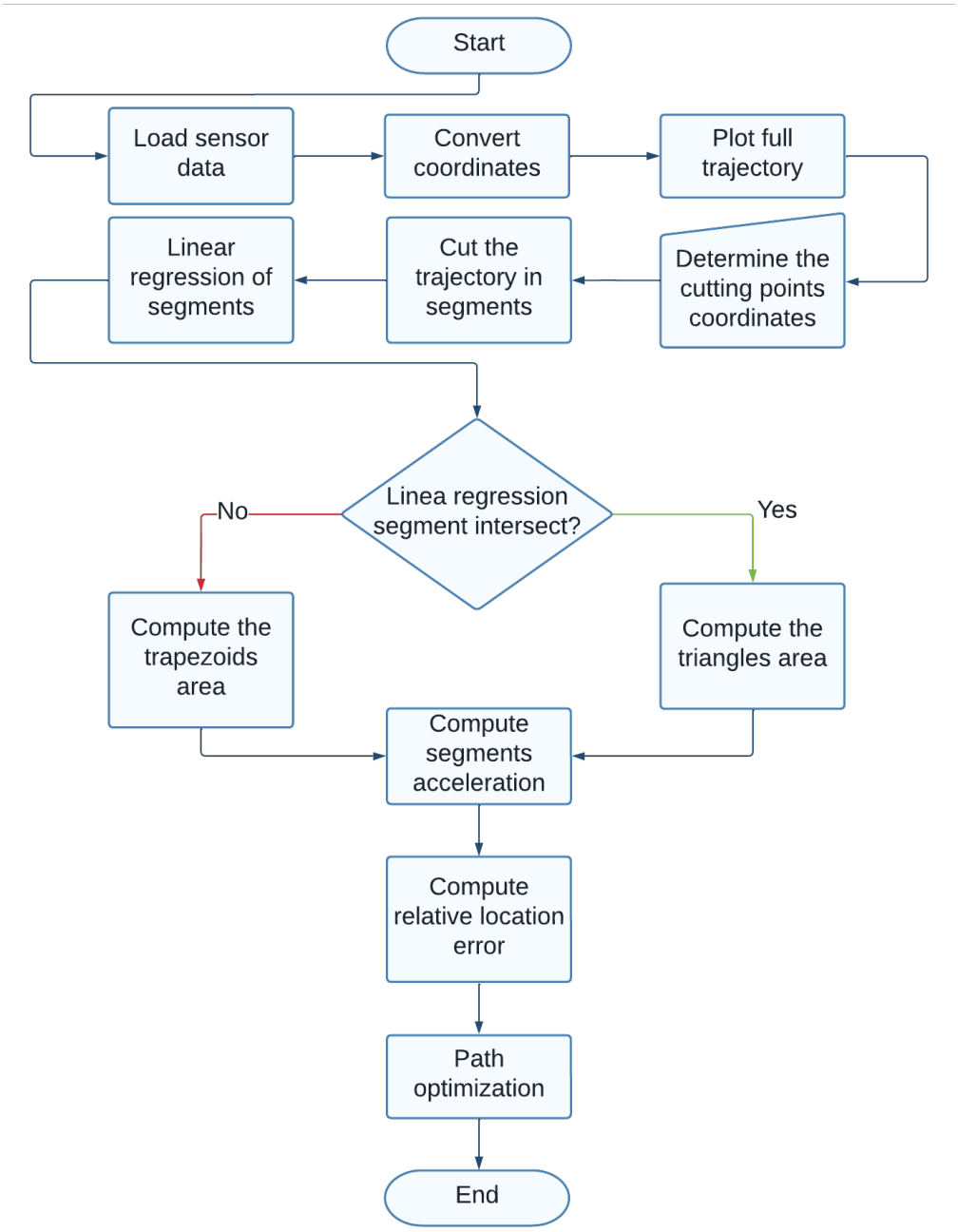

Figure 6.4: MATLAB post-processing script applied to all the measurements obtained in order to calculate the evaluation criteria chosen, *Regression error*, *Area error*, *Acceleration error*, *Relative location error*

Chapter 7

Experimental Results

This chapter reports all the measurement results obtained from the various experiments divided by environment and divided by configuration utilized, for a total of 12 different experiments per sensor (four experiments per environment per sensor). It is important to notice that in all the experiments the original firmwares provided by the producers of the sensors have been utilized. In all the experiments, the sensors were placed one on top of the other, in order to have them positioned on the same x and y coordinate of the reference system. This means that the Position2Go has $z = 1.30\,\text{m}$ and the IWR6843ISK has $z = 1.48\,\text{m}$.

The chapter is organized in three sub-sections: Position2Go measurements, divided by environments, IWR6843ISK measurements, divided by environments, the comparison of the results of the two boards. For every environment, first, the physical set-up for the experiments is shown, then, the measured trajectory vs. the real trajectory plots for every configuration are presented.

In the last section of the chapter, the graphs of all the selected evaluation criteria for the two boards are shown. The graphs, divided by type of criteria and having all the environment criteria in the same type of graph, report in the x-axis all the different configurations. Moreover, in the linear regression error, root area error, and acceleration, the mean value and the standard deviation of the errors are presented, since they have been computed divided for trajectory segments, e.g., for every configuration and for every environment, the evaluation of the measurements resulted in five linear regression errors, five root area errors and five acceleration, each one associated to one of the trajectory segment. To have better graph readability, the standard deviation of the linear regression error, root area error, and acceleration has been drawn using a semi-transparent area that surrounds the average error value, with the same color as the latter. The minimized location error is computed as the square root of the sum of squares of all the location errors of the measured trajectory segments, hence it does not have a standard deviation. Also, the tables with the evaluation criteria numerical values

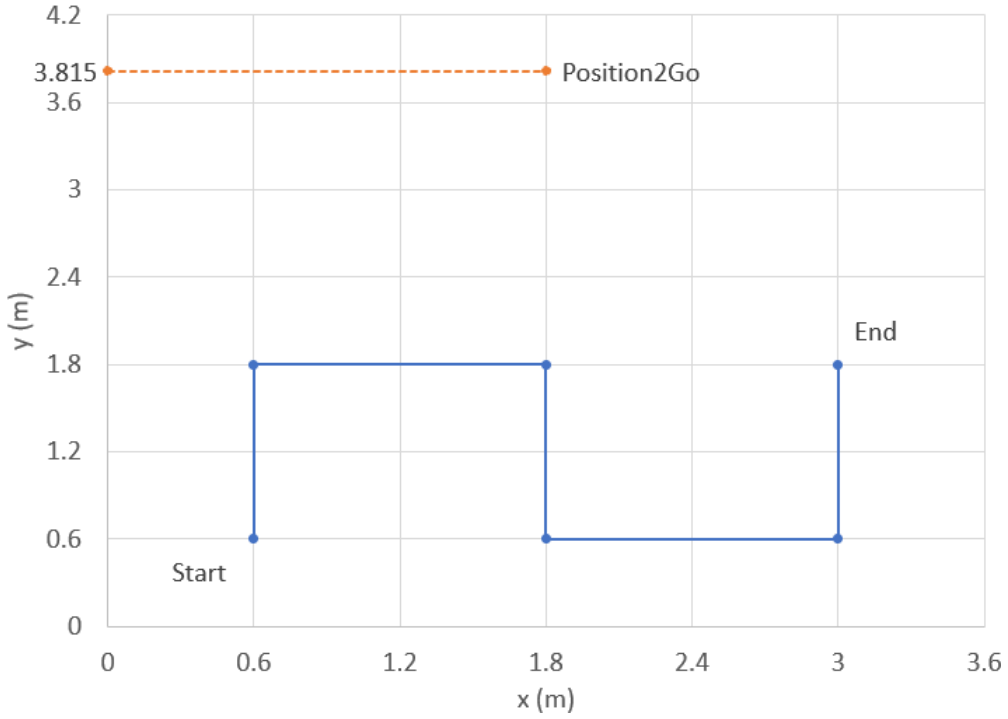

Figure 7.1: Position2Go set-up for Laboratory measurements. The orange dot represents the sensor position, while the blue path is the real trajectory

are reported.

7.1 Infineon Sensor Position2Go

The results of the measurements of the Position2Go board are presented in this sub-chapter. All the measured trajectory plots are the result of a moving mean window of size five applied to the measured positions, since the sensor tracking ability is not as good as the IWR6843ISK sensor. Without the moving mean, the plots were very chaotic, having the target "jumping" in a radius of about 20 cm of the actual position. In addition, the measured positions, except for the Garden measurements, have been filtered to remove spurious Reflections due to the wall in front of the sensor. The positions of the reflections had large negative y coordinates in the reference system in Figure 7.1 and Figure 7.2.

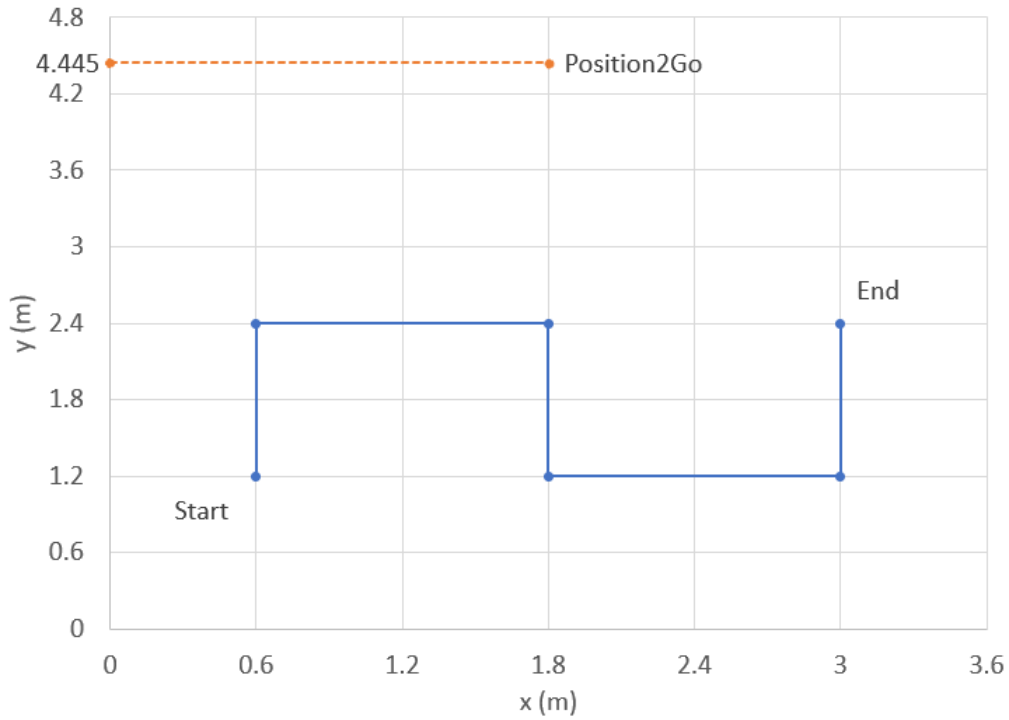

Figure 7.2: Position2Go set-up for Corridor measurements. The orange dot represents the sensor position, while the blue path is the real trajectory

7.1.1 Environment: Lab

The set-up utilized for this experiment is shown in Figure 7.1 and is the same for all the configurations.

The measurements in the Lab environment led to the results shown in Figure 7.3, where the measured trajectory for every configuration can be seen.

As can be seen in the measured trajectory plots, the sensor is able to track the target in almost all the utilized configurations, obtaining the best precision in the center and the right vertical segments, when the person is approaching or leaving the sensor. In the center segment trajectory lower curve, although, the sensor places the target at a higher distance than the real one. For what regards the horizontal segments, the best precision is obtained at the segment with y = 1.8 m.

7.1.2 Environment: Corridor

The original set-up for this set of experiments was the same as the one utilized for the Corridor experiments performed with IWR6843ISK, but the sensor has not been able to capture good data and the measurements have been repeated many

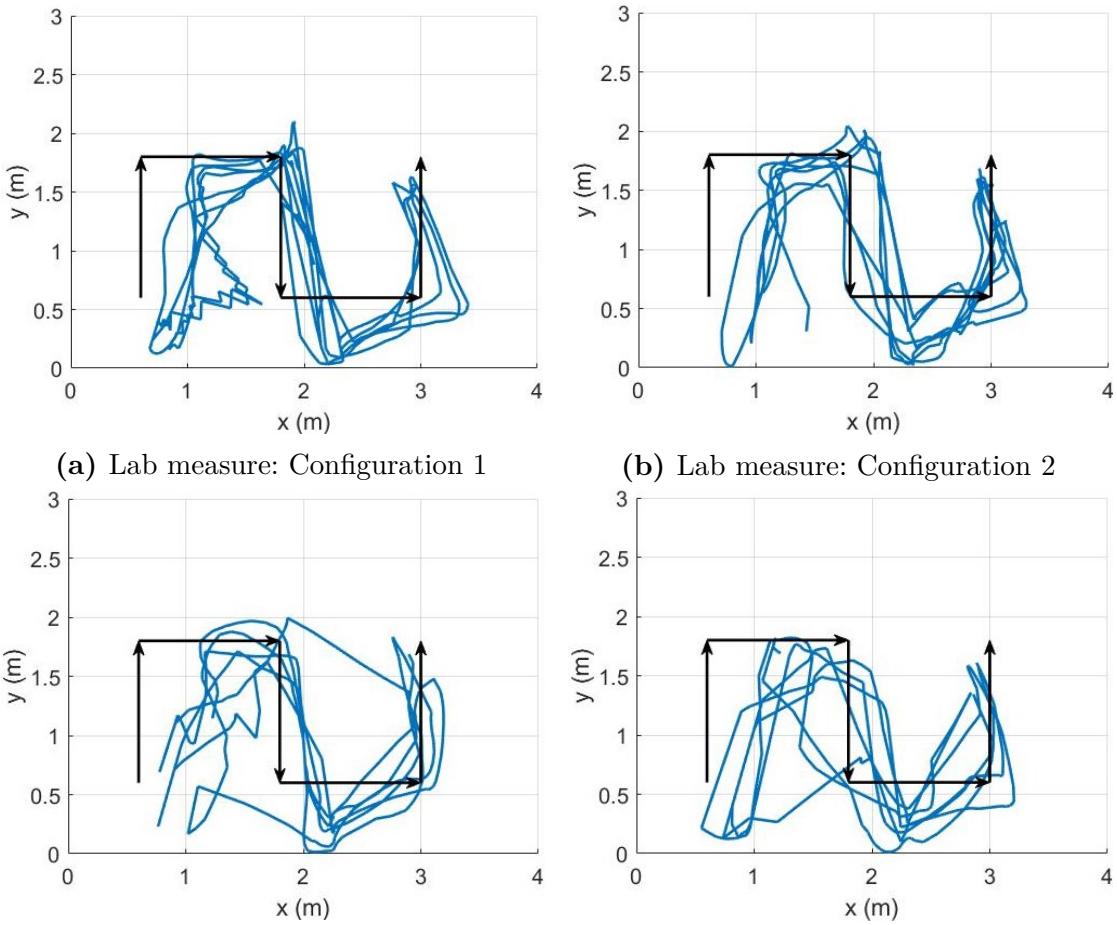

(a) Lab measure: Configuration 1

(b) Lab measure: Configuration 2

(c) Lab measure: Configuration 3

(d) Lab measure: Configuration 4

Figure 7.3: Position2Go Laboratory measured trajectories (in blue) vs. real trajectories (in black)

times. To solve this problem, the sensor and the walked path have been translated by 0.60 m along the y direction in order to obtain good measurements.

The set-up can be seen in Figure 7.2, while the measured trajectories can be seen in Figure 7.4.

This environment has been the most difficult one for the Position2Go measurements, since the measurements had to be repeated many times in order to obtain data not too corrupted by noise. In all configurations, the higher precision has been obtained in the central vertical trajectory segment, followed by the left vertical segment, with $x = 0.6$ m. The right-most horizontal segment, with $y = 0.6$ m is the worst one in terms of precision, having oblique segments, most noticeable in the Configuration 4 measurement, or segments with a totally wrong y coordinate,

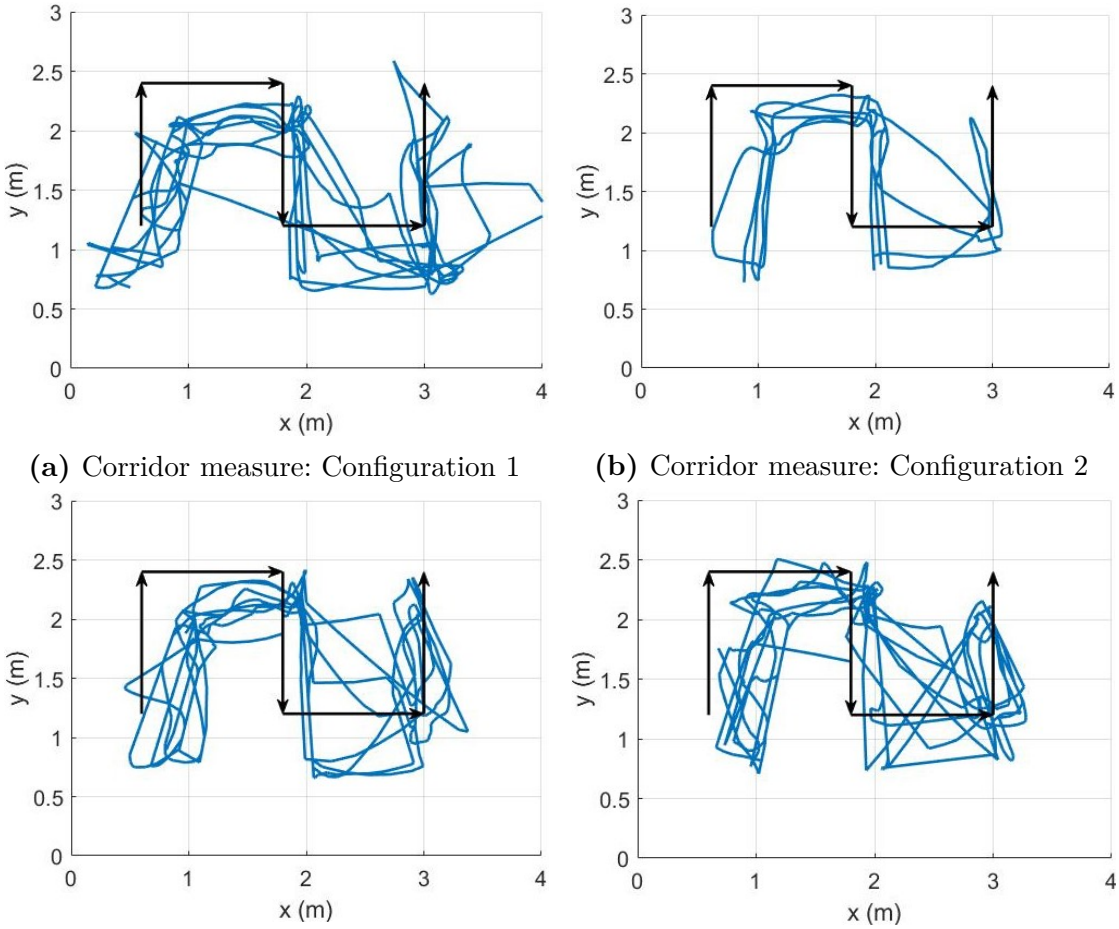

(a) Corridor measure: Configuration 1

(b) Corridor measure: Configuration 2

(c) Corridor measure: Configuration 3

(d) Corridor measure: Configuration 4

Figure 7.4: Position2Go Corridor measured trajectories (in blue) vs. real trajectories (in black)

most noticeable in the Configuration 3 measurement.

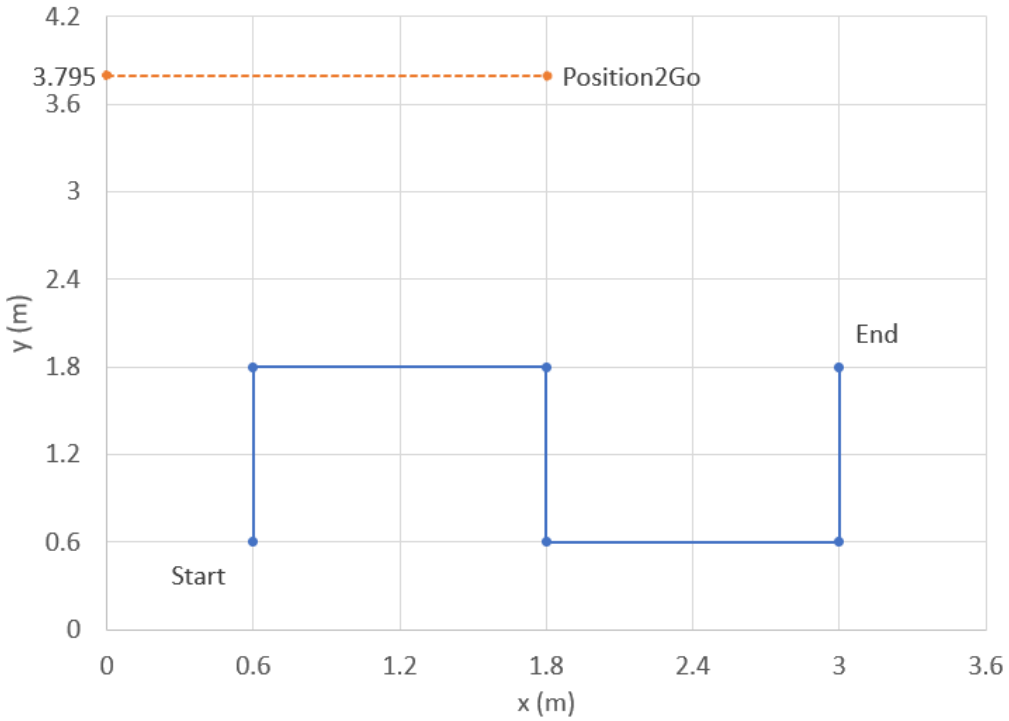

Figure 7.5: Position2Go set-up for Garden measurements. The orange dot represents the sensor position, while the blue path is the real trajectory

7.1.3 Environment: Garden

The set-up for these experiments can be seen in Figure 7.5, while all the measured trajectories can be seen in Figure 7.6.

Differently from the IWR6843ISK outdoor measures, these experiments have been performed on the University garden, since the experiments on the Terrace resulted highly disturbed and not usable for the work. This problem led to the need to perform the experiments in another outdoor environment, comparable with the Terrace environment utilized for the Texas Instruments evaluation board. Hence, the choice of the Garden environment, shown in Figure 7.7. The principal difference between environments is that the ground material is different, having concrete in the Terrace and garden soil in the Garden, and there are no building nearby the measurement area in the Garden environment, just the university building behind the sensor, and another building at the left of the sensor, at a high distance.

The measured vs. real trajectory plots for all the configurations can be seen in Figure 7.6.

The measurements in this environment are the most precise ones, obtaining the best results among all the environments in all the trajectory segments. Differently

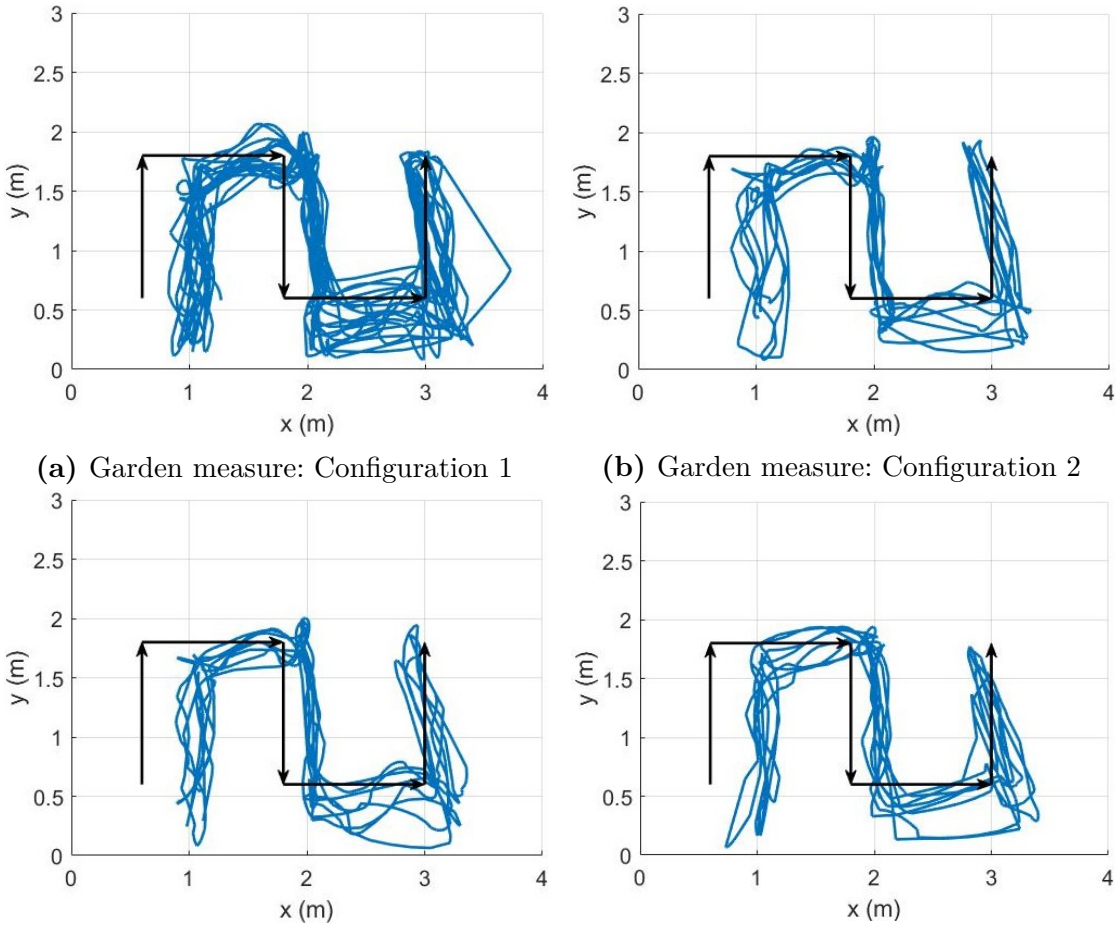

(a) Garden measure: Configuration 1

(b) Garden measure: Configuration 2

(c) Garden measure: Configuration 3

(d) Garden measure: Configuration 4

Figure 7.6: Position2Go Garden measured trajectories (in blue) vs. real trajectories (in black)

from the measurements in the other environments, in all Configurations the positions associated with the central vertical segment, even if describing straight lines, present a horizontal offset of about 20 cm in the positive x direction. In addition, the left-most vertical segment shows measurements with a very high offset of about 40 cm in the positive x direction. Finally, the right-most vertical segment shows the highest accuracy.

For what regards the horizontal segments, the one with y = 1.8 m is the most precise horizontal trajectory segment in all Configurations, while the one with y = 0.6 m shows positions of the target much more distant than the actual position, having points with y coordinate equal to 0.1 m or very near to 0 m, showing an offset of almost 0.6 cm in the worst case.

Figure 7.7: Garden environment (outdoor) where the Position2Go sensor can be seen in the top part, while in the bottom part the area where the target walked can be seen. No walls nearby the experiment area is present, only the university building behind the sensor, and another building at the left of the sensor at a high distance, differently from the Terrace environment, where the measurements resulted very disturbed and not exploitable for the thesis work. In addition, the ground material is not concrete but garden soil

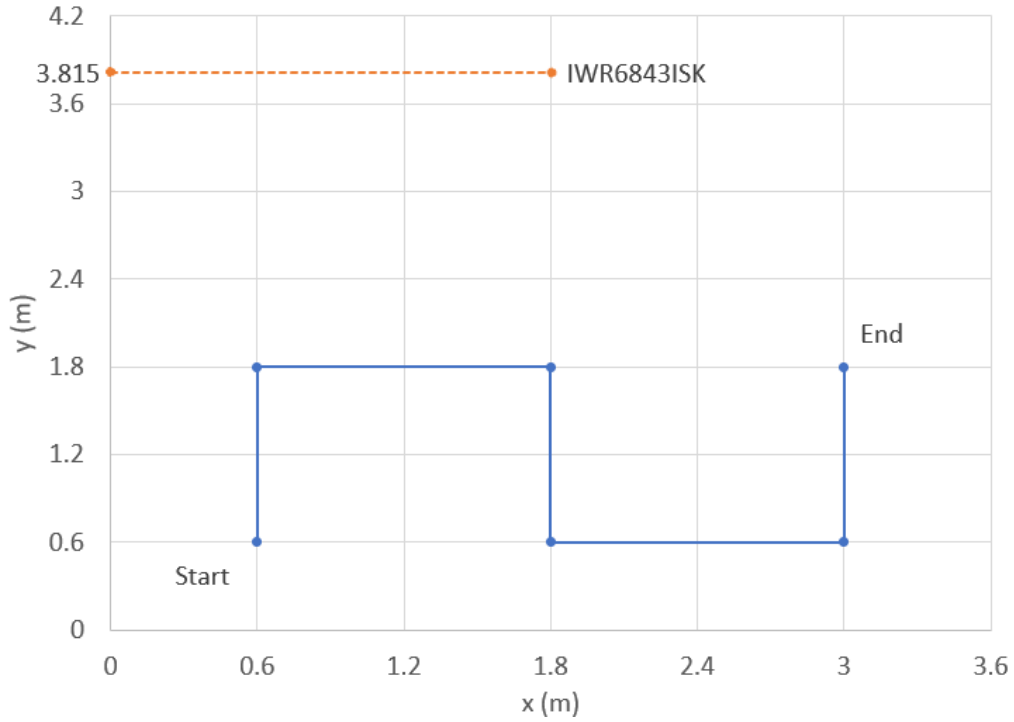

Figure 7.8: IWR6843ISK set-up for Laboratory measurements. The orange dot represents the sensor position, while the blue path is the real trajectory

7.2 Texas Instruments Sensor IWR6843ISK

The results the measurements of the IWR6843ISK board are presented in this sub-chapter. Differently from the PositionGO board, in the following results the moving mean has not been applied, since the measurements were much more stable than those of the Infineon PositionGo board. In addition, no filtering operation have been performed, since no reflection have been detected as "ghost" targets.

7.2.1 Environment: Lab

The set-up utilized in these experiments is shown in Figure 7.8, while the measured vs. real trajectories for all the configurations are visible in Figure 7.9.

The segment with the highest accuracy is the central vertical one, e.g., the segment right in front of the sensor. The other two vertical segments show a negative x direction offset, with the highest one present in the left-most vertical segment, especially in Configuration 1 and Configuration 2.

For what regards the horizontal segments, the most accurate one is the segment with y = 0.6 m coordinate, while the other one experience in all Configurations

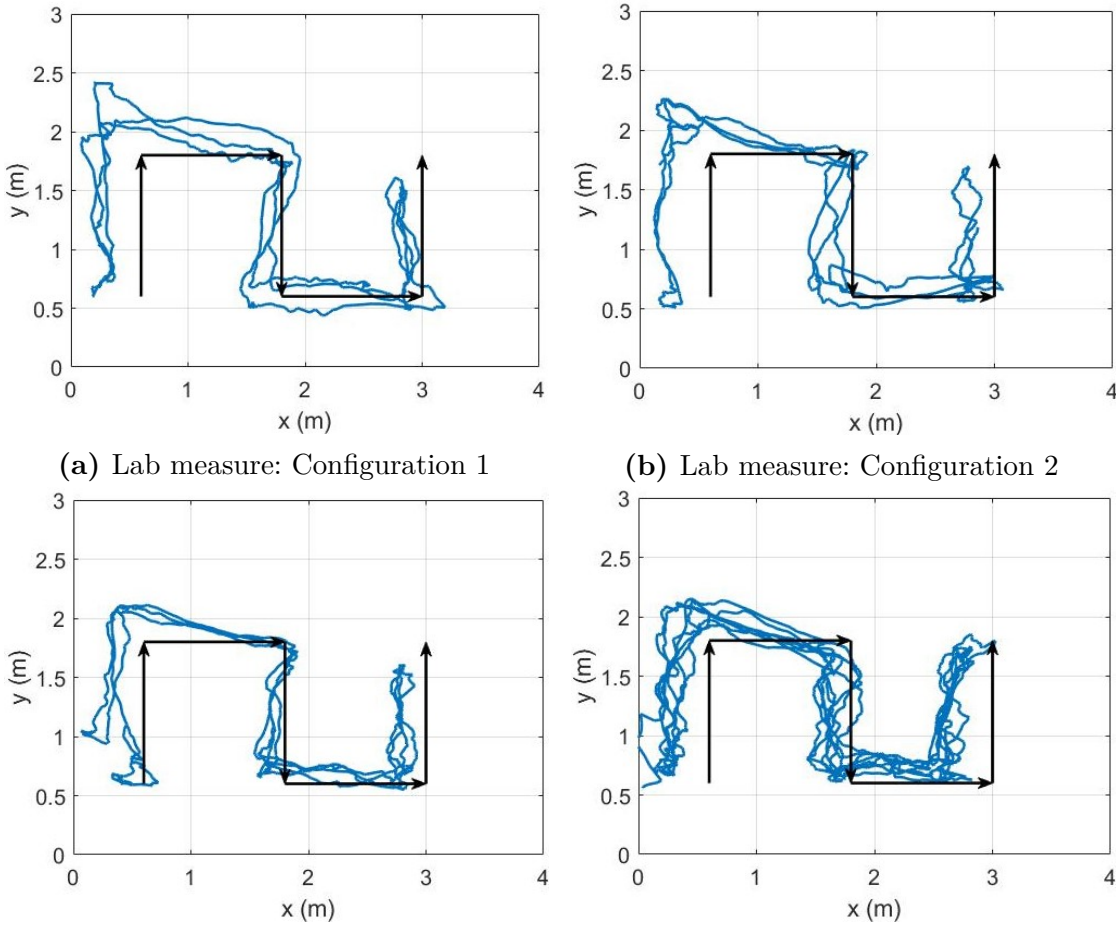

(a) Lab measure: Configuration 1

(b) Lab measure: Configuration 2

(c) Lab measure: Configuration 3

(d) Lab measure: Configuration 4

Figure 7.9: IWR6843ISK Laboratory measured trajectories (in blue) vs. real trajectories (in black)

a very high positive y offset nearby the curve that leads to the left-most vertical segment.

7.2.2 Environment: Corridor

The set-up utilized in these experiments is shown in Figure 7.10 while the measured vs. real trajectories for all the configurations are visible in Figure 7.11.

In this environment, all the vertical segments present a negative x direction offset, which is the lowest in the central segment and higher in the left-most segment. Differently from the Laboratory measurements, the horizontal measured segment at y = 1.8 m presents a lower positive y offset nearby the left-most vertical

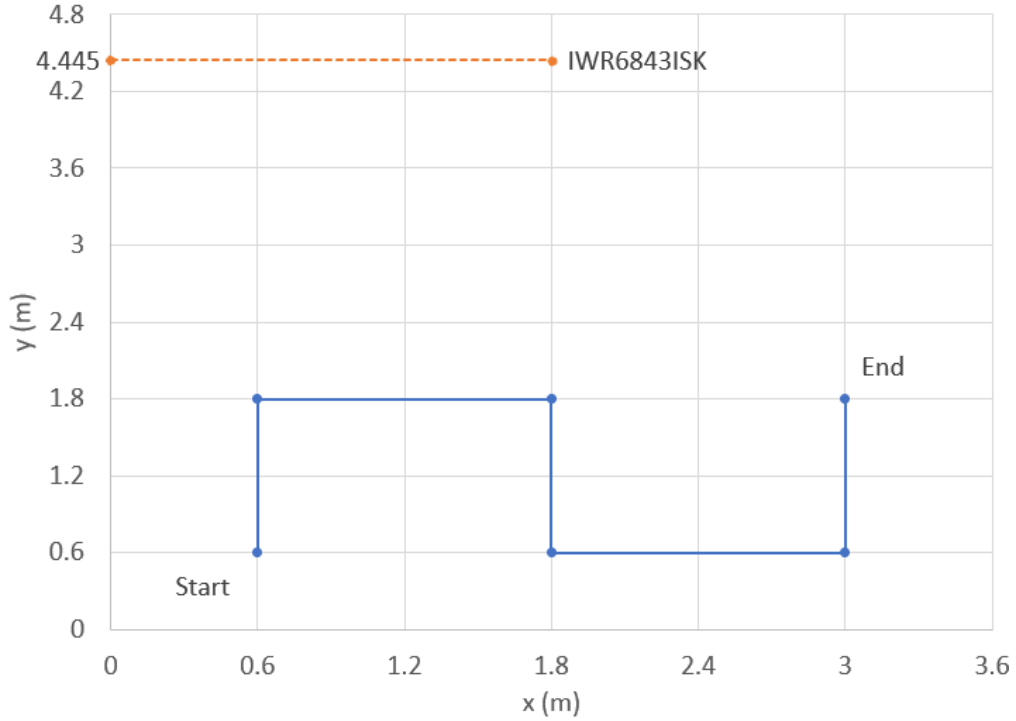

Figure 7.10: IWR6843ISK set-up for Corridor measurements. The orange dot represents the sensor position, while the blue path is the real trajectory

segment in Configuration 1, while presents no positive y offset in all the other 3 Configurations. Lastly, the lower horizontal segment present a good accuracy in all the Configurations.

7.2.3 Environment: Terrace

The set-up utilized in these experiments is shown in Figure 7.12 while the measured vs. real trajectories for all the configurations are visible in Figure 7.13.

In all the Configurations, the whole measured trajectory is shifted in the negative x direction with respect to the real trajectory, with the highest offset in the left-most vertical segment. Nevertheless, the central vertical segment presents the lowest offset among the vertical segments. In all Configurations, similarly to the measurements performed in the Laboratory, in the horizontal segment at y = 1.8 m there is a high offset in the positive y direction nearby the left-most vertical segment. Lastly, all Configurations show a positive y offset in the lower horizontal segment, which is lower in Configuration 2 and higher in Configuration 4.

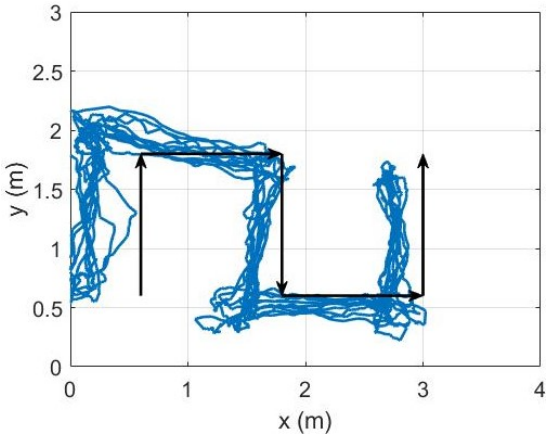

(a) Corridor measure: Configuration 1

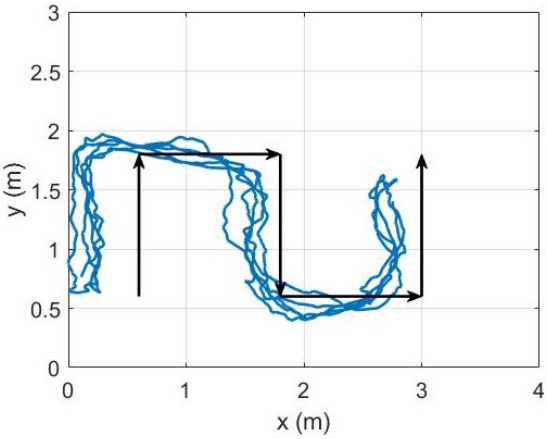

(b) Corridor measure: Configuration 2

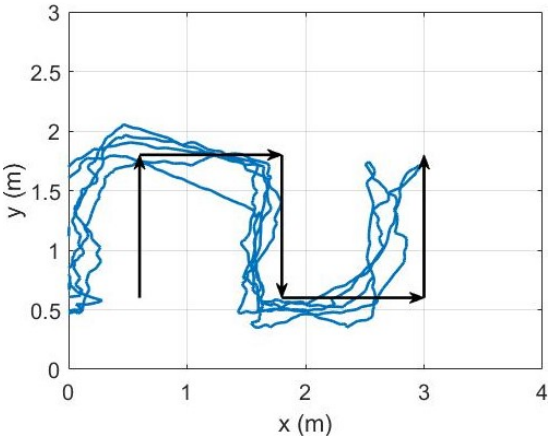

(c) Corridor measure: Configuration 3

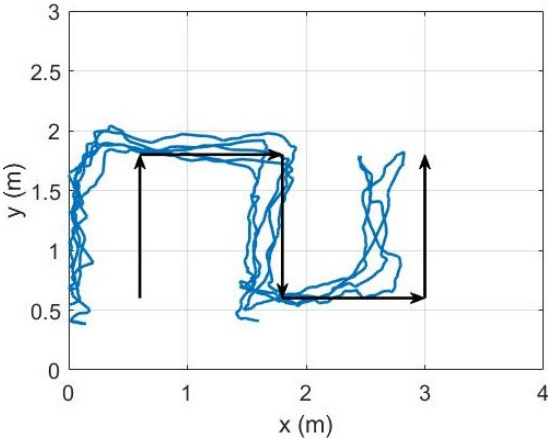

(d) Corridor measure: Configuration 4

Figure 7.11: IWR6843ISK Corridor measured trajectories (in blue) vs. real trajectories (in black)

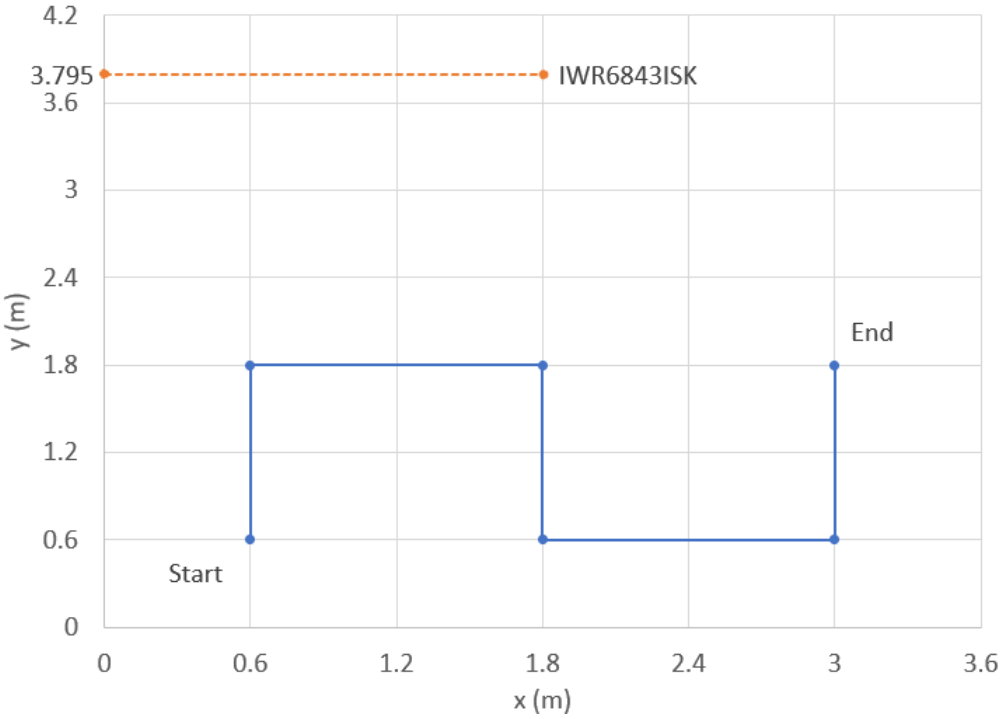

Figure 7.12: IWR6843ISK set-up for Terrace measurements. The orange dot represents the sensor position, while the blue path is the real trajectory

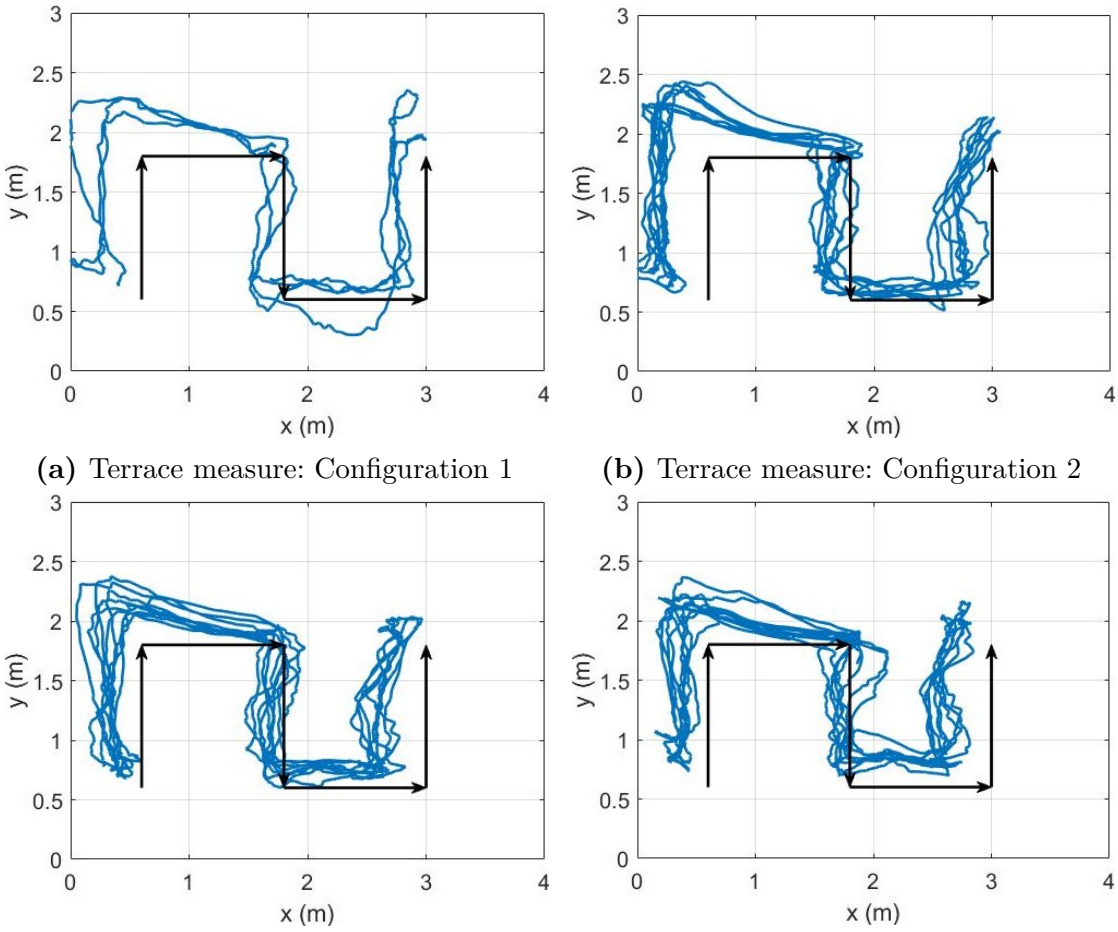

(a) Terrace measure: Configuration 1

(b) Terrace measure: Configuration 2

(c) Terrace measure: Configuration 3

(d) Terrace measure: Configuration 4

Figure 7.13: IWR6843ISK Terrace measured trajectories (in blue) vs. real trajectories (in black)

Table 7.1: Position2Go and IWR6843ISK sensors linear regression, where the green highlighted entries are the configurations with the lowest linear regression errors

Location	Config.	Position2Go		IWR6843ISK	
		Mean error (m)	**Standard deviation** (m)	**Mean error** (m)	**Standard deviation** (m)
Laboratory	1	0.100	0.095	0.108	0.081
	2	0.085	0.051	0.148	0.118
	3	0.121	0.075	0.095	0.066
	4	0.053	0.023	0.110	0.091
Corridor	1	0.088	0.047	0.122	0.092
	2	0.101	0.100	0.142	0.108
	3	0.097	0.055	0.121	0.088
	4	0.083	0.067	0.112	0.091
Outdoor	1	0.077	0.060	0.140	0.824
	2	0.132	0.114	0.109	0.081
	3	0.100	0.067	0.092	0.066
	4	0.081	0.074	0.082	0.069

7.3 Sensor Result Comparison

In the following section, the error graphs of the two boards are presented, allowing us to evaluate and compare the results obtained, in order to understand which configuration is the best in every environment, and which sensor is the one with the best performances in the localization and tracking task.

As stated in Chapter 6, four types of evaluation criteria have been chosen in order to evaluate the sensors performances, with the last one being the relative location error computed after the minimization.

- *Linear regression error*: shown in Figure 7.14 the linear regression errors of the two sensors in all environments divided by configuration. Table 7.1 shows the numerical values of the Position2Go and IWR6843ISK sensors linear regression errors.

  The Position2Go sensor shows the lowest linear regression error in the Laboratory environment (Configuration 4), while the highest error is reached in the Garden area (Configuration 2). The IWR6843ISK sensor, which linear regression errors are slightly higher than the one of the Position2Go sensor, presents the lowest error in Terrace (Configuration 4) and the highest one in

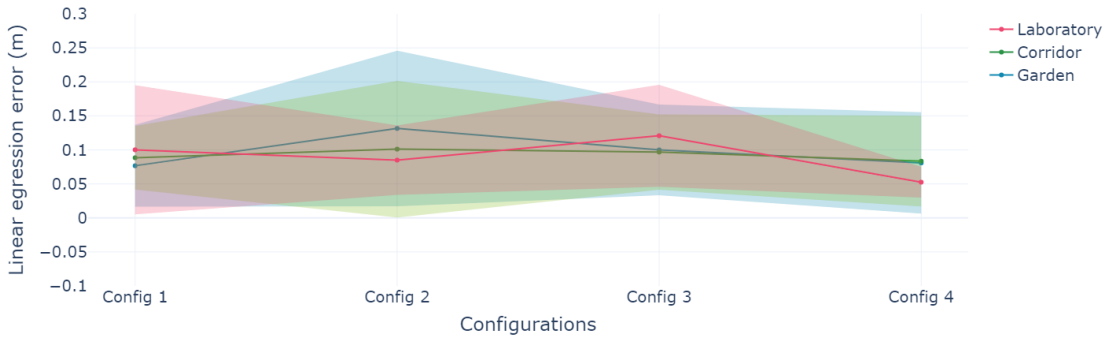

(a) Position2Go linear regression errors

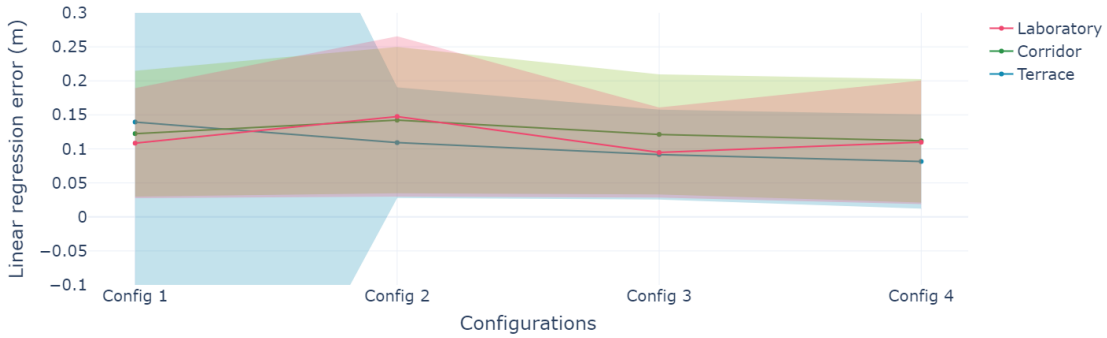

(b) IWR6843ISK linear regression errors

Figure 7.14: Environments linear regression errors for the two sensors for all sensor configurations. The continuous line is the mean linear regression error of the configuration, while the semi-transparent area is the standard deviation of such value

the Laboratory environment (Configuration 2).

- *Root area error*: shown in Figure 7.15 the root area errors of the two sensors in all environments divided by configuration. In Table 7.2 the numerical values of the Position2Go and IWR6843ISK sensors root area errors.

  The Position2Go sensor shows both the lowest and the highest area error in the Garden environment with the lowest error in Configuration 1 and the highest in Configuration 3. The IWR6843ISK reaches both the lowest and the highest area error in the Laboratory environment, with the lowest one being in Configuration 3 and the highest in Configuration 1.

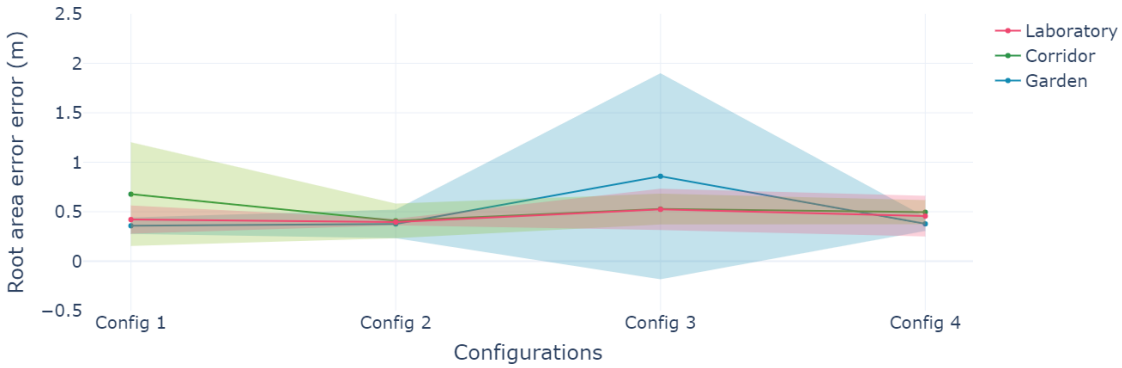

(a) Position2Go root area errors

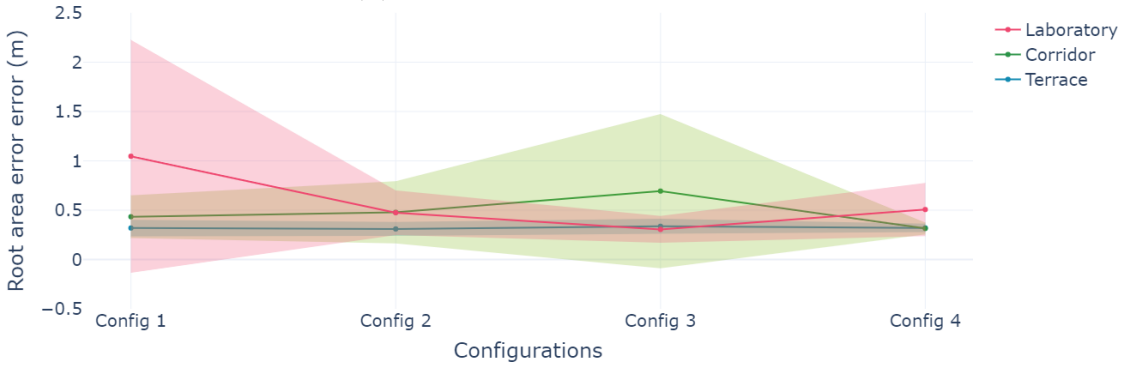

(b) IWR6843ISK root area errors

Figure 7.15: Environments root area errors for the two sensors for all sensor configurations. The continuous line is the mean root area error of the configuration, while the semi-transparent area is the standard deviation of such value

The area error falls within the same range for both sensors.

- *Acceleration*: shown in Figure 7.16 the acceleration of the two sensors in all environments divided by configuration. In these plots the scale on the y axis is not the same for the two sensors, since if otherwise the Position2Go plot would have resulted not readable, due to the very low values of the acceleration. In Table 7.3 the numerical values of the Position2Go and IWR6843ISK sensors accelerations.

  The Position2Go reaches the lowest acceleration in the Corridor environment, in Configuration 2, while the highest value is reached in the Configuration 1 measurement of the Laboratory area. The Texas Instruments sensor presents the lowest acceleration in the Configuration 1 utilized in the Laboratory measurement, while the highest one is reached in the Terrace (Configuration 4). It is worth noticing that the Position2Go achieves in general a lower acceleration

Table 7.2: Position2Go and IWR6843ISK sensors root area error, where the green highlighted entries are the configurations with the lowest root area error

Location	**Config.**	**Position2Go**		**IWR6843ISK**	
		Mean error (m)	**Standard deviation** (m)	**Mean error** (m)	**Standard deviation** (m)
Laboratory	1	0.421	0.142	1.046	1.180
	2	0.395	0.033	0.475	0.226
	3	0.524	0.208	0.305	0.136
	4	0.456	0.205	0.506	0.270
Corridor	1	0.677	0.524	0.433	0.216
	2	0.408	0.175	0.478	0.316
	3	0.527	0.154	0.693	0.781
	4	0.495	0.122	0.314	0.060
Outdoor	1	0.358	0.083	0.319	0.084
	2	0.377	0.145	0.310	0.070
	3	0.859	1.042	0.336	0.076
	4	0.378	0.071	0.321	0.043

Table 7.3: Position2Go and IWR6843ISK sensors acceleration measurements, where the green highlighted entries are the configurations with the lowest acceleration

Location	**Config.**	**Position2Go**		**IWR6843ISK**	
		Mean error (m/s^2)	**Standard deviation** (m/s^2)	**Mean error** (m/s^2)	**Standard deviation** (m/s^2)
Laboratory	1	1.058	0.530	1.685	0.273
	2	0.741	0.131	1.937	0.444
	3	0.807	0.271	1.761	0.389
	4	0.882	0.462	1.945	0.278
Corridor	1	0.816	0.402	2.263	0.141
	2	0.667	0.134	2.222	0.259
	3	0.840	0.358	2.027	0.192
	4	1.011	0.616	2.231	0.472
Outdoor	1	0.775	0.174	2.089	0.346
	2	0.780	0.337	2.416	0.616
	3	0.721	0.251	2.264	0.559
	4	0.821	0.388	2.464	1.007

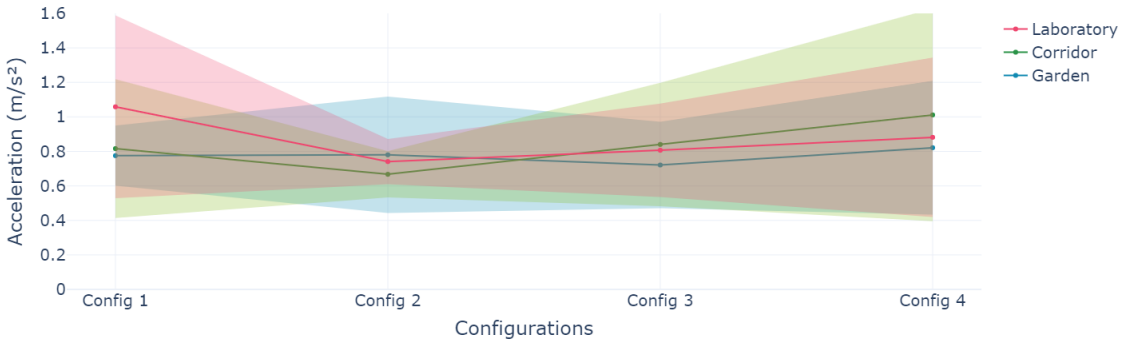

(a) Position2Go acceleration

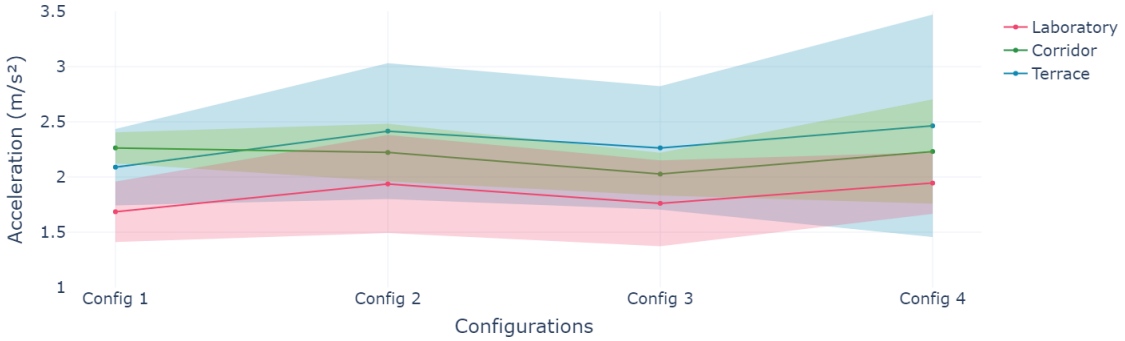

(b) IWR6843ISK acceleration

Figure 7.16: Environments acceleration for the two sensors for all sensor configurations. The continuous line is the mean acceleration of the configuration, while the semi-transparent area is the standard deviation of such value

in all experiments, due to the application of the moving-average filter.

- *Minimized relative location error*: shown in Figure 7.17 the minimized relative location errors of the two sensors in all environments divided by configuration. As shown in Table 7.4, the relative location errors values of the Position2Go and IWR6843ISK sensors before and after the minimization. The table shows the original relative location errors vs. the minimized relative location errors obtained through path translation.

  In general, the location errors of the Position2Go sensor are much greater than the ones present in the Texas Instruments sensor, this is also reflected in the relative location error re-calculated after the minimization process, where the highest reduction of this value is reached by the IWR6843ISK, which shows, for instance, a reduction of the error of the 79.5 % in the Configuration 4 of the Laboratory measurement.

In Table 7.5 all the evaluation criteria that obtained the best performances

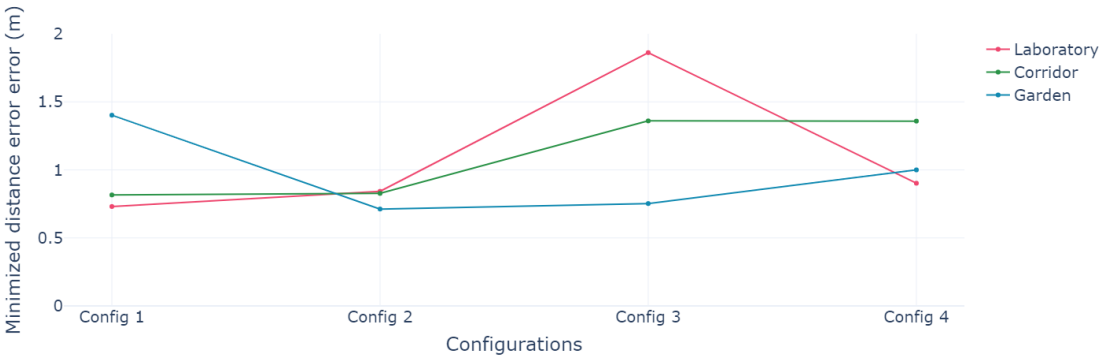

(a) Position2Go minimized relative location errors

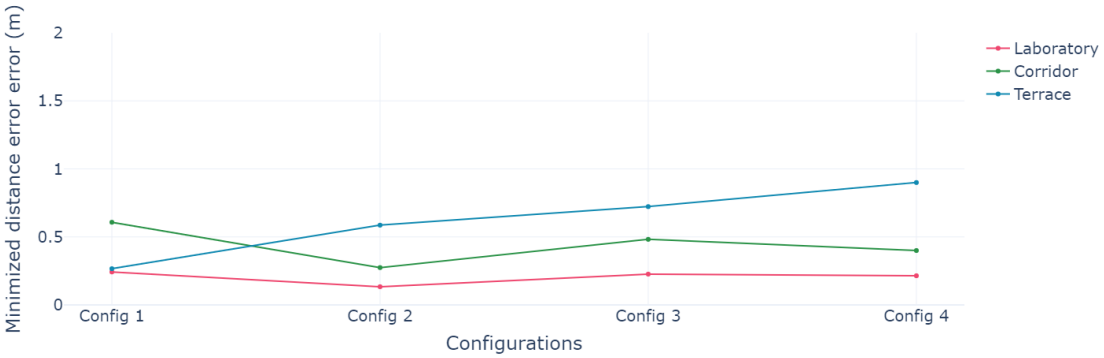

(b) IWR6843ISK minimized relative location errors

Figure 7.17: Environments minimized relative location errors for the two sensors for all sensor configurations

for the Position2Go sensor in all environments, while in Table 7.6 all the best performances measurements for the IWR6843ISK sensor. The tables report the lowest evaluation criteria in every environment, highlighted with the color associated to the configuration through which the value has been obtained, in order to categorize them.

From the error graphs of Figure 7.14, Figure 7.15, Figure 7.16, Figure 7.17, and from Table 7.5, and Table 7.6 it is possible to determine which configuration is the best in every environment for every sensor. The preferred configuration selections are based on the majority of vote of the preferred configuration per evaluation criteria. Since we have four evaluation criteria, if in a particular environment, a configuration obtains the lowest error for two or more criteria, then such configuration is the best one in that particular environment. An overview of the preferred configuration

Table 7.4: Position2Go and IWR6843ISK sensors original location error vs. minimized location error, where the green highlighted entries are the configurations that achieve the lowest minimized relative location error

Location	**Config.**	**Position2Go**		**IWR6843ISK**	
		Original error (m)	**Min error** (m)	**Original error** (m)	**Min error** (m)
Laboratory	1	1.086	0.731	0.528	0.242
	2	1.221	0.842	0.506	0.134
	3	2.103	1.862	0.513	0.226
	4	1.325	0.902	1.048	0.214
Corridor	1	1.417	0.816	1.356	0.608
	2	1.046	0.827	1.013	0.274
	3	1.561	1.360	1.167	0.482
	4	1.474	1.359	1.151	0.400
Outdoor	1	2.279	1.402	0.711	0.266
	2	1.419	0.712	1.305	0.586
	3	1.470	0.752	1.173	0.723
	4	1.537	1.000	1.213	0.900

Table 7.5: Position2Go sensor best measurements per environment, where Configuration 1, Configuration 2, Configuration 3, Configuration 4

Location	**Linear regression error** (m)	**Root area error** (m)	**Acceleration** (m/s^2)	**Relative location error** (m)
Laboratory	0.053	0.395	0.741	0.731
Corridor	0.083	0.408	0.667	0.816
Garden	0.077	0.358	0.721	0.712

selections for Position2Go can be seen in Table 7.7, and for the IWR6843ISK in Table 7.8. In the two tables, the preferred configurations are reported in a decreasing order of importance, e.g., the first configuration is the one with the highest number of votes, while the last configurations is the one with the least number, or zero number, of votes.

From Table 7.7, we can see that the Position2Go sensor have two preferred configurations: Configuration 2 for Laboratory and Corridor, and Configuration 1 for Garden. Additionally, it can be noticed that the Configuration 2 is the second

Table 7.6: IWR6843ISK sensor best measurements per environment, where Configuration 1, Configuration 2, Configuration 3, Configuration 4

Location	**Linear regression error** (m)	**Root area error** (m)	**Acceleration** (m/s^2)	**Relative location error** (m)
Laboratory	0.095	0.305	1.685	0.134
Corridor	0.112	0.314	2.027	0.274
Terrace	0.082	0.310	2.089	0.711

Table 7.7: Position2Go best configurations per environment using majority voting (has the lowest error for at least half of the evaluation criteria). In the *Preferred* column, the configurations in decreasing order of votes

Location	**Best Configuration**				**Preferred**
	Linear regression	**Root area**	**Acceleration**	**Relative location**	
Laboratory	4	2	2	1	2,1,4,3
Corridor	4	2	2	1	2,1,4,3
Garden	1	1	3	2	1,2,3,4

preferred configuration in the Garden environment, while Configuration 1 is the second preferred configuration in both the indoor environments. Configuration 3 and Configuration 4 can be considered the worst configurations, since the latters appears always in the third or in the last position of the preferred configurations. On the other hand, the IWR6843ISK has several preferred configurations: Configuration 3 for Laboratory, Configuration 4 for Corridor, Configuration 1 for Terrace. Additionally, Configuration 2 is the second preferred configuration in Corridor and Terrace environments, while is the third preferred configuration in Laboratory environment. Differently from the case of the Position2Go, it is not easy to say which configuration is the worst, since the positions of the latter are very variable.

In comparison to the best outdoor configuration, (Configuration 1), the Position2Go preferred indoor configuration, is Configuration 2 for both *Lab* and *Corridor* environments. This configuration achieves a significantly higher *Linear regression error*, and slightly higher values of both *Root area error* and *Acceleration*. In addition, Configuration 2 achieves the lowest *Minimized relative location error* in the outdoor environment. From this results, we can say that this configuration would work well even in outdoor environments, obtaining similar results than the preferred outdoor configuration. Note that, it is likely that the *Linear regression*

Table 7.8: IWR6843ISK best configurations per environment using majority voting (has the lowest error for at least half of the evaluation criteria). In the *Preferred* column, the configurations in decreasing order of votes

Location	**Best Configuration**				**Preferred**
	Linear regression	**Root area**	**Acceleration**	**Relative location**	
Laboratory	3	3	1	2	3,1,2,4
Corridor	4	4	3	2	4,2,3,1
Terrace	4	2	1	1	1,2,4,3

error would get worse.

The IWR6843ISK sensor has two preferred configurations in the chosen indoor environments. In the *Lab* environment, Configuration 3 is the preferred overall, while in the *Corridor* environment, Configuration 4 is the preferred overall. Making again the comparison with the preferred outdoor configuration (Configuration 1), we have:

- The preferred *Lab* configuration for the IWR6843ISK achieves a slightly lower *Linear regression error*, slightly higher *Root area error* and *Acceleration* values, and a remarkably higher *Minimized relative location error*. This means that this configuration would work well also in outdoor environments. Despite it is likely to achieve a lower *Linear regression error*, this configuration would also result in a significantly higher *Minimized relative location error*.

- The preferred *Corridor* environment configuration achieves the lowest *Linear regression error*, a slightly higher *Root area error*, a higher *Acceleration*, and an importantly higher *Minimized relative location error*. This means that the configuration is not suitable for outdoor environments, since all the evaluation criteria, except for the *Linear regression error*, are worse than the actual best outdoor configuration.

If, instead, we look only at the positions of the configurations in Table 7.8, it would result that the preferred *Laboratory* configuration, Configuration 3, would not work well in outdoor environments, since the latter is in the last position of the preferred ones, while the *Corridor* preferred configuration, Configuration 4, would work well since it is the third preferred configuration for the *Terrace* environment.

From the results obtained in this chapter, each evaluation criteria of the two sensors obtain in general similar values, with the exception of the *Minimized relative location error* which is lower in the IWR6843ISK, and the *Acceleration*, which is lower in the Position2Go. On the other hand, the Position2Go sensor has a higher

need for post-processing algorithm, e.g., the application of a moving-average on the measured positions, hence we can conclude that the IWR6843ISK sensor is the best choice for indoor human localization.

Chapter 8

Conclusion

The objective of this thesis work is to introduce and explore the techniques for human localization and tracking based on sensors in indoor environments, as opposed to the human tracking performed by GPS in outdoor environments. The initial step has been to perform a research on the available techniques, followed by the market analysis of the sensors with the best performances.

The chosen sensors to investigate are the radar sensors, which allowed us to select two sensor evaluation boards, the Position2Go and the IWR6843ISK, two sensors that work at different frequencies, particular that encouraged me to perform the comparison between the two radars.

The main challenge I faced has been choosing the configurations, which then led to four different configurations for both sensors. The objective of the different configurations was to understand if the change of the parameters had an impact on the localization performance, and if such impact would change with the change of the environments. Once chosen the configurations, three environments have been selected for the experiments, two indoor environments, the Laboratory and the Corridor, and one outdoor environment, the Terrace for the Texas Instruments sensor, and the Garden for the Infineon sensor. The outdoor environment in which the experiments have been performed is different due to interference problems faced by the Position2Go sensor in the Terrace environment, a phenomenon that did not affect the IWR6843ISK measurements. The different outdoor environment, however, still allows the results comparison, since the characteristics of the outdoor environments are basically the same: large area without the presence of walls or ceiling.

All the experiments, have been performed utilizing the original demo firmwares provided by the producers for both sensors. Differently from the IWR6843ISK, where the raw measurements data have been utilized, the Position2Go sensor needed a filtering operation through a moving-average filter of window size five and an outlier removal step.

After all the data have been collected, four criteria have been chosen for the evaluation of those measurements: Linear regression error, Root area error, Acceleration, and Relative location error, where the latter has been then minimized with a path optimization procedure, which consists of the translation of the full measured path.

From the evaluation, it was found out that the Position2Go has one preferred indoor configuration and one preferred outdoor configuration, chosen in terms of performances of the criteria. In particular, the preferred indoor configuration results to be the second-preferred outdoor configuration, while the preferred outdoor configuration results to be the second-preferred indoor configuration. From this result we can say that the preferred indoor configuration would work well even in outdoor environments.

On the other hand, the IWR6843ISK has two preferred indoor configurations, one for the Laboratory and the other one for the Corridor, chosen in terms of performances of the criteria. If we look only at the votes for the preferred configurations, e.g., in how many evaluation criteria such configuration achieved the lowest value, it would result that the preferred configuration in the Corridor environment would work well even in outdoor environments, since this configuration is the third-preferred one for the Terrace environment.

The Relative location error of the original measurements, is very low in the IWR6843ISK sensor, compared with the one obtained by the Position2Go sensor. The self-consistency of the IWR6843ISK sensor is slightly worse than the Position2Go sensor in some of the configurations, but more or less the same, from what is reported in the Root area error. The two sensors obtain the almost same Linear regression error, while the Position2Go sensor has a better measured Movement smoothness, since the computed acceleration is very low compared to the IWR6843ISK sensor, due to the moving-average filter application in the data.

From the evaluation performed on the measurements, it results that the two sensors achieve more or less the same performance in the chosen environments, but the higher need for post-processing algorithms on the measurements of the Position2Go sensor, e.g., the implementation of a moving-average, make the IWR6843ISK the best choice between the two sensors. In addition, the results obtained from both sensors can be improved via post-processing algorithms like the one employed for this thesis, which translates the measured trajectory depending on the location error previously computed.

Future developments of this activity could be to perform a fine tuning of the configurations in order to obtain the best ones for both sensors, to employ more advanced post-processing algorithms, in order to produce even better results from the initial data. These algorithms could also include all kinds of techniques related to the Machine Learning field, like Regression algorithms, Neural Networks or Deep Networks.

Another possible development could be to modify the firmware of the sensors, improving the tracking algorithms employed since the Texas Instruments sensor shows a more precise software for the tracking task than the Position2Go sensor. The precision difference between the two sensors has been noticed during the measurements since the Position2Go radar loses the acquired target more often than the IWR6843ISK sensor.

Bibliography

[1] Kerem Özsoy, Ayhan Bozkurt, and Ibrahim Tekin. «2D Indoor positioning system using GPS signals». In: *2010 International Conference on Indoor Positioning and Indoor Navigation*. 2010, pp. 1–6. DOI: 10.1109/IPIN.2010.5647644 (cit. on p. 3).

[2] Tomislav Kos, Ivan Markezic, and Josip Pokrajcic. «Effects of multipath reception on GPS positioning performance». In: *Proceedings ELMAR-2010*. 2010, pp. 399–402 (cit. on p. 3).

[3] Biying Fu, Naser Damer, Florian Kirchbuchner, and Arjan Kuijper. «Sensing Technology for Human Activity Recognition: A Comprehensive Survey». In: *IEEE Access* 8 (2020), pp. 83791–83820. DOI: 10.1109/ACCESS.2020.2991891 (cit. on pp. 3, 4).

[4] Klaus Finkenzeller. *RFID handbook: fundamentals and applications in contactless smart cards, radio frequency identification and near-field communication*. John wiley & sons, 2010 (cit. on p. 4).

[5] Rachid Mafamane, Asmae Ait Mansour, Mourad Ouadou, and Khalid Minaoui. «FTSMAC: A Multi-Channel Hybrid Reader Collision Avoidance Protocol for RFID Network». In: *Journal of Sensor and Actuator Networks* 10.3 (2021). ISSN: 2224-2708. DOI: 10.3390/jsan10030046. URL: https://www.mdpi.com/2224-2708/10/3/46 (cit. on p. 5).

[6] Qian Ma, Xia Li, Guanyu Li, Bo Ning, Mei Bai, and Xite Wang. «MRLIHT: Mobile RFID-based Localization for Indoor Human Tracking». In: *Sensors* 20 (Mar. 2020), p. 1711. DOI: 10.3390/s20061711 (cit. on p. 6).

[7] Yu-Jin Hong, Ig-Jae Kim, Sang Chul Ahn, and Hyoung-Gon Kim. «Activity Recognition Using Wearable Sensors for Elder Care». In: *2008 Second International Conference on Future Generation Communication and Networking*. Vol. 2. 2008, pp. 302–305. DOI: 10.1109/FGCN.2008.165 (cit. on p. 6).

[8] C. Bisdikian. «An overview of the Bluetooth wireless technology». In: *IEEE Communications Magazine* 39.12 (2001), pp. 86–94. DOI: 10.1109/35.968817 (cit. on p. 6).

[9] Marcin Kolakowski and Bartosz Blachucki. «Monitoring Wandering Behavior of Persons Suffering from Dementia Using BLE Based Localization System». In: *2019 27th Telecommunications Forum (TELFOR)*. 2019, pp. 1–4. DOI: 10.1109/TELFOR48224.2019.8971136 (cit. on pp. 6, 7).

[10] Keiron O'Shea and Ryan Nash. «An introduction to convolutional neural networks». In: *arXiv preprint arXiv:1511.08458* (2015) (cit. on p. 7).

[11] Larry Medsker and Lakhmi C Jain. *Recurrent neural networks: design and applications*. CRC press, 1999 (cit. on p. 7).

[12] *Come funziona una rete neurale CNN (convolutional Neural Network)*. URL: https://www.domsoria.com/2019/10/come-funziona-una-rete-neurale-cnn-convolutional-neural-network/ (cit. on p. 8).

[13] Nura Aljaafari. «Ichthyoplankton Classification Tool using Generative Adversarial Networks and Transfer Learning». PhD thesis. Feb. 2018 (cit. on p. 8).

[14] Daniel Svozil, Vladimir Kvasnicka, and Jiri Pospichal. «Introduction to multi-layer feed-forward neural networks». In: *Chemometrics and intelligent laboratory systems* 39.1 (1997), pp. 43–62 (cit. on p. 8).

[15] *Understanding Feedforward Neural Networks*. URL: https://learnopencv.com/understanding-feedforward-neural-networks/ (cit. on p. 9).

[16] *Rete neurale ricorrente*. URL: https://it.wikipedia.org/wiki/Rete_neurale_ricorrente (cit. on p. 9).

[17] J Michael Lloyd. *Thermal imaging systems*. Springer Science & Business Media, 2013 (cit. on p. 9).

[18] *Omron D6T8L06 MEMS Thermal Infrared Temperature Sensor, +5°C to +50°C*. URL: https://il.rsdelivers.com/product/omron/d6t8l06/omron-d6t8l06-mems-thermal-infrared-temperature-5c/8226421 (cit. on p. 10).

[19] *HTI HT-A1 termocamera, tascabile risoluzione telecamera ad infrarossi 220x160*. URL: https://www.ebay.it/itm/352467149774 (cit. on p. 10).

[20] *Le termocamere FLIR colgono sul fatto i taccheggiatori*. URL: https://www.flir.it/discover/security/commercial/flir-cameras-catch-shoplifters-red-handed2/ (cit. on p. 10).

[21] J. R. Smith. «Field mice: Extracting hand geometry from electric field measurements». In: *IBM Systems Journal* 35.3.4 (1996), pp. 587–608. DOI: 10.1147/sj.353.0587 (cit. on p. 11).

[22] Miguel Sousa, Axel Techmer, Axel Steinhage, Christl Lauterbach, and Paul Lukowicz. «Human tracking and identification using a sensitive floor and wearable accelerometers». In: *2013 IEEE International Conference on Pervasive Computing and Communications (PerCom)*. 2013, pp. 166–171. DOI: 10.1109/PerCom.2013.6526728 (cit. on p. 11).

[23] Miika Valtonen, Jaakko Maentausta, and Jukka Vanhala. «TileTrack: Capacitive human tracking using floor tiles». In: *2009 IEEE International Conference on Pervasive Computing and Communications*. 2009, pp. 1–10. DOI: 10.1109/PERCOM.2009.4912749 (cit. on p. 11).

[24] Samiksha Sikarwar, Shakti Singh, Bal Chandra Yadav, et al. «Review on pressure sensors for structural health monitoring». In: *Photonic Sensors* 7.4 (2017), pp. 294–304 (cit. on p. 11).

[25] *MEMS Capacitive vs Piezoresistive Pressure Sensors – What are their differences?* URL: https://esenssys.com/capacitive-piezoresistive-pressure-sensors-differences/ (cit. on p. 12).

[26] Alan Bränzel, Christian Holz, Daniel Hoffmann, Dominik Schmidt, Marius Knaust, Patrick Lühne, René Meusel, Stephan Richter, and Patrick Baudisch. «GravitySpace: Tracking Users and Their Poses in a Smart Room Using a Pressure-Sensing Floor». In: *Proceedings of the SIGCHI Conference on Human Factors in Computing Systems*. CHI '13. Paris, France: Association for Computing Machinery, 2013, pp. 725–734. ISBN: 9781450318990. DOI: 10.1145/2470654.2470757. URL: https://doi.org/10.1145/2470654.2470757 (cit. on p. 12).

[27] Ashraf Tahat, Georges Kaddoum, Siamak Yousefi, Shahrokh Valaee, and Francois Gagnon. «A look at the recent wireless positioning techniques with a focus on algorithms for moving receivers». In: *IEEE Access* 4 (2016), pp. 6652–6680 (cit. on p. 12).

[28] Wenda Li, Robert J. Piechocki, Karl Woodbridge, Chong Tang, and Kevin Chetty. «Passive WiFi Radar for Human Sensing Using a Stand-Alone Access Point». In: *IEEE Transactions on Geoscience and Remote Sensing* 59.3 (2021), pp. 1986–1998. DOI: 10.1109/TGRS.2020.3006387 (cit. on pp. 12, 13).

[29] Fadel Adib. «Seeing with radio Wi-Fi-like equipment can see people through walls, measure their heart rates, and gauge emotions». In: *IEEE Spectrum* 56.6 (2019), pp. 34–39. DOI: 10.1109/MSPEC.2019.8727144 (cit. on p. 12).

[30] Guido R. Hiertz, Dee Denteneer, Lothar Stibor, Yunpeng Zang, Xavier Perez Costa, and Bernhard Walke. «The IEEE 802.11 universe». In: *IEEE Communications Magazine* 48.1 (2010), pp. 62–70. DOI: 10.1109/MCOM.2010.5394032 (cit. on p. 12).

[31] Seeed Studio. *Grove - Sound Sensor*. URL: https://wiki.seeedstudio.com/Grove-Sound_Sensor/ (cit. on p. 16).

[32] WHADDA. *MODULO SENSORE ACUSTICO MICROFONO, COMPATIBILE ARDUINO®*. URL: https://www.velleman.eu/products/view/?id=459214 (cit. on p. 16).

[33] *SPH0645LM4H-B - I2S Output Digital Microphone*. Rev. B. Knowles. July 2015 (cit. on p. 16).

[34] *IM69D130 - High performance digital XENSIV™MEMS microphone*. Rev. 1.0. Infineon. Dec. 2017 (cit. on p. 16).

[35] *MP23ABS1 - High-performance MEMS audio sensor: single-ended analog bottom-port microphone*. Rev. 6. STMicroelectronics. Oct. 2020 (cit. on p. 16).

[36] *Sound Detection Sensor*. Rajguru Electronics (cit. on p. 16).

[37] *SPV1840LR5H-B - Zero-Height SiSonic™Microphone*. Rev. B. Knowles. Feb. 2013 (cit. on p. 16).

[38] *SPM1423HM4H-B - Digital High-SNR SiSonic™Microphone*. Rev. D. Knowles. June 2013 (cit. on p. 16).

[39] *SPH0611LR5H-1 - Precision High SNR Zero-Height SiSonic™Microphone*. Rev. A. Knowles. Apr. 2013 (cit. on p. 16).

[40] *SPM0437HD4H-B - Digital SiSonic™Microphone*. Rev. A. Knowles. July 2013 (cit. on p. 16).

[41] *SPU1410LR5H-QB - Zero-Height SiSonic™Microphone With Extended Low Frequency Performance*. Rev. D. Knowles. Mar. 2013 (cit. on p. 16).

[42] *Ultrasonic Ranging Module HC - SR04*. ElecFreaks (cit. on pp. 17, 23).

[43] *HY-SRF05 Precision Ultrasonic Sensor*. ETC (cit. on p. 17).

[44] *Gravity: URM09 Analog Ultrasonic Sensor*. DFRobot (cit. on p. 17).

[45] *A02YYUW Waterproof Ultrasonic Sensor*. DFRobot (cit. on p. 17).

[46] *HRLV-MaxSonar®- EZ™Series*. MaxBotic (cit. on p. 17).

[47] *XL-MaxSonar®- EZ™Series*. MaxBotic (cit. on p. 17).

[48] Heschen. *Capacitive Proximity Sensor Switch LJC12A3-5-Z/AY Detector 5mm 6-36 VDC 200mA PNP normally Closed(NC) 3 wire*. URL: https://heschen.com/products/b078xh2t44 (cit. on p. 18).

[49] Heschen. *Capacitive Proximity Sensor Switch LJC18A3-B-Z/BX detector 1-10mm 6-36 VDC 300mA NPN Normally Open(NO) 3 wire*. URL: https://heschen.com/products/ljc18a3-b-z-bx (cit. on p. 18).

[50] *CAT2-12GM series capacitive proximity sensor*. URL: https://www.finglai.com/products/sensors/capacitive-proximity-sensors/CAT2-12GM/ (cit. on p. 18).

[51] *CAM8-20GM series capacitive proximity sensor*. URL: https://www.finglai.com/products/sensors/capacitive-proximity-sensors/CAM8-20GM/ (cit. on p. 18).

[52] *CPM40-80B series capacitive proximity sensor*. URL: https://www.finglai.com/products/sensors/capacitive-proximity-sensors/CPM40-80B/ (cit. on p. 18).

[53] *Proximity Sensors Capacitive Thermoplastic Polyester Housing Type EC, M30, AC*. Carlo Gavazzi (cit. on p. 18).

[54] *CA18EAxxBPxIO - IO-Link - Capacitive Proximity Sensors with IO-Link communication*. Carlo Gavazzi (cit. on p. 18).

[55] *KI5087 - KIA3150NFPKG/2T/US*. IFM (cit. on p. 18).

[56] *BGT24MTR11 - Silicon Germanium 24 GHz Transceiver MMIC*. Rev. 3.1. Infineon. Mar. 2014 (cit. on p. 19).

[57] *BGT24MTR12 - Silicon Germanium 24 GHz Transceiver MMIC*. Rev. 3.2. Infineon. July 2014 (cit. on p. 19).

[58] *BGT24LTR11N16 - Silicon Germanium 24GHz Radar Transceiver MMIC*. Rev. 1.3. Infineon. May 2018 (cit. on p. 19).

[59] *BGT24MR2 - Silicon Germanium 24 GHz Twin IQ Receiver MMIC*. Rev. 3.1. Infineon. Mar. 2014 (cit. on p. 19).

[60] *RR30.DAO0-IGPI.9VF - Radar distance measuring sensors*. Baumer (cit. on p. 19).

[61] *FM24-NP100 microwave range radar*. Chongqing Yanwu Tcchnology Co.,Ltd (cit. on p. 19).

[62] Seeed Studio. *Microwave Sensor - 24GHz Doppler Radar Motion Sensor - MW2401TR11*. URL: https://wiki.seeedstudio.com/Microwave-Sensor-24GHz-Doppler-Radar-Motion-Sensor-MW2401TR11/ (cit. on p. 19).

[63] *IWR6843, IWR6443 Single-Chip 60- to 64-GHz mmWave Sensor*. Rev. E. Texas Instruments. June 2021. URL: https://www.ti.com/lit/pdf/swrs219 (cit. on pp. 19, 20, 47–50).

[64] Infineon. *Distance2GoL (Software-Controlled FMCW) – XENSIV™ 24 GHz lowpower radar shield using BGT24LTR11 for range detection and human tracking*. Rev. 1.0. Chongqing Yanwu Tcchnology Co.,Ltd. Mar. 2021 (cit. on p. 20).

[65] Infineon. *Sense2GoL Pulse (Pulsed Doppler) – XENSIV™ 24 GHz low-power radar Shield using BGT24LTR11 for motion, speed and direction of movement detection*. Rev. 2.0. Aug. 2021 (cit. on p. 20).

[66] *Position2GO - XENSIV™24 GHz radar demo kit with BGT24MTR12 and XMC4700 32 - bit ARM® Cortex™- M4 MCU for ranging, movement and target position estimation*. Rev. 1.3. Infineon. May 2020 (cit. on pp. 20, 39).

[67] Seeed Studio. *Grove - Doppler Radar*. URL: https://wiki.seeedstudio.com/Grove-Doppler-Radar/ (cit. on p. 20).

[68] Infineon. *XENSIV™BGT60LTR11AIP shield*. Rev. 1.6. Oct. 2021 (cit. on p. 20).

[69] Infineon. *Radar baseboard MCU7*. May 2021 (cit. on p. 20).

[70] Acconeer. *A111 – Pulsed Coherent Radar (PCR)*. Rev. 2.1. Jan. 2020 (cit. on p. 20).

[71] Acconeer. *XC112 Connector Board Product Brief*. Rev. 1.1. Apr. 2021 (cit. on p. 20).

[72] Acconeer. *XR112 Radar Sensor Board Product Brief*. Rev. 2.1. Apr. 2021 (cit. on p. 20).

[73] OmniPreSence. *OPS243 Short-Range Radar* (cit. on p. 20).

[74] JORJIN TECHNOLOGIES. *MM5D91-00 -60GHz mmWave Radar - Presence Detection Sensor Module*. Rev. 1.0 (cit. on p. 20).

[75] Texas Instruments. *IWR1843 Single-Chip 76- to 81-GHz FMCW mmWave Sensor*. Rev. A. Jan. 2022 (cit. on p. 20).

[76] Texas Instruments. *xWR1843 Evaluation Module (xWR1843BOOST) Single-Chip mmWave Sensing Solution*. Rev. B. May 2020 (cit. on p. 20).

[77] *60GHz mmWave Sensor EVMs*. Rev. E. Texas Instruments. May 2022 (cit. on pp. 20, 47).

[78] Qingcui Wang, Shuanping Du, Fangyong Wang, and Yuechao Chen. «Underwater target recognition method based on multi-domain active sonar echo images». In: *2021 IEEE International Conference on Signal Processing, Communications and Computing (ICSPCC)*. 2021, pp. 1–5. DOI: 10.1109/ICSPCC52875.2021.9564611 (cit. on p. 21).

[79] Stefan Gombots, Jonathan Nowak, and Manfred Kaltenbacher. «Sound source localization–state of the art and new inverse scheme». In: *e & i Elektrotechnik und Informationstechnik* 138.3 (2021), pp. 229–243 (cit. on p. 22).

[80] Caleb Rascon and Ivan Meza. «Localization of sound sources in robotics: A review». In: *Robotics and Autonomous Systems* 96 (2017), pp. 184–210. ISSN: 0921-8890. DOI: https://doi.org/10.1016/j.robot.2017.07.011. URL: https://www.sciencedirect.com/science/article/pii/S0921889016304742 (cit. on p. 22).

[81] Stefano Coraluppi. «Multistatic Sonar Localization». In: *IEEE Journal of Oceanic Engineering* 31.4 (2006), pp. 964–974. DOI: 10.1109/JOE.2005.862117 (cit. on p. 22).

[82] *Sonar*. URL: https://en.wikipedia.org/wiki/Sonar (cit. on p. 23).

[83] Michal Kelemen, Ivan Virgala, Tatiana Kelemenová, Lubica Mikova, Peter Frankovskỳ, Tomáš Lipták, and Milan Lörinc. «Distance measurement via using of ultrasonic sensor». In: *Journal of Automation and Control* 3.3 (2015), pp. 71–74 (cit. on p. 22).

[84] Hong-Shik Kim and Jong-Suk Choi. «Advanced indoor localization using ultrasonic sensor and digital compass». In: *2008 International Conference on Control, Automation and Systems*. 2008, pp. 223–226. DOI: 10.1109/ICCAS.2008.4694553 (cit. on p. 22).

[85] *ReSpeaker Mic Array v2.0*. URL: https://wiki.seeedstudio.com/ReSpeaker_Mic_Array_v2.0/ (cit. on p. 24).

[86] *Ring72 AC Pro - 72 CHANNEL SYSTEM FOR VARIOUS MEASUREMENT SCENARIOS*. gfai tech GmbH (cit. on p. 24).

[87] M. Risoud, J.-N. Hanson, F. Gauvrit, C. Renard, P.-E. Lemesre, N.-X. Bonne, and C. Vincent. «Sound source localization». In: *European Annals of Otorhinolaryngology, Head and Neck Diseases* 135.4 (2018), pp. 259–264. ISSN: 1879-7296. DOI: https://doi.org/10.1016/j.anorl.2018.04.009. URL: https://www.sciencedirect.com/science/article/pii/S187972961830067X (cit. on pp. 24, 25).

[88] Muhammad Usman Liaquat, Hafiz Suliman Munawar, Amna Rahman, Zakria Qadir, Abbas Z. Kouzani, and M. A. Parvez Mahmud. «Localization of Sound Sources: A Systematic Review». In: *Energies* 14.13 (2021). ISSN: 1996-1073. DOI: 10.3390/en14133910. URL: https://www.mdpi.com/1996-1073/14/13/3910 (cit. on pp. 24–26).

[89] Leandro de Santana. «Fundamentals of acoustic beamforming». In: *Design and Operation of Aeroacoustic Wind Tunnel Tests for Group and Air Transport* (2017) (cit. on p. 26).

[90] António Ramos, Sverre Holm, Sigmund Gudvangen, and Ragnvald Otterlei. «Delay-and-sum Beamforming for Direction of Arrival Estimation Applied to Gunshot Acoustics». In: vol. 8019. Apr. 2011. DOI: 10.1117/12.886833 (cit. on p. 26).

[91] *How does Delay-and-Sum Beamforming in the Time Domain work?* URL: https://www.gfaitech.com/knowledge/faq/delay-and-sum-beamforming-in-the-time-domain (cit. on p. 27).

[92] *How does Delay-and-Sum Beamforming in the Frequency Domain work?* URL: https://www.gfaitech.com/knowledge/faq/delay-and-sum-beamforming-in-the-frequency-domain (cit. on p. 28).

[93] Clara Lohmann. *What you need to know about... Beamforming*. URL: https://www.linkedin.com/pulse/what-you-need-know-beamforming-clara-lohmann/ (cit. on p. 28).

[94] Lei Li, Kechao Lian, Jintao Fu, Pengfei Zhu, Zhiyong Hu, and Ce Guo. «Acoustic Enhanced Camera Tracking System Based on Small-Aperture MEMS Microphone Array». In: *IEEE Access* 8 (2020), pp. 215827–215839. DOI: 10.1109/ACCESS.2020.3041445 (cit. on pp. 27, 29, 30).

[95] Merrill Skolnik. «An introduction and overview of radar». In: *Radar Handbook* 3 (2008), pp. 1–1 (cit. on p. 31).

[96] *Short-Range Radar - A Look behind the Scenes*. URL: https://www.ilmsens.com/short-range-radar/ (cit. on p. 32).

[97] *Continuous-wave radar*. URL: https://en.wikipedia.org/wiki/Continuous-wave_radar (cit. on p. 33).

[98] *The fundamentals of millimeter wave radar sensors*. Texas Instruments. July 2020 (cit. on pp. 32, 34–38).

[99] *Position2Go software user manual*. Rev. 1.1. Infineon. June 2019 (cit. on pp. 32, 35, 37, 39–47, 60).

[100] *Radar a onda continua modulata in frequenza*. URL: https://www.radartutorial.eu/02.basics/rp08.it.html (cit. on p. 33).

[101] *Digital Chirp Generator for 77GHz Radar Transmitter*. URL: https://it.mathworks.com/matlabcentral/fileexchange/73585-digital-chirp-generator-for-77ghz-radar-transmitter (cit. on p. 34).

[102] Peng Chen, Zhenxin Cao, Zhimin Chen, and Chunhua Yu. «Sparse DOD/-DOA Estimation in a Bistatic MIMO Radar With Mutual Coupling Effect». In: *Electronics* 7 (Nov. 2018), p. 341. DOI: 10.3390/electronics7110341 (cit. on p. 38).

[103] Infineon. *DEMO POSITION2GO*. URL: https://www.infineon.com/cms/en/product/evaluation-boards/demo-position2go/ (cit. on p. 40).

[104] *24 GHz radar tools and development environment user manual*. Rev. 1.1. Infineon. July 2020 (cit. on p. 39).

[105] Texas Instruments. *IWR6843ISK - IWR6843 intelligent mmWave sensor standard antenna plug-in module*. URL: https://www.ti.com/tool/IWR6843ISK (cit. on p. 49).

[106] *3D People Counting Demo Software Implementation Guide*. Rev. 1.0. Texas Instruments. Feb. 2021 (cit. on pp. 47, 50, 51).

[107] *Detection Layer Parameter Tuning Guide for the 3D People Counting Demo*. Rev. 2.0. Texas Instruments. Oct. 2021 (cit. on pp. 47, 50, 51, 62).

[108] *Tracking radar targets with multiple reflection points*. Rev. 1.8. Texas Instruments. Feb. 2021 (cit. on pp. 47, 52–54, 56).

[109] *Group Tracker Parameter Tuning Guide for the 3D People Counting Demo*. Rev. 1.0. Texas Instruments (cit. on pp. 47, 50, 53–55).

[110] Texas Instruments. *People Counting Visualizer User's Guide - Overview*. URL: https://dev.ti.com/tirex/explore/node?node=AEHm-5JHl-24ru0Yz-Za4Q__VLyFKFf__LATEST (cit. on p. 57).

[111] Texas Instruments. *mmWave Sensing Estimator*. URL: https://dev.ti.com/gallery/view/1792614/mmWaveSensingEstimator/ver/1.3.0/ (cit. on p. 62).

Acknowledgements

I would like to thank Professor Mihai Lazarescu and Professor Luciano Lavagno for always supporting me throughout this thesis work and for giving me the opportunity to work on this thesis project. I also thank Politecnico di Torino for providing all the tools needed for this work, and for letting me use the university spaces for the development of the experiments needed for the thesis.

Finally, I must express my very profound gratitude to my parents for providing me with unfailing support and continuous encouragement throughout my years of study and through the process of writing this thesis; to my sister Antonella, who has ever guided and supported me. She has always been a point of reference for me and one of the best life models that I had ever been able to have.

I want to thank my girlfriend Noemi: thank you for always being there for me, for supporting me every time. You have never doubted me, you have always encouraged me to do more, to not stop. Thank you for everything.